DESIGN AND MATERIALS INNOVATIONS IN EMERGENT SOLID BATTERIES

by

Justin M. Whiteley

B.S., University of California, Berkeley, 2010

M.S., University of Colorado, Boulder, 2014

A thesis submitted to the

Faculty of the Graduate School of the

University of Colorado in partial fulfillment

of the requirements for the degree of

Doctor of Philosophy

Department of Mechanical Engineering

2016

This thesis entitled:
DESIGN AND MATERIALS INNOVATIONS IN EMERGENT SOLID BATTERIES
written by Justin M. Whiteley
has been approved for the Department of Mechanical Engineering

Prof. Sehee Lee

Dr. Heather Platt

Prof. Conrad Stoldt

Prof. Ronggui Yang

Prof. Wei Zhang

Date

The final copy of this thesis has been examined by the signatories, and we find that both the content and the form meet acceptable presentation standards of scholarly work in the above mentioned discipline.

Whiteley, Justin M. (Ph.D., Mechanical Engineering)

DESIGN AND MATERIALS INNOVATIONS IN EMERGENT SOLID BATTERIES

Thesis directed by Prof. Sehee Lee

Emergent technologies, such as electric vehicles and grid energy storage, are driving iterations of the lithium-ion battery (LIB) to exhibit enhanced safety and higher temperature capabilities. The commercial LIB based on organic liquid electrolytes presents a variety of safety concerns most notably flammability. Batteries encompassing inorganic solid electrolytes, known as solid-state batteries, have attracted significant attention in recent years due to resolution of overheating and thermal runaway, as well as lithium-ion conductivities matching liquids yet still maintaining a lithium transference number of unity. With commercial deployment rapidly approaching, solid-state research has been intensified to resolve many of the problems introduced once a liquid is replaced with a solid.

The most challenging problems presented in solid-state batteries are interfaces. These interfaces are present on a variety of length scales: between lithium and electrolyte, electrolyte and binder, active material and conductive additives, and within the active material itself. To mitigate many of the interfacing problems, a materials and/or engineering design approach is employed dependent upon the situation.

Fundamentals of electrolytic stability, particularly with $Li_{10}SiP_2S_{12}$, against metallic lithium are explored including the effects of the decomposition layer on battery performance. Mixed conductors, such as tin and TiS_2, are used for amplifying reaction area and simplifying charge transfer when interfacing with the active materials of silicon and FeS_2, respectively. A new design approach is demonstrated on producing thin solid membranes utilizing a self-healing polymer to form an in-situ polymeric matrix for mechanical strength and enhanced conductance. The new membrane is demonstrated as a self-optimizing interface to suppress the formation of lithium metal dendrites. In the final chapter, the solid interfaces are taken advantage of to demonstrate a new phenomenon

of charge storage that is only present in the solid-state - pseudocapacitance in disordered $LiTiS_2$.

Dedication

This thesis is dedicated to my family.

To my parents, Phyllis and Brian, who instilled in me the importance of education and societal betterment from my very first thoughts.

To my brothers, Aaron and Sam, who provided the advice of pursing a Ph.D. and motivation along the way through "friendly competition."

To my girlfriend, Nicole, who was a constant source of enthusiasm and patience.

Acknowledgements

The work in this thesis would not be possible without generous support from numerous individuals.

Prof. Sehee Lee: A tremendous adviser, mentor, and role model. One who took a chance on an individual with no research experience. Providing an everlasting energy and passion for the field of electrochemistry that has made a true impact on my life.

Members of ECEL: Lab-mates, mentors, and friends. Dr. Tom Yersak and Dr. Ji-Woo Kim for training me in the art of research. Dr. Daniela Molina Piper for being an endless source of encouragement and motivation. Dr. Tyler Evans for the countless conversations on electrochemistry and batteries to form a deep appreciation for the field and hone ambitions. To the many others who I've worked with in some capacity: post-docs, PhD students, MS students, and undergrads.

Collaborators: Realistically well over half of faculty and students in the Mechanical Engineering Department. The many groups in the Department of Chemistry, Aerospace Engineering, Civil Engineering, Environmental Engineering, BNL, NREL, and Seoul National University. Whether to use equipment, successful collaborations, or wild ideas that didn't proceed, all have had an impact on my work.

Solid Power Inc.: Particularly, Dr. Heather Platt and Josh Buettner-Garrett for advice and guidance usually when it was needed most.

The author is grateful for financial support from ARPA-E, NSF, and MAST Center.

Contents

Chapter

1 Introduction **1**

2 Tin Networked Electrode Providing Enhanced Volumetric Capacity and Pressureless Operation **18**

3 High-Capacity and Highly Reversible Silicon-Tin Hybrid Anode **30**

4 A Silicon-Based Superionic Conductor for Enhanced Lithium Metal Stability **38**

5 Ultrathin Solid-State Li-Ion Electrolyte Membrane Facilitated by a Self-Healing Polymer Matrix **51**

6 Stable Lithium Deposition Using a Self-Optimizing Solid Electrolyte Composite **66**

7 FeS_2-Imbedded Mixed Conducting Matrix as a Solid Battery Cathode **78**

8 Surface Pseudocapacitive Charge Storage in Disordered $LiTiS_2$ at Solid-Solid Interfaces **96**

Bibliography **119**

Appendix

A Experimental **142**

Tables

Table

1.1 Ionic conductivities of select sulfide glass and ceramic solid electrolytes 7

2.1 Summary of Sn lithiation phases and associated volume increase factors 23

5.1 Summary of solid electrolyte-polymer composite properties 59

7.1 Exchange current, charge transfer resistance, and activation energy for FeS_2-LTS and standard systems 91

Figures

Figure

2.1 Microstructure of Sn:SSE composite anode 21

2.2 Cycling of Sn:SSE at C/10 for 50 cycles 22

2.3 Effect of external pressure on Sn lithiation 24

2.4 Effect of current on Sn lithiation kinetics 26

3.1 Cycling and voltage profiles of Sn encapsulated Si as a composite anode 32

3.2 Deconvolution of Si-Sn cycling by means of differential voltage analysis 33

3.3 Ex-situ x-ray diffraction of lithiated Si-Sn anode 35

3.4 Experimentally determined Si utilization over the course of cycling 36

4.1 Synchrotron x-ray diffraction of synthesized LSiPS and LGPS samples 40

4.2 Scanning electron microscopy images and elemental analysis in determining two phase crystalline presence in LSiPS and LGPS samples 41

4.3 Synchrotron x-ray diffraction patterns for LSiPS under different synthesis conditions 42

4.4 Arrhenius relationship of ionic conductivity in LSiPS and LGPS 43

4.5 Cyclic voltammetry of LSiPS to determine electrochemical stability in a 0 to 5 V range 44

4.6 Determination of LSiPS and LGPS stability versus lithium metal and mechanism for decomposition 46

4.7 Time dependence Nyquist plot of LSiPS stored against lithium 48

4.8 Cycling of NMC cathode using LSiPS as a solid electrolyte 49

5.1 Schematic for forming a solid electrolyte in polymer matrix membrane 53
5.2 Characteristics of polyimine polymers using stress-strain, stress relaxation, and determined bond exchange energies 55
5.3 Determination of glass transition in methyl-imine by differential scanning calorimetry 56
5.4 AC Impedance of solid electrolyte-polymer composites over a range of temperatures 57
5.5 Performance metrics of solid electrolyte-polymer composites determined by physical properties, ionic conductivity, and conductance as a function of thickness 58
5.6 DC resistance measurements as a function of time for solid electrolyte-polymer composites in contact with lithium metal 60
5.7 Electrochemical properties of solid electrolyte-polymer composite using linear sweep voltammetry and transference number 60
5.8 Microstructure of solid electrolyte-polymer composite using scanning electron microscopy 61
5.9 Rate study and long-term cycling of FeS_2 cathode using a solid electrolyte-polymer composite separator 63
5.10 Voltage profiles over cycling for experiment in Figure 5.9 64

6.1 Scanning electron microscopy image of the top surface of a cold-pressed composite of solid electrolyte and methyl-imine 68
6.2 Unidirectional galvanostatic plating of lithium in hot-pressed composites containing an increasing amount of methyl-imine 69
6.3 Unidirectional galvanostatic plating of lithium in cold-pressed composites containing an increasing amount of methyl-imine 70
6.4 The effect of current density and temperature on the amount of capacity passed before short circuit in cold-pressed composite of solid electrolyte and methyl-imine . 71
6.5 Comparison of polyethylene oxide and methyl-imine as a filler in a composite with solid electrolyte 72

6.6 Unidirectional galvanostatic plating of lithium using a variety of polyimine self-healing polymers in composites with solid electrolyte 73
6.7 Cycling test of solid electrolyte-methylimine composites at a variety of current densities 74
6.8 Schematic of the proposed mechanism for interparticle lithium growth using solid electrolyte-polyimine system 76

7.1 Schematic of charge transfer at solid interfaces in conventional solid electrode and new proposed design with mixed conductor 79
7.2 X-ray diffraction patterns of FeS_2-LTS cathode 81
7.3 Interface of FeS_2 and $LiTiS_2$ in uncycled and 10th cycle electrode imaged by high resolution transmission electron microscopy 83
7.4 Zero-loss electron energy loss spectroscopy of microstructural changes in FeS_2-LTS over cycling 84
7.5 Cyclic voltammetry of FeS_2-LTS and standard systems 86
7.6 Diffusion coefficients as determined by the galvanostatic intermittent titration technique in FeS_2-LTS and standard systems over a full discharge and charge 88
7.7 Tafel analysis detailing charge transfer mechanisms including exchange current and activation energy for sulfur and iron redox regions in FeS_2-LTS and standard systems 90
7.8 Rate study from C/10 to 4C of FeS_2-LTS and standard systems 92
7.9 Long-term cycling at C/2 and the new ability of capacity recovery for FeS_2-LTS and standard systems 94

8.1 Microstructure of disordered $LiTiS_2$ as determined by x-ray diffraction, scanning electron microscopy, and high resolution transmission electron microscopy 100
8.2 Diffusion coefficients during discharge as determined by the galvanostatic intermittent titration technique to distinguish structural differences between crystalline and disordered $LiTiS_2$ 101
8.3 Zero-loss electron energy loss spectroscopy of disordered $LiTiS_2$ particles 102

8.4 Cyclic voltammetry to determine pseudocapacitive region of disordered $LiTiS_2$ and comparison with crystalline $LiTiS_2$ . . . 104
8.5 Cyclic voltammetry between 3 and 1 V at 60°C and 120°C for crystalline and disordered $LiTiS_2$ . . . 105
8.6 Cyclic voltammetry between 2 and 1 V for crystalline $LiTiS_2$ . . . 106
8.7 Cyclic voltammetry between 2 and 1 V for disordered $LiTiS_2$ over a variety of temperatures to determine variation in capacitance . . . 107
8.8 Rate study and long-term cycling at C/2 for variants of $LiTiS_2$ . . . 108
8.9 Cycling statistics of Figure 8.8 including coulombic efficiency and voltage profiles . . 109
8.10 Function as a capacitor for disordered $LiTiS_2$ in the 2 to 1 V region including capability up to 20C . . . 110
8.11 Ex-situ x-ray photoelectron spectroscopy at different stages of lithiation for disordered $LiTiS_2$ . . . 111
8.12 Ex-situ x-ray photoelectron spectroscopy titanium and lithium states at 1 V . . . 112
8.13 Theoretical capacities as a function of domain size in $LiTiS_2$ . . . 113
8.14 Deep discharge to 10 mV to compare reaction pathways for crystalline versus disordered $LiTiS_2$ . . . 115
8.15 Effect of thickness and electrolyte selection on pseudocapacitance in disordered $LiTiS_2$ 116
8.16 Capacity recovery ability for disordered $LiTiS_2$ . . . 117
8.17 Cycling of a thick electrode of disordered $LiTiS_2$ at C/5 . . . 117

Chapter 1

Introduction

Insurgence of the solid-state battery must be viewed in the current climate of technological advancement. Demanding applications, such as portable electronics, electric vehicles, and grid energy storage, have fueled the rise of the lithium-ion battery (LIB).[1] Yet there is a level of understanding that LIB development has reached a pinnacle.[2] This is not to discredit the tremendous amount of research being performed on conventional LIBs (yet the designs and materials have been relatively unchanged for 25 years[3]), but rather to highlight inherent problems with the system. The concerns are many, however, simplistically most drawbacks can be assigned to the organic liquid electrolyte.[4] The liquid, typically a mixture of organic carbonate solvents with a dissolved lithium salt, allows for the transport of Li-ions between anode and cathode but also within electrodes themselves.[5] At its most microscopic level, the liquid electrolyte continuously degrades due to chemical decomposition to form solid electrolyte interphases (SEI) on active material surfaces.[6] At a more macroscopic level, the liquid electrolyte allows for dissolution of active material species,[7] molecular or ionic. Zooming out even further reveals the volatility of the organic electrolyte from the low flash point solvents.[8] Collectively, the problems exacerbated by a liquid electrolyte SEI can lead to safety concerns of flammability in the system. In order to deal with these problems, large auxiliary materials, such as cooling equipment must be utilized lowering the overall energy density of the battery.[9] Wide scoping studies have been performed to find a suitable liquid electrolyte replacement but typically performance is negatively affected, namely ionic mobility.[10] Therefore, drastic changes in the battery design need to take place to resolve safety issues.

Electrochemical devices replacing the liquid electrolyte with a solid material (polymers or ceramics) have been studied for decades.[11–14] With a solid phase material, flammability is relatively a low risk,[15] high temperature operation is possible,[16] self-discharge is rare,[17] undesired decomposition can be addressed,[18] and active materials are confined.[19] An ideal system would employ an electrolyte with high cation conductivity and high transference number, making glassy and ceramic solid electrolytes preferable.[20] However, with all the added benefits arise new engineering challenges on integrating a solid into a battery construction. Issues such as mechanical properties of the solid,[21] chemical stability in the presence of a metallic species,[22] chemical stability at high voltages,[23] and electrode microstructuring[24] are paramount. The first solid-state system, known as the thin-film battery, used vacuum deposition processes and had uses in applications such as microelectronics and lightweight batteries.[25] However, due to the small size and high production costs of these cells, applications are limited.[26] The push to replace a conventional LIB has resulted in development of the bulk solid-state battery. The challenges remain numerous yet this thesis details ongoing work to break down barriers to progress the solid-state battery towards commercialization.

1.1 Solid State Ionics

The term Solid State Ionics was first used in 1960 to represent the field of ion transport in solids.[27] However, the roots of 'solid electrolytes', the mechanism which allows for operation of solid-state devices, were developed over the preceding century. Detailed is a brief overview of the major milestones in the Solid State Ionics field. The goal is not to provide an in depth scientific understanding on the fundamental of solid electrolytes, but rather to set the stage for major developments leading to creation and current landscape of the solid-state battery. For additional information on the Solid State Ionics field, refer to reviews[28] and text books.[29]

Michael Faraday was the first to discover electrolytes that were not liquid, but solid. In 1834, he recorded the following observation:[30]

> 'I formerly described a substance, sulfuret of silver, whose conducting power was increased by heat; and I have since then met with another as strongly affected

> in the same way: this is fluoride of lead. When a piece of that substance, which had been fused and cooled, was introduced into the circuit of a voltaic battery, it stopped the current. Being heated, it acquired conducting powers before it was visibly red hot in daylight; and even sparks could be taken against it whilst still solid.'

This observation was the first instance in determining a transition from a poor conducting to high conducting phase within the same material - a commonality of solid electrolytes. Michael Faraday presented both the material PbF_2 and Ag_2S in his observations. Later it was determined that Ag_2S actually exhibited a mixed electronic and ionic conduction,[31] a quality which will provide much interest throughout the course of this thesis.

For the remainder of the 19th century, much of the work performed in understanding solid conduction was continuation of Michael Faraday's work. A general understanding was developed on charge carriers, electric fields, and thermodynamics within solids. Yet a general understanding on the mechanism of ionic motion still was unaddressed.

Walther Nernst provided the next great contribution in developing the Nernst equation - the fundamental relation of electrochemical potential to the chemical reactions occurring within the cell.[32] Nernst also detected ionic conduction in heterovalently doped zirconia, such as yttrium doped zirconia (YSZ), a solid conductor of oxygen and material still investigated today for a variety of applications.

In 1914, Carl Tubandt and E Lorenz discovered the unexpected conduction properties in AgI.[33] A dramatic improvement in conductivity occurred at the transition between high temperatures phases to α-AgI. The discovery of α-AgI was the starting point for the investigation of a whole new class of optimized ion conductors, namely the so-called AgI-type solid electrolytes.

In the late 1920s and early 1930s, the concept of point defects was established by Yakov Il'ich Frenkel, Walter Schottky, and Carl Wagner, including the development of point-defect thermodynamics by Schottky and Wagner. In terms of point defects, ionic (and electronic) transport in ionic crystals became easy to visualize. On an atomic scale, the relevant processes were identified as site exchanges of mobile ions with either vacancies or vacant neighboring interstitial sites. By laying

the groundwork, developments in a variety of solid electrolytes of the AgI-type class were made.

Two breakthroughs were developed in the discovery of $RbAg_4I_5$[34,35] and (1+x)Na_2O-Al_2O_3 (Na β-alumina).[36] For the first time, ionic conductivities in solids were found to be on the order of liquids. Na β-alumina is of particular interest as high room temperature conductivities could be achieved with severe disordering of the material. Finally, it became a reality that devices based on solid electrolytes would be able to be commercialized.

1.1.1 Early Solid-State Devices

The first device using a solid electrolyte to function was the Nernst lamp.[37] Developed by Walther Nernst in 1897, the Nernst lamp was an early form of a incandescent lamp. Luminescience was achieved through the heating of a YSZ rod. While the benefits of the lamp was the lack of encapsulation and vacuum to prevent oxidation, the device eventually lost to Edison's incandescent lamp. YSZ, however, found its way into a lamba probe,[38] an oxygen sensor still used today.

Cells and batteries based on the fast silver-ion conductor rubidium silver iodide, $RbAg_4I_5$, such as $Ag/RbAg_4I_5/RbI_3$, where Rb_2AgI_3 is formed in the cell reaction, were tested around 1970.[39] These cells were capable of operation at both high and low current density and over a wide range of temperatures. However, they suffered from rather low energy content per unit weight (about 5 Wh kg^1) and have, therefore, never been commercially developed.

Sodium-sulfur cells,[40] with ceramic beta alumina serving as solid electrolyte between the molten sodium anode and the molten sulfur cathode, were for a long while regarded as promising units for electrotraction, since they offered energy densities and therefore, automobile operating ranges that surpassed the possibilities of conventional lead-acid or nickel-cadmium accumulators roughly by a factor of 10. The favored beta alumina variants included the lithium- and magnesium-stabilized sodium β"-aluminas, which are similar to Na β-alumina, but somewhat different in composition and structure.

In contrast to $RbAg_4I_5$, lithium iodide, LiI, is a poor ion conductor, with a conductivity of only about 10^{-7} S cm^{-1} at room temperature.[41] Nevertheless, this did not prevent the successful

development of all-solid-state cardiac pacemaker batteries employing this solid electrolyte.[42] Since then, the LiI battery has established an excellent record in reliability. Indeed, millions of people have benefited from implantable pacemaker devices containing LiI batteries.

Electrochromic devices in the 1970s demostrated the variety of applications that could be developed with the use of a solid conductor.[43]

1.2 Solid Electrolytes

The electrolyte is the most important part of the solid-state battery. Solid electrolytes are known mainly for their fast and efficient ion transport properties. The following are some of the important general parameters that must be considered in selection of the electrolyte.

(i) *Chemical and thermal stability* For prolonged operation, undesirable reactions should be avoided at the interfaces of electrodes and electrolyte. This generally equates to a electrochemical window of 0 to 5 V.[44] Recently it was shown that almost all solid electrolytes will decompose against a lithium metal surface.[45,46] The property of the interface is of specific importance and explored further in Chapter 4. Therefore, chemical and electrochemical stability is an essential property in a solid electrolyte. Versatility of the solid-state battery dictates that it must be able to work in a broad temperature range. Usually, lithium based rechargeable batteries used for military purposes are subjected to a temperature range of -50°C to 80°C, and the electrolyte must be able to function perfectly in this temperature range without showing any thermal degradation.[47] To fully take advantage of a diverse range of applications, thermal stability up to 200°C is also of interest.[48]

(ii) *Ionic Conductivity* Li-ion conductivity is an extremely important parameter in all electrolyte systems. Conductivity is a function of ion mobility which expresses transport in a frequency of hops of the ion.[49] A high conductivity leads to greater power density capabilities. Solid electrolytes have recently reached the same order of conductivity that liquid electrolytes exhibit making them competitive.[50] Solid electrolytes have Arrhenius relations of conductivity with temperature for a given crystallographic phase. Therefore increased temperature actually has a dramatic im-

provement on the functions of many solid-state batteries.

(iii) *Ion transference number* The ion transference or transport number indicates the contribution of the different ions toward the total electric current carried by the electrolyte.[51] The ion transference number of the solid-state electrolyte should be close to unity or even, ideally, exactly unity.[52] This is because the main purpose of the electrolyte is to allow the flow of the ions (cations) and prevent any electrons from traveling. The transference number is of particular importance to concentration gradients developed throughout the electrolyte - a high transference number reducing concentration polarization. Liquid electrolytes typically have transference numbers on the order of 0.2 to 0.5.[53] Thus a solid electrolyte typically has more efficient transport of the cations, reduction in the concentration of polarization, and consequently higher power density.

(iv) *Mechanical strength* Mechanical properties of solid electrolytes are one of the more indiscriminate qualities. The mechanical strength will be incredibly important depending on the processing method, a more ductile electrolyte in favor of dynamic compaction methodologies. Additionally, if high volume expansion active materials are used, a more elastic or deformable electrolyte is favored.

The types of solid electrolytes explored in the upcoming sections must meet the criteria of either glass or ceramic in phase and only conductive of lithium cations.

1.2.1 Sulfide Solid Electrolytes

Studies on ionic conduction in sulfides started in glasses.[54] Because the high polarizability of sulfide ions weakens the interaction between the anions and the lithium ions, sulfides inherently tend to show fast ionic conduction. In fact, the highest conductivities observed among sulfide glasses, e.g. LiI - Li_2S - P_2S_5[55] and LiI - Li_2S - B_2S_3,[56] were already of the order of 10^{-3} S cm^{-1} in the early 1980s, as listed in Table 1. Besides the high ionic conductivity, sulfide electrolytes have the following advantages: the first is that they show high ionic conductivity without presence of transition metal elements that narrow the electrochemical window, second is the low grain-boundary resistance. Contrary to oxide or oxysalt solid electrolytes, sulfide solid electrolytes show small grain-

boundary resistance even in a cold-pressed pellet.[57] That is, the sintering process is not necessary to connect ionic path between the particles. This feature is convenient for constructing bulk-type batteries, because the batteries can be assembled by pressing powders of batteries materials into a three-layered structure of anode/electrolyte/cathode.[58] Because sulfide systems have advantages for fabricating bulk-type solid-state batteries, the development of Li-ion batteries triggered many studies on sulfide electrolytes in the 1990's. Various kinds of sulfide glasses doped with oxysalts were developed,[59,60] and in the 21st century, conductivities of the order of 10 $^{-3}$ S cm^{-1} have been achieved also in crystalline sulfides.

Table 1.1: Lithium-ion conductivities of select sulfide glass and ceramic solid electrolytes.

Electrolyte	$\sigma_{25^\circ C}$ (mS cm^{-1})	Preparation Method	Reference
Glass			
$Li_2S - GeS_2$	0.04	Melt-quench: Water	[54]
$Li_2S - P_2S_5$	0.1	Melt-quench: Water	[55]
$Li_2S - P_2S_5 - LiI$	1.7	Melt-quench: Water	[55]
$Li_2S - P_2S_5 - Li_2O$	2.7	Melt-quench: Water	[61]
$Li_2S - B_2S_3$	0.1	Melt-quench: Water	[56]
$Li_2S - B_2S_3 - LiI$	1.7	Melt-quench: Water	[56]
$Li_2S - SiS_2$	0.15	Mechanical milling	[62]
$Li_2S - SiS_2 - LiI$	1.8	Melt-quench: Twin-roller	[63]
$Li_2S - SiS_2 - Li_3PO_4$	1.5	Melt-quench: Twin-roller	[64]
Crystalline			
$\gamma - Li_3PS_4$	0.0004	Melt-crystallization	[65]
$\beta - Li_3PS_4$	0.16	Wet-chemical	[66]
Li_4GeS_4	0.0002	Melt-crystallization	[67]
Li_4SnS_4	0.07	Melt-crystallization	[68]
$Li_{4-x}M_{1-x}P_xS_4$	2.2	Melt-crystallization	[69]
$Li_7P_3S_{11}$	3.2	Solid state reaction	[70]
Li_6PS_5X	1.33	Solid state reaction	[71]
$Li_{10}GeP_2S_{12}$	12	Solid state reaction	[72]

Li_4GeS_4 was found to be a solid electrolyte in 2000.[67] Although the conductivity is only 2.0 x 10 $^{-7}$ S cm^{-1}, cation substitution in this material has given countless solid solutions. They are categorized into thio-Lithium Super Ionic Conductors (LISICON) family, because they have *c*-Li_3PO_4-type structure oxysalts typified by LISICON. Aliovalent substitution introducing lithium-

ion vacancies or interstitial lithium ions increased the conductivity,[73] and the conductivity has reached 2.2 x 10^{-3} S cm^{-1} at a composition of $Li_{3.25}Ge_{0.25}P_{0.75}S_4$.[69]

Another high conductivity was found in glass ceramic. Fast ion-conducting phase is precipitated as a primary crystal in the crystallization process of a supercooled Ag^+-ion-conducting glass.[74] A lithium-ion-conducting sulfide glass also showed a similar phenomenon, although the mechanism may be different. Precipitation of a metastable crystalline phase increases the conductivity from 5.4 x 10 $^{-5}$ S cm^{-1} in $70Li_2S - 30P_2S_5$ glass to 3.2 x 10^{-3} S cm^{-1} with a very low activation energy of conduction of 12 kJ mol^{-1} in the glass-ceramic phase.[70]

Very recently, the highest ionic conductivity among Li-ion conductive solid electrolytes of 1.2 x 10^{-2} S cm^{-1} was observed in $Li_{10}GeP_2S_{12}$.[72] Although the paper claims that electric conductivity is comparable to that of organic solvent liquid electrolyte, Li-ion conductivity is much higher, when taking into account that the transport number of Li ions is unity.

Other new crystalline solid electrolytes developed are based on doping with halogens. These include the argyrodite phase Li_6PS_5X where X = Cl, Br, I[71,75] and doped conductor $Li_7P_2S_8I$.[76] The new solid electrolytes demonstrate high chemical stability in contact with lithium which is most likely the result of a favorable passivation layer containing a lithium halide species.

1.2.2 Ionic Conduction Mechanism

Ionic transport in crystals is described classically by the vacancy, interstitial, and interstitialcy models. The vacancy mechanism involves the motion of a ion through a lattice by successive ion hops in the direction opposite to vacancy motion. In the interstitial model an ion moves through a series of interstitial sites. The interstitialcy mechanism involves cooperative motion in which a lattice ion hops to an interstitial site and an interstitial ion fills the remaining vacancy. For all these mechanisms, ionic conductivity in crystals can usually be described by an Arrhenius equation. Ionic conductivity is extremely sensitive to the value of the activation energy.

For a solid to have high ionic conductivity at temperatures much lower than its melting point, it must have three characteristics: a high concentration of potential charge carriers, a high

concentration of vacancies or interstitial sites, and a low activation energy for ion hopping from filled to unfilled sites.

In comparison with crystalline materials, the understanding of transport processes in glasses is complicated by the inherent structural disorder in these materials.[77] Vacancies are developed in glasses by breaking bonds between glass former and modifier developing polar units.[78] Using the $Li_2S - P_2S_5$ system as an example, the bridging sulfur in P_2S_5 are modified to become nonbridging sulfur, essentially an ionic species.[79] With increasing amount of Li_2S, the short range order of the glass changes; high concentrations yield an underlying PS_4^{3-} unit that can coordinate with up to 3 Li ions.[80] The high number of interstitial sites created by polar sulfurs coupled with the large number of charge carriers in Li explain how such high conductivities can be achieved with the chalcogenide glasses.[81]

1.3 Solid-State Batteries

1.3.1 Thin-Film Solid-State Batteries

One of the earliest thin-film solid-state batteries to have been studied was produced by Hitachi Co., Japan.[25] The battery was called the "all-solid-state thin-film battery" and incorporated a TiS_2 cathode, a metallic lithium anode, and a $Li_{3.6}Si_{0.6}P_{0.4}O_4$ thin-film electrolyte prepared by the RF sputtering technique. However, it was not immediately deployed commercially, as it was not sufficient for the larger electronic devices prevalent at that time. NTT Co., Japan, achieved further advances in thin-film solid-state batteries by developing a $Li_{3.4}V_{0.6}Si_{0.4}O_4$ glassy electrolyte also by the RF sputtering technique.[82] Eveready Battery Co. and Bellcore Co. have developed solid-state batteries using sulfide glasses ($Li_4P_2S_7$ and $Li_3PO_4 - P_2S_5$) as electrolytes.[83] More recently, Baba et al. developed the rocking chair type solid-state battery using lithium phosphorus oxynitride (LiPON) electrolyte, $Li_xV_2O_5$ anode, and $LiMn_2O_4$ cathode, by RF sputtering.[84] They have also developed solid-state batteries without using a Li anode (for example by using a V_2O_5 anode) and have been able to obtain capacities of approximately 10 μAh cm^{-2}.[85]

A variety of electrodes have been explored for use in thin-film batteries. For anodes, these

include Li-based alloys with Al,[86] Sn,[87] and Si[88] among others. However, the real advantage of the thin-film battery is the ability to use metallic lithium as the anode.[26] This provides a large operating voltage and specific capacity leading to a greater energy density. It is unclear though if the mechanism of reversible lithium usage is attributed to the small capacities passed or high relative density of the deposited solid electrolyte. Cathodes explored include classic layered structures $LiCoO_2$,[89] spinels $LiMnO_2$,[90] olivenes $LiFePO_4$,[91] chalcogenides TiS_2,[25] mixed conductors V_2O_5,[84] and new high voltage class $LiCoMnO_4$.[92]

LIPON is the solid electrolyte of choice for thin-film batteries.[93] The solid electrolyte while having a very low ionic conductivity of 1 x 10^{-6} S cm^{-1}, claimed to originally have a stable voltage from 0 to 5.5 V. Recently, however, it was shown that LIPON actually degrades against metallic Li and high voltage cathodes.[45,46] The work highlighted the necessity of the desired decomposition layers chemistry leading to insulating electronic conductivity and high ionic conductivity.[46]

While thin-film batteries provide limited applications due to small capacities, they provide an excellent tool for fundamental studies of material interactions and degradations. The author points to the following comprehensive reviews for more information.[94,95]

1.3.2 Bulk Solid-State Batteries

As thin-film batteries can only deliver 10 μAh cm^{-2}, a design was needed for solid batteries to be able to compete with conventional, liquid-based LIB with capacities closer to 1 mAh cm^{-2}, a 2-order of magnitude difference. The traditional method for measuring ionic conductivity in Li-containing solid electrolytes involved the grinding of powders, pressing at a given pressure, and attaching blocking electrodes. Blocking electrodes could either be Li, TiS_2, Pt, Ag, C, or some or method of making a high-quality interface between electrolyte and electrode. This method was extrapolated to electrode manufacturing by pressing a composite of active material, solid electrolyte, and conductive additive onto the pressed electrolyte layer - resulting in the dynamic compaction design.[58] Electrode length scales could now be produced on the micron scale leading to much larger derived capacities. The dynamic compaction design highlighted the necessity for deformable solid

electrolytes to minimize charge transfer resistance in the cell and thus the sulfide solid electrolytes received the majority of attention. When referring to a "bulk solid-state battery" within this thesis, this is referring to those prepared by dynamic compaction, whether cold-pressing or hot-pressing. A variety of other techniques will also be explored in this thesis to create batteries using solid electrolytes and electrode thicknesses greater than 1 μm.

1.4 Design Challenges and Considerations

The success of state-of-the-art Li-ion battery may be attributed not only to the use of suitable electrode materials, but also to the carbonate-based liquid electrolytes, with their kinetically wide electrochemical windows and their excellent compatibility with the electrode materials. For example, fully reversible intercalation-deintercalation in $LiVS_2$ became possible when using the electrolyte which is commonly used nowadays, namely 1 M LiPF6 in EC:DEC (1:1 vol. ratio), whereas the traditional electrolyte used for the studies performed in the 1970s, 1 M $LiClO_4$ in PC, had a detrimental effect on the performance of $LiVS_2$.[96] Understanding the phenomena taking place at the interface between the sulfide solid electrolytes and the electrode materials is crucial. In addition, new opportunities may arise to (re)investigate the compatibility of already known or innovative electrode materials with the sulfide solid electrolytes.

1.4.1 Cathode

As for the conventional Li-ion batteries using liquid electrolytes, the layered or spinel Li_xMO_2 (M = Co, Ni, Mn) cathode materials are considered as viable candidates for solid-state lithium batteries because of their highly reversible intercalation-deintercalation reaction with low dimensional change and high operating potential. To date, many Li_xMO_2 materials, including $LiCoO_2$,[72,97,98] $Li[Ni, Mn, Co]O_2$,[99,100] and $LiMn_2O_4$,[101] have been tested in solid-state batteries. However, the bare Li_xMO_2 showed much lower capacity than the theoretical one, a large amount of irreversible reaction during charging, and a high overpotential.[102] The poor performance of Li_xMO_2 originates from the intrinsically low oxidation onset potential ($\sim$ 3 V vs. Li^+/Li) of the sulfide solid electroyltes[103,104] as confirmed by the abnormal sloping plateau starting at $\sim$ 2.3 - 2.4 V (vs. LiIn).

Tatsumisago and co-workers investigated the interface between $LiCoO_2$ and $Li_2S - P_2S_5$ solid electrolyte after charging using transmission electron microscopy.[97] It was observed that the elements originally found in $LiCoO_2$ and $Li_2S - P_2S_5$ solid electrolyte mutually diffuse. The formation of a new interfacial layer, mainly consisting of cobalt and sulfur, was suggested to be the cause of the poor performance. Takada and co-workers adopted the space-charge layer theory[105] to explain the poor behavior at the interface between $LiCoO_2$ and the sulfide solid electrolyte.[98,106,107] Depletion of lithium in the solid electrolyte near the Li_xMO_2 accounts for the huge interfacial resistance, and is reasonably caused by the diffusion of lithium triggered by the large difference in chemical potentials between Li_xMO_2 and the sulfide materials. Recently, it was predicted through density functional theory (DFT) simulation that breakdown of the sulfide solid electrolyte with $LiCoO_2$ could result in a mixed conducting species of cobalt sulfide.[108]

As already reported by numerous publications regarding oxide cathodes for Li-ion batteries containing liquid electrolytes,[109,110] surface coatings made using various metal oxides, such as $LiNbO_3$,[106] $Li_4Ti_5O_{12}$,[111] Li_2SiO_3,[112] Al_2O_3,[113] and $BaTiO_3$,[107] when applied on Li_xMO_2, turned out to be effective for significantly reducing the interfacial resistance in solid-state batteries, thereby improving their electrochemical performance. The mechanism underlying the observed enhancement can be either the suppression of chemical reactions between the sulfide and the oxide layers, or the shielding effect provided by the oxide coatings against the noble potential of the Li_xMO_2 cathodes.[114] It should be emphasized that typically, the coatings with electron-insulating and ion-conducting oxide materials resulted in improvement of performance. Enhanced performance of $LiCoO_2$ by electronically conductive coatings with metal sulfides, such as NiS and CoS, were also reported.[115]

Sulfur is a highly sought after cathode material due to high theoretical capacity. The formation of a nanocomposite structure from the combination of sulfur or Li_2S with carbon is the most common strategy to improve the performance of the cathode in either liquid[116] or solid state.[117] The size of sulfur or Li_2S particles is critical, not only to relieve the stresses induced by the volume changes during charge and discharge, but also to maximize the extension of the electrically active

domains. Carbon can provide conduction pathways for the insulating sulfur or Li_2S, and at the same time, can act as a buffering phase for the volume change. Nanostructured sulfur-carbon or Li_2S-carbon materials were prepared by ball-milling[118–120] and gas-phase mixing (or melt diffusion mixing).[121,122] Notably, the intimate ionic contacts achieved by ball-milling between the sulfur-carbon or Li_2S-carbon and the solid electrolyte are critical for the enhancement of the capacity and rate capability.

Notably, solid-state batteries provide a new opportunity to investigate, under a different perspective, electrode materials that were found inappropriate or simply not good enough for conventional Li-ion batteries. Lithium intercalation-deintercalation in the layered transition metal chalcogenides was extensively investigated in the early 1970s. However, transition metal chalcogenides were abandoned after the emergence of Li_xMO_2, which is lighter and allows operation at higher voltages than sulfides. However, the transition metal sulfides may be revisited for solid-state battery because of their mild operating voltages ($\sim$ 2 - 3 V vs. Li^+/Li) and potentially good compatibility between different types of sulfides, creating an effective interface.[103] In particular, TiS_2[123] and Li_xTiS_2[124] were reported to show good cycling performance, with reversible capacities close to the theoretical one ($TiS_2 + Li^+ + e^- \rightarrow LiTiS_2$, 239mAh g^{-1}). The Chevrel-phase compound, $(Cu_x)Mo_6S_{8-y}$, also exhibited excellent cycle life.[125] The outstanding performance of TiS_2 and $(Cu_x)Mo_6S_{8-y}$ is associated with their metallic nature, their reversible intercalation/deintercalation, high Li^+ ion diffusivity, and so on. Lee and co-workers investigated the electrochemical reactivity of pyrite FeS_2 as a solid-state cathode.[126] Excellent performance demonstrates reversibility due to active material confinement and lack of polysulfide dissolution, common problems in cells containing liquid electrolytes.

For a more comprehensive list of more cathodes tested in solid-state, refer to reviews.[127]

1.4.2 Anode

A variety of anode materials have been explored in solid-state. The first being graphite due to the wide spread use in conventional cells.[128,129] Other common anodes include the spinel

structured $Li_4Ti_5O_{12}$,[130] group IV alloy materials such as Si, Ge, Sn,[131–133] metal oxides such as Fe_2O_3,[134] and metal phosphides (e.g., Sn_4P_3, NiP_2).[135] Li-alloy materials, such as In and Al, can be good alternatives to replace lithium metal in the solid-state. All-solid-state test cells, using a Li-In alloy electrode as the counter/reference electrode, are frequently used.[72,97] Those are similar to the conventional liquid electrolyte-based half-cells using lithium metal in that Li-In alloy provides an excess lithium source, a flat voltage plateau at 0.62 V (vs. Li^+/Li) for the range of $0 < x < 1$ in Li_xIn, and fast charge transfer kinetics.[59,136] Li-Al alloy (0.38V vs. Li^+/Li) has been also examined.[137]

Lithium Metal

Lithium metal is supposed to be an ideal anode for all types of lithium secondary batteries, including alternative batteries such as Li-S and Li-air batteries, because of its high theoretical capacity (3862 mAh g^{-1}), the lowest operating potential among all the known anode materials, its metallic nature, and the fact that it avoids the use of pre-lithiated cathode materials.[138] However, a severe safety concern, associated with eventual internal short circuits caused by the dendritic growth of lithium during repeated deposition and dissolution cycles, brought the ban of lithium metal in commercially available lithium ion batteries.[139] The solid-state battery, which is free from flammable components, can take advantage of the use of lithium metal as the anode, maximizing its energy density.

Two issues, however, must be addressed. First, solid-state batteries also suffer from the internal short circuits caused by abnormal lithium growth. In the experiments carried out using the Li_2S - P_2S_5 solid electrolyte pellet, it was observed that lithium metal tends to grow in the voids and along the particle boundaries.[140] As a result, a sign of internal short circuit manifests as a sudden drop to zero in the voltage profile. Second, the chemical stability of the solid electrolytes in contact with lithium metal can be affected by its composition. Jung and co-workers reported that the structure of LGPS is severely altered at low voltage ranges, likely generating a Li_2S phase.[141] The poor chemical stability of the solid electrolyte in contact with lithium was also found in the As-doped

Li_4SnS_4, in which tin acts as a reducing center.[142] A protective coating on $Li_{3.833}Sn_{0.833}As_{0.166}S_4$, made with $3LiBH_4$ - LiI, enabled the reversible cycling of lithium metal. A thin In layer prepared by vacuum evaporation can be employed to achieve good cyclability of $Li/Li_4Ti_5O_{12}$ cells at high current density, due to the intimate contacts formed at the electrolyte/Li interface.[118] Similar concepts has been explored with Au coatings.[143] However, electronically conductive surface coatings will not prevent lithium from depositing directly on top of the coating nor prevent electrolytic decomposition. Therefore developing an artificial, electronically insulating/ionically conductive interface, will be paramount to enable lithium metal. The third issue is the large volume changes associated with lithium. Due to a lack of concentration gradient driving diffusion, large voids will develop at the interface of electrolyte and lithium contributing to resistance rise; these are entitled constriction resistance, a concept long known.[144–147] Therefore pressure must be applied to prevent the increase in resistance.[148] Enabling the use of lithium metal as the anode will remain a challenge until significant developments of composition, surface modifications, and pelletized microstructure of solid electrolytes are made.

1.4.3 Electrode Structuring

Achieving a good electrical connection between the current collector and each of the active materials is of prime importance in the fabrication of a composite electrode, not only for conventional lithium ion batteries, but also for solid-state batteries. For example, the electrochemical performance of $LiCoO_2$ in the solid-state is significantly affected by the conductive additives.[70] In the case of solid-state batteries, however, the design of composite electrodes is more complicated than for conventional lithium ion batteries because many factors contribute to significantly affect the ionic conduction pathways, including morphology, percolation of solid electrolytes, and contacts between the active materials and the solid electrolyte. For example, the capacity of $LiCoO_2$/In solid-state cells is highly dependent on the composition of the composite electrodes.[70] In contrast, liquid electrolytes can easily be absorbed into the porous structure of composite electrodes, wetting almost all the exposed surfaces of the active materials.

In the majority of publications regarding the composite electrodes of Li_xMO_2, such as $LiCoO_2$, a 30 - 65 wt % of solid electrolyte is included to ensure the creation of facile ionic conduction pathways.[70,72,97–100] Obviously, the very high content of solid electrolyte may severely reduce the energy density of battery. To overcome this issue, one ideal structure of the composite electrode should contain the active materials coated by layers of solid electrolyte as uniform as possible, while maintaining electronically conductive pathways. Tatsumisago and co-workers reported that a thin Li_2S - P_2S_5 film can be deposited on electrode materials by pulsed laser deposition (PLD).[149] As a proof of concept, the authors successfully demonstrated that a solid electrolyte-coated $LiCoO_2$ could work without any addition of solid electrolyte powders to the positive electrode layer. However, as the expensive PLD technique is far from being a viable solution for practical applications, innovative approaches are needed. Wet coating of Li_2S - P_2S_5 using N-methyl formamide, which has the advantage of fully dissolving Li_2S - P_2S_5, was tried.[150] However, the improvement in the performance of the cell was not significant, since the conductivity was only 2.6 x 10^{-6} S cm^{-1}. It was also demonstrated that a much higher conductivity (1.82 x 10^{-4} S cm^{-1}) could be obtained for thio-LISICON-like $Li_{3.25}Ge_{0.25}P_{0.75}S_4$ using Li_2S, P_2S_5, and GeS_2 as precursors, and employing a solution method with anhydrous hydrazine.[151] However, anhydrous hydrazine is extremely dangerous, thus discouraging further developments. Although the two dimensional contacts between the active materials and the sulfide solid electrolytes are simply made by cold-pressing, it is worth noting that hot-pressing at temperatures above the glass transition temperature can deform and enable the merging of the sulfide particles, forming poreless, dense pellets.[152–154] Consequently, hot-pressing of composite electrodes containing sulfide solid electrolytes resulted in an increased utilization of the active materials, as demonstrated in the case of $Li_4Ti_5O_{12}$.[154] However, the trade-off of hot-pressing is the massive interfacial reaction observed in the case of $LiCoO_2$.[154] A protective coating on $LiCoO_2$ by $LiNbO_3$ may partially suppress the interfacial reaction occurring during hot-pressing.

1.5 Overview of Thesis

The Thesis is organized in the following manner:

Chapters 2 and 3 relate to the anode. In particular new materials, that were previously found to be incompatible in liquid cells, are explored as solid electrodes. Design considerations such as the amount of external pressure for operation are investigated for more commercially viable usage.

Chapter 4 is associated with the solid electrolyte chemistry. The highlight in this chapter is to cast light on not only developing highly conductive crystals, but to consider properties such as chemical stability in contact with lithium.

Chapters 5 and 6 are related to the battery design, in particular, the thickness of the solid electrolyte layer. After developing a new processing technique, it was found to have extraordinary properties for the optimized deposition of lithium.

Chapters 7 and 8 deal with the cathode. Fundamentals of charge transfer take place is look for ways of completely removing the solid electrolyte additive within the composite. In the final chapter, a new mechanism of charge storage is revealed which we anticipate will open up a new line of research.

Chapter 2

Tin Networked Electrode Providing Enhanced Volumetric Capacity and Pressureless Operation

2.1 Introduction

In 1997, Fuji announced a tin (Sn)-based amorphous composite oxide material for commercial Li-ion batteries.[155] Ensuing anode deployments include the Sony developed Sn-based compound (Sn-Co-C) in 2005.[156] Although these were the first commercial deployments of Sn-based anodes, Sn has been extensively studied for decades as a candidate in rechargeable Li-ion batteries because of its substantial lithium storage capabilities and quicker charging times.[157] Despite the theoretical capacity of Sn being lower than the currently spotlighted silicon (Si) anode, Sn has exceptionally appealing features: high gravimetric and volumetric capacity (959 mAh g^{-1} and 2,476 mAh mL^{-1} for 4.25 Li-ions),[158] excellent electrical conductivity (9.17 x 10^6 S m^{-1}), and room temperature Li-ion diffusivity (5.9 x 10^{-7} cm^2 s^{-1} of $Li_{4.4}Sn$).[159] The commercialized Sn-Co-C anode by Sony provides a significant capacity advantage over the currently utilized graphite anode material (372 mAh g^{-1}). However, wide use of the Sn-Co-C anode has been limited due to the high cost and environmental concerns about cobalt. Iron and nickel have been introduced as replacements for cobalt forming amorphous Sn-Fe and Sn-Ni with similar electrochemical properties to the Sn-Co alloy.[160–164] Despite the low cost and high capacity of the Sn-Fe and Sn-Ni anodes, poor cycling stability and coulombic efficiency (CE) hinder their practical use in Li-ion batteries. These drawbacks mainly result from the notorious volume change of Sn (255% when 4.25 Li-ion inserted),[158,165] leading to

a loss of electric contact, pulverization, and cracking.[166] Therefore, controlling the microstructure of the expandable active material during lithiation/delithiation processes is a key point to realize a high energy-dense Li-ion battery using Sn-based anode materials.

Recently, Molina Piper et al. reported the effect of compressive stress on the electrochemical performance of a Si anode in an all-solid-state Li-ion cell, which similarly suffers from pulverization due to immense volume changes.[167] By applying external compressive stress to the silicon/solid-state electrolyte (SSE) composite anode, free volume expansion of Si as well as solid-solid interfaces between the active material, SSE, and conductive additive were effectively controlled, thereby significantly reducing capacity fade. Generally, interfacial impedance in solid-state cells is much higher than that of conventional liquid electrolyte cell because the junction is limited to the small contact area between SSE and active material particles.[168] Therefore, achieving and preserving absolute interfaces between SSE and active material during the cycling process will be one of the most critical points for highly reversible all-solid-sate Li-ion batteries.

To this resolve, exploration of Sn-based anodes in the solid-state configuration has been rather limited. To create the ionically conductive network, studies have focused on integrating Sn into glasses or crystals that act as conversion materials.[133,169,170] These solutions usually result in very low amounts of Sn active material mass loading and still require significant amounts of conductive additive, essentially nullifying the attractive volumetric capacity from Sn. Additionally, almost all solid-state studies do not address the fact that these composite anodes, or even cathodes, require large amounts of external pressure for proper operation.[171] Usage of a polymeric binder in solid-state actually contributes to worse performance.[172] Therefore, to ensure sustained particle-particle contact, external pressure is necessary in the range of a few MPa. This is not a realistic possibility for a commercial solid-state design. Thus, future work on solid-state architectures should focus on microstructural design of the electrode to address this issue.

In this study, we aim to demonstrate improved cycling performance and reduced stack pressure of a high capacity Sn metal-based anode in an all-solid-state Li-ion battery. As Sn is one of the most ductile and malleable metals, we develop an interpenetrating network of electrically

conductive Sn with ionically conductive SSE. The absence of conductive additive, such as carbon black, allows for enhanced cycle life as there is no concern for active material segregation. The composite anode delivers near theoretical capacity on the first cycle with over a 90% CE; subsequently a capacity in excess of 800 mAh g^{-1} of Sn (560 mAh g^{-1} electrode) is established with a CE over 99%. Interestingly, due to the interplay between expansive Sn and rigid SSE, the cell can be cycled reversibly near ambient pressure conditions. Finally, we formulate a correlation between pressure, current density, and the overall effect on Sn delithiation kinetics. This study provides an interesting landscape of examination expansion of active materials into rigid solid electrolytes compared to a fluid liquid electrolyte.

2.2 Results and Discussion

Work in this section has been presented in the 2015 publication.[173] To determine the microstructure of the composite electrode, we used focused ion beam (FIB) to prepare a cross-sectional image of the uncycled Sn:SSE electrode (Figure 2.1). Due to its inherent ductility, Sn powder forms a dense, long-range network filling the porous SSE green compact. This leads to a continual interface between Sn active material and SSE where electrochemical reactions occur. It is evident that very little Sn is electrically isolated. Additionally, pores are apparent in the electrolyte layer, whereas the composite anode appears almost completely dense. In Figure 2.1b and 2.1c, energy dispersive spectroscopy (EDS) elemental maps and point spectra from Sn and SSE confirms the interpenetrating three-dimensional (3D) network structure. It has been well documented and highlighted in our previous studies that intimate solid-solid interfaces between active material and SSE are ideal for Li-ion and electron transport during discharge-charge processes.[168]

Figure 2.2a presents performance of the composite anode over the first 50 cycles between 0.005 and 1.8 V (vs. Li^+/Li at a C/10-rate (100 mA g^{-1}). Corresponding voltage profiles of the Sn:SSE electrode are shown in Figure 2.2b. A voltage hold was applied at 0.005 V until a current of C/100 is reached to allow for full lithiation. On the first cycle, the Sn anode delivers a discharge capacity of 990 mAh g^{-1} (respect to Sn) with a reversible charge capacity of 912 mAh g^{-1} exhibiting a high

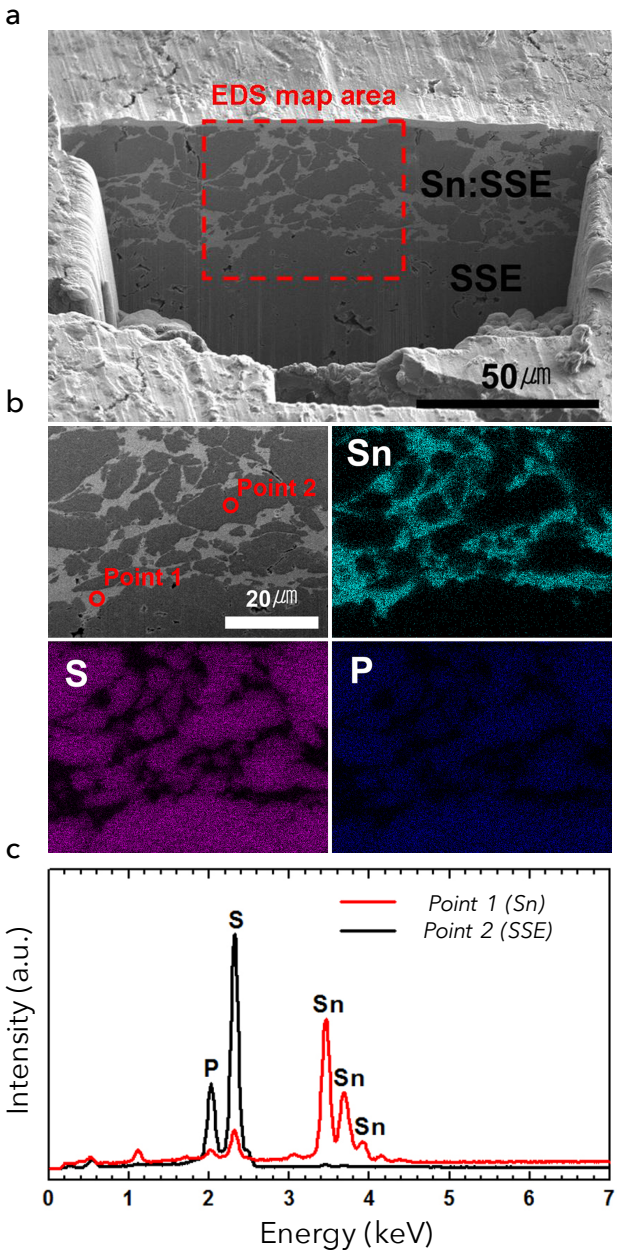

Figure 2.1: (a) FIB cross section view of pressed Sn:SSE composite anode on top of SSE separator layer, (b) EDS elemental maps indicating intertwining networked structure of Sn and SSE and (c) point EDS spectrum confirming presence of Sn and SSE.

initial CE of 92%. This is an interesting result as charge recovery in Sn cells is usually very poor.[174] A small irreversible capacity was identified at 1.1 V upon initial lithiation. This can be attributed to the decomposition of any native SnO layer as this is in line with previous reports and disappears on subsequent cycles.[165] Subtracting out this contribution, the Sn alloys with 4.2 moles of lithium;

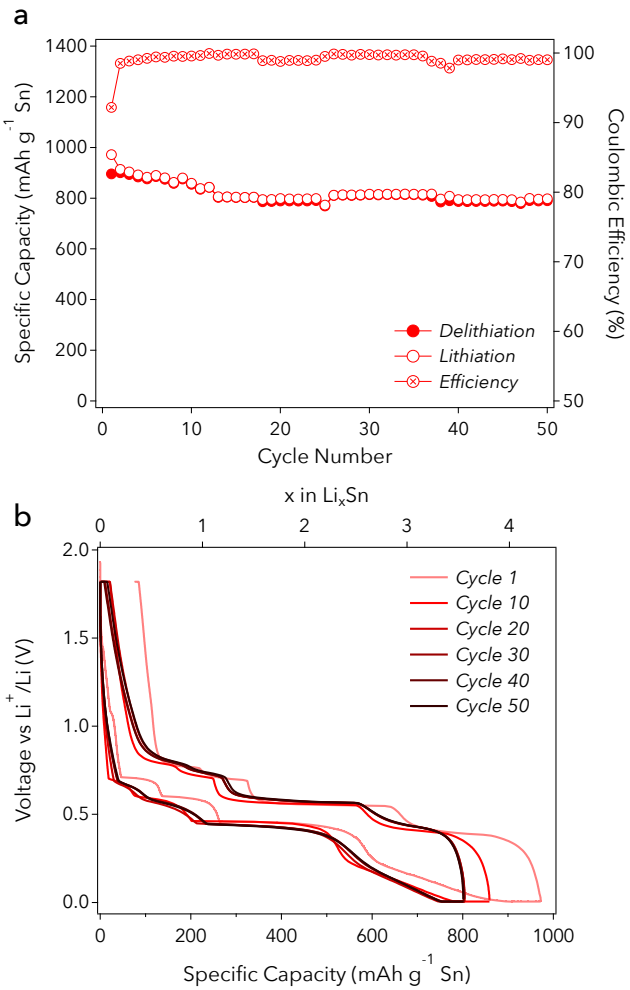

Figure 2.2: (a) Cycle performance and coulombic efficiency of Sn:SSE anode in all-solid-state Li-ion battery at 60°C with C/10-rate (100 mA g^{-1}) and (b) Corresponding voltage profiles of the Sn:SSE anode vs. LiIn counter electrode (converted to vs. Li). It is clear that formation of a stable structure occurs in the first 10 cycles.

this is close to theoretical capacity of Sn (959 mAh g^{-1}) and suggests the final crystallographic phase is the refined $Li_{17}Sn_4$ phase.[158,175,176] The exceptional initial CE also suggests that the side reactions are nonexistent. This is a different characteristic to conventional liquid electrolyte cells containing Sn which exhibit a continual formation of a solid electrolyte interphase (SEI) layer at the interface between active material and electrolyte.[177]

For ease of reference, the voltage profile has been separated into distinct regions over the course of lithiation and delithiation and outlined in Table 2.1. These correspond to the well-defined phase transformations of the Li-Sn alloy. The rest of this paper will use the region identifiers for

Table 2.1: Summary of observed electrochemical lithiation regions of Sn in solid-state. Crystallographic phases and volume increase factors are assigned from previous studies.[158,165,178]

Region	Potential vs. Li (V)	x in Li_xSn	Crystallographic Phases	Volume Increase Factor
1	0.70 - 0.60	0 - 0.4	Sn, Li_2Sn_5	1.23
2	0.60 - 0.45	0.4 - 1.0	Li_2Sn_5,LiSn	1.53
3	0.45 - 0.25	1.0 - 2.6	LiSn, Li_7Sn_3 Li_5Sn_2, $Li_{13}Sn_5$	2.81
4	0.25 - 0.01	2.6 - 3.5	$Li_{13}Sn_5$, Li_7Sn_2	2.98
5	0.01 - 0.005	3.5 - 4.25	Li_7Sn_2, $Li_{17}Sn_4$	3.55

simplicity. Due to operation at 60°C, the identified potentials are actually closer to thermodynamic equilibrium than reports of other tin-based liquid cells.[178] Surprisingly, the Sn composite displays exceptional specific capacity (> 800 mAh g^{-1} Sn) and CE_{avg} (99.2%) for the subsequent 50 cycles. From Figure 2.1a, we estimate an electrode thickness of 25 μm, which translates to a volumetric capacity of 844 Ah L^{-1}. This is on the order of state-of-the-art silicon anodes in liquid cells.[179] Outstanding capacity retention of the composite suggests the preservation of the networked microstructure, guaranteeing electric and ionic pathways with little Sn segregation.

As mentioned previously, almost all solid-state battery constructions require an external pressure to ensure particle contact throughout the course of cycling. This pressure is required as the use of binders has shown to have an adverse effect of coating the solid electrolyte particles and increasing interfacial resistance. However, the pressures used are generally very large and unrealistic for scalability. Therefore, it is of paramount importance that electrodes are developed in the future which can reduce the required external stack pressure. We postulated that the Sn electrode should retain high capacity and reversibility even with reduced pressures due to the networked electrode microstructure, the absence of conductive additive, and the inclusion of elastic solid electrolyte particles.

To test this theory, the Sn electrode was subjected to three different pressures and examined over the course of the first 10 cycles at a rate of C/20 (Figure 2.2b demonstrates that the electrode tends to stabilize after the first 10 cycles). Figure 2.3 presents the results of this study using

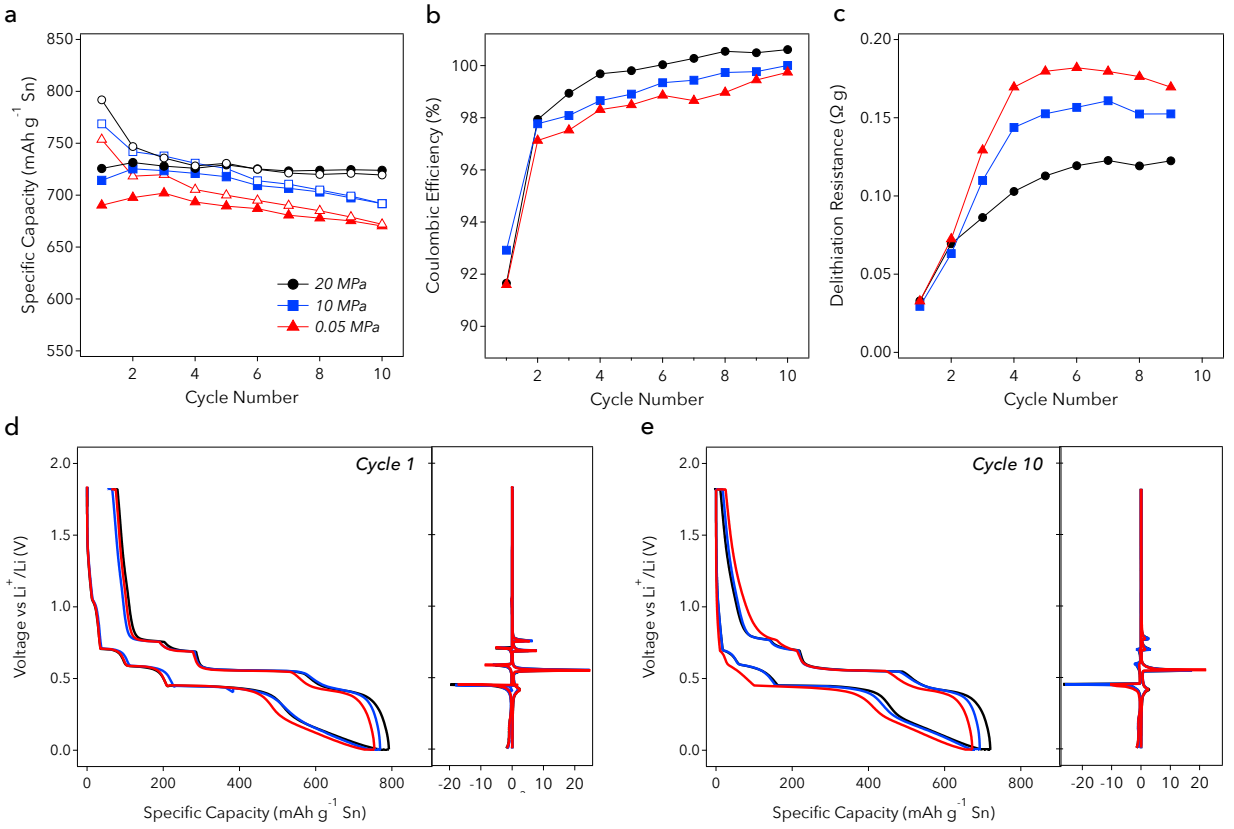

Figure 2.3: (a) Specific capacity with respect to Sn for applied constant external pressures of 20 MPa (black), 10 MPa (blue), and 0.05 MPa (red), (b) Associated coulombic efficiencies with all reaching greater than 99.7% by the 10th cycle, (c) Change in delithiation resistance per cycle, normalized per gram of Sn, (d) 1st cycle voltage profile with dQ/dV spectrum, and (e) 10th cycle voltage profile with dQ/dV spectrum.

external pressures of 20 MPa (standard operation), 10 MPa, and 0.05 MPa which is essentially the required pressure for the current collectors to maintain good electrical contact with the electrode (no lithiation hold is used which accounts for the reduced capacities). A general trend is seen that the initial lithiation and delithiation capacities decrease with decreasing pressure (Figure 2.3a). However, despite this characteristic, the first cycle CEs are essentially all the same for the three different pressures (Figure 2.3b). This would suggest that the pressures would simply be providing better active material utilization and not ensuring recovery of the original structure. This is further compounded by Figure 2.3d which demonstrates the first cycle voltage profiles at the three pressures. No discernible overpotentials are developed between the samples, however, lithiation Regions 3-5 tend to shorten. We suspect that with less confinement (ie. reduced pressure)

more particle-particle connections are lost due to expansion of Sn. Thus there is a smaller amount of active material utilization at the highest lithiated phases of Sn with less pressure.

Another clear difference between the samples is the rate at which they achieve stability. With decreasing pressure it takes longer for the cell to achieve a stable CE, however, all samples reach close to 100 by the 10th cycle. A possible explanation for this can be determined through examining the resistance increase over the course of cycling as in Figure 2.3c. Resistance rise was calculated by taking the resistance difference between full delithiation and the uncycled electrode and multiplying by active material mass. This should negate any inherent contributions from the resistance of the electrolyte separator. The three pressures all achieve stability but resistance increases with decreasing pressure. This would indicate a loss of some electrical contact (Sn network) and ionic contact (SSE network) in the electrode thus supporting the claim of less active material utilization.

By the 10th cycle, the 0.05 MPa condition loses the characteristic Region 1 and 2 plateaus (Figure 2.3e). This is most likely attributed to the volume increase factors (VIF) presented in Table 2.1. It can be seen that the cumulative VIF rise through Region 2 is 1.53. This would indicate that the Sn particles undergo a 53% increase in volume with the complete formation of LiSn. This is a rather miniscule amount compared to the ensuing expansion in Region 3. With the absence of an overpotential in Region 1 and 2 in the 10th cycle, this would indicate that some Sn becomes electrically isolated in the ambient pressure sample. Although, the Sn becomes reconnected once other particles expand enough to regain electrical contact. This behavior is interesting as it coincides with previous studies of monitoring in-situ pressure development over the course of Sn lithiation.[180] Mukaibo et al. found no detectable tensile stress development until after the LiSn phase is formed and postulated a "stress accumulation" occurring in Region 1 and 2 leading to rapid volume change in Region 3. Once sufficient expansion has occurred in a number of the Sn particles, other Sn is reconnected and can undergo lithiation, rationalizing the very little change in the voltage profile of the ambient condition in Regions 3 to 5.

In analyzing the effect of pressure on lithiation processes of Sn in solid-state, we can see that this is mechanistically different than previous studies by Molina Piper et al. of applying higher

pressures to simulate the confinement of silicon. The lower pressures used in this present study, allows us to study the preservation of electric and ionic pathways through particle contact rather than application of a strain energy.

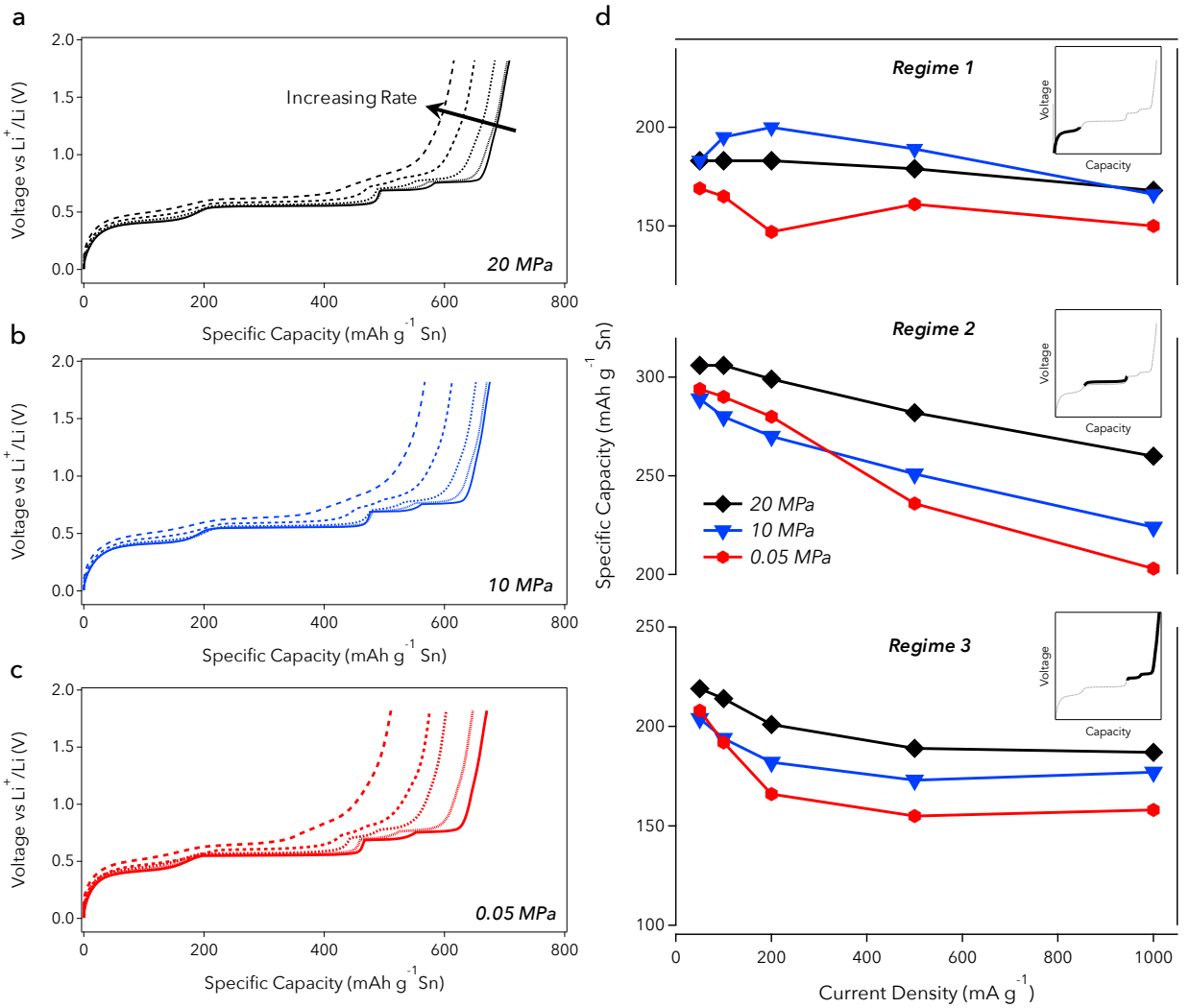

Figure 2.4: Asymmetric rate study of the Sn:SSE composite electrode with a constant lithiation rate of 50 mA g^{-1} and increasing delithiation rate up to 1000 mA g^{-1}. (a) Delithiation voltage profiles for cell with external pressure of 20 MPa, (b) Delithiation voltage profiles for cell with external pressure of 10 MPa, (c) Delithiation voltage profiles for cell with external pressure of 0.05 MPa, (d) Capacity contributions of three distinct regimes of voltage profiles with increasing rate. Insets are provided to demonstrate regime inclusions.

In addition to examining the effect of pressure on formation cycles in the networked Sn electrode, it is also desirable to inspect the dual effect of pressure and rate on Sn kinetics. The networked Sn electrode was subjected to an asymmetric rate study with increasing delithiation

rates and a constant C/20 lithiation rate. The delithiation voltage profiles were then split up into three distinct regimes: the first encompassing the reactions of Regions 4 and 5, the second covering Region 3, and the third comprising Regions 1 and 2. Figure 2.4a, 2.4b, 2.4c are the voltage profiles for the three different pressures at rates ranging from 50 mA g^{-1}(C/20) to 1000 mA g^{-1} (1C). Figure 2.4d plots the measured capacity contributions of the three delithiation regimes of the three pressures versus current density (insets highlight the regimes). Note: there will be some additional error introduced in estimating capacity contributions at higher rates due to overpotential, however, designated Regimes can still be discerned since the voltage profile shape remains relatively intact.

Regime 1: Pressure and rate have the smallest impact on Regime 1. A constant difference in capacity of 20 mAh g^{-1} exists between the 20 MPa and 0.05 MPa samples for all currents. In all three samples, the capacity retention of Regime 1 is greater than 90% when normalizing to the C/20 rate. This can again be analyzed by looking at the VIF values. The cumulative change in VIF in Regime 1 is 0.74. Most likely the actual value is less than this amount as this assumes the full formation of $Li_{17}Sn_4$. It has also been noted previously that electrochemical formation of Li_xSn compounds in the range of $2.6 < x < 4.4$ are highly disordered;[181] this would lead to a smaller volume change than simulating the equilibrium phases. With a small volume change in Regime 1, this could ensure full utilization of active material and explain the high capacity retentions even with high rates. Stress development from the expanded Sn would simulate applying an external pressure which could explain the constant difference between the 20 MPa and 0.05 MPa samples. In another trend, the highest lithiated phases exhibit a decline in lithium diffusion coefficient and electrical conductivity, resulting in an increased overpotential with increased rate in Regime 1.[175] Therefore, a disconnect exists between capacity retention and overpotential with rate.

Regime 2: Largely dominated by the transformation of Li_7Sn_3 to LiSn, Regime 2 exhibits the largest correlation amongst performance, pressure, and rate. It is clear that with decreasing pressure, the capacity drops significantly more with increasing rate. At 20 MPa, the cell retains 84% capacity at high rates whereas the 0.05 MPa cell retains 69% capacity. The VIF difference is 1.28, almost double Regime 1 and more than double Regime 3. Therefore, it is reasonable

that the delithiation contribution declines with high rates. Dissimilarly, with the highest lithium mobility in this Regime, the overpotential associated with increased rate remains small. As Regime 2 demonstrates the greatest capacity loss yet smallest overpotential with rate, this further supports the claim of disconnect between the two.

Regime 3: This area exhibits very interesting characteristics, most notably that a limiting current is reached at about 200 mA g^{-1}, above which capacity contribution does not change significantly. This appears to be characteristic of Sn itself as all three pressures had very similar profiles. In analyzing the voltage profiles of Figure 2.4, all three pressures lost the distinct dual plateaus of Region 1 and 2 to blend together to form a single plateau most likely due to the lowest lithium ion mobility in this Regime. This Regimes small VIF change (0.53) and previous studies showing small stress development[180] coincide with our observation of sustained capacity even at high rates. It is interesting to note that the retention in this Regime is independent of the behavior in Regime 2.

From examining the co-dependence of pressure and current on delithation mechanics, we can conclude that the most impacted factor is active material utilization. This is in direct correlation with volume increases in Sn as this serves to preserve electronic pathways. Therefore we see the highest impact of pressure and rate when Sn undergoes the largest volume changes. In the highest lithiated phases of the Li-Sn alloy, the large volume increases and stress development act to form an internal pressure within the electrode which negates the requirement for an external pressure. This is made possible by the inclusion of rigid solid electrolyte particles for Sn to expand into which separates the vast performance differences between solid and liquid cells containing Sn. Future work will focus on in-situ monitoring of Sn expansion in solid-state and try to determine the overall electrode level volume changes.

2.3 Conclusion

We have demonstrated the electrochemical performance of a high capacity Sn anode in an all-solid-state Li-ion cell. By taking advantage of the favorable inherent ductility and mixed conductivity of the active material, we formed an interpenetrating network of Sn and solid electrolyte.

This ideally structured composite electrode delivers remarkable capacity of over 800 mAh g^{-1} with respect to Sn and coulombic efficiency of 99.2%, while exhibiting a reversible Sn-Li alloying process. To our knowledge, this is the first report on utilizing high amounts of pure-Sn metal (70 wt. % of the total electrode) in an all-solid-state Li-ion battery without any conductive additives; this allows for a volumetric capacity of 844 Ah L^{-1} which competes with even some of the highest silicon-based systems. We investigated the effect of pressure and rate upon the delithiation mechanics of the favorable microstructure; correlations are drawn that volume increase factors and stress accumulation are the largest contributors to material utilization over the course of Sn-Li phase transformations. We even show that Sn develops a pseudo-pressure through expansion negating requirements for external pressure and allowing ambient operation the next step towards commercialization of the solid-state battery. We believe that this initial work provides new opportunities to study the electrochemical expansion of Sn with the inclusion of rigid particles.

Chapter 3

High-Capacity and Highly Reversible Silicon-Tin Hybrid Anode

3.1 Introduction

Batteries based upon ceramic electrolytes have become an attractive conception for elevated temperature and safe operation.[18] Approaches to using next-generation battery materials in the solid-state have to be reconsidered as a new set of engineering challenges arise; hindrances such as solid electrolyte interphases (SEI) are replaced with solid-solid material interfacing.[168] To enable the use of most energy-dense materials in the solid-state, new tactics must be taken that deviate from the standard.

Silicon (Si) is the most sought after anode alloying material due to its high theoretical capacity and natural abundance. However, the drawbacks (massive expansion, mechanical pulverization, active material isolation) have also been well documented and studied extensively in the solid-state.[182,183] Molina Piper et al. studied the effect of confinement pressure on silicon: it was concluded that with greater confinement pressure, silicon alloys with fewer moles of lithium than free energy allows, conversely, is able to cycle for much longer periods of time.[167] Son et al. and subsequently Yersak et al. applied this concept to confining silicon in a silicon-titanium-nickel (STN) matrix to limit the extent of lithiation while improving reversibility.[171,182] STN is a rather weak mixed conductor with small electrochemical activity and improvements can be made to this concept.

We recently reported on an in situ derived tin (Sn) networked anode.[173] As Sn is ductile

and an excellent mixed conductor, long-range interfaces were developed between Sn and solid electrolyte lowering interfacial resistance. The high electrical conductivity absolved the need for carbon additives and therefore prevented active material isolation. Sn additionally does not exhibit any decomposition with the sulfide solid electrolyte (SSE) which allows for superior stability. Sn therefore appears to be a perfect active and mixed conductive matrix to host Si. Only one other study has been identified using this pairing,[184] however, this was performed in a thin-film format whereas we envision the Sn-Si system as a bulk anode exhibiting commercial grade capacities. For the reasons outlined above, this system does not lend itself to the non-aqueous, solvent based lithium ion system rather is better suited for a ceramic-based system.

In this study, we present a proof-of-concept pairing the highest capacity anode material, Si, within a Sn matrix. As Sn lithiates at greater voltages than Si, the pressure derived by Sns lithiation expansion is used to confine silicon achieving greater reversibility. Thus a solid-state battery is presented with tremendous stability over 50 cycles. Through an extensive electrochemical analysis and x-ray diffraction (XRD), we confirm full utilization of Sn and determine the extent of Si utilization. By replacing some of the more expensive Sn with Si, we present a more commercially viable anode with greater volumetric and gravimetric capacities than previous reports.

3.2 Results and Discussion

Work in this section has been presented in the 2016 publication.[185] Figure 3.1a shows the excellent reversibility of the Sn-Si system over 50 cycles. The cell achieves an active material specific capacity of over 1000 mAh g^{-1}. This is in comparison to the 800 mAh g^{-1} previously achieved with using pure Sn as the anode.[173] The extra capacity clearly comes from the utilization of Si as is confirmed in the voltage profile in Figure 3.1b. The Si contribution is most evident on the first cycle lithiation and contributes consistently to the remaining cycles. An ideal anode should have as low of a voltage versus lithium as possible. Using pure Sn, we previously achieved a stable cycling anode with an average delithiation voltage of 0.79 V (vs. Li^+/Li), however, the addition of the silicon lowers the voltage to 0.53 V (vs. Li^+/Li) which is even more desirable. A coulombic

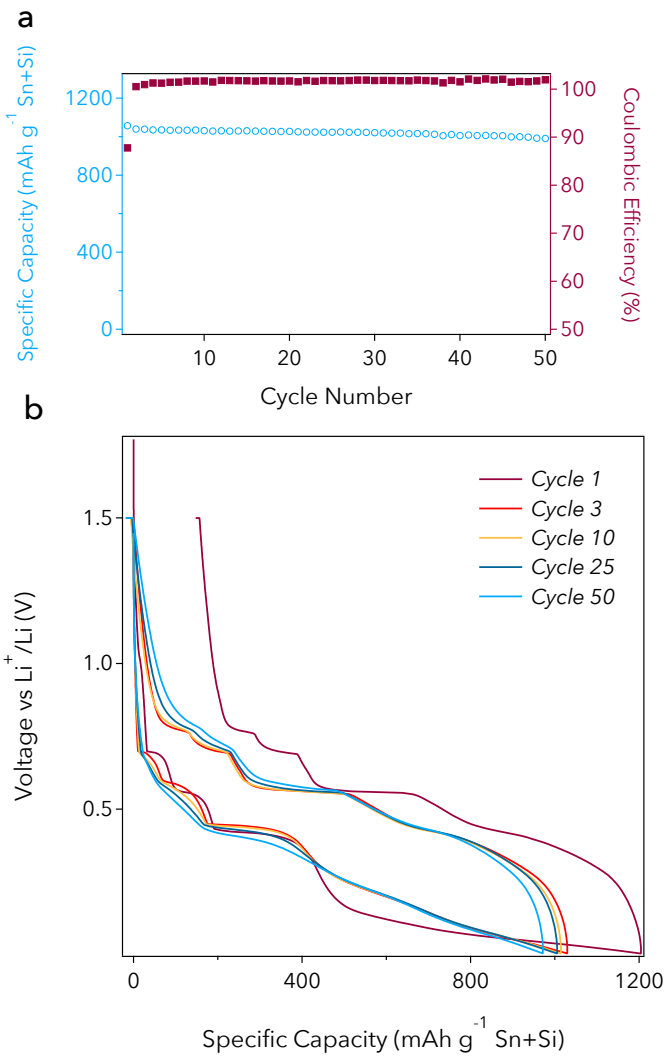

Figure 3.1: (a) Cycle performance and coulombic efficiency of Sn:Si:SSE [7(3:1):3] anode in all-solid-state Li-ion battery at 60°C with C/20-rate (80 mA g^{-1}) and (b) Corresponding voltage profiles of the Sn:Si:SSE anode vs. LiIn counter electrode (converted to vs. Li^+/Li).

efficiency greater than 100% is evident over the course of cycling. This is attributed to the voltage hold applied at full delithiation and is apparent in Figure 3.1b.

Deconvolution of the system to attribute individual capacities to the different materials can prove tough. Si has a varying voltage profile between the first and subsequent cycles and Sn has five distinct voltage regions. Therefore, cycles 1 and 3 are deconvoluted separately. Distinctive lithiation voltage regions have been assigned using the designation of cycle-material-region (ie. 1-Si-1 or 3-Sn-4). Figure 3.2a and 3.2b are the first and third cycle voltage profiles, respectively, of a Si cell in

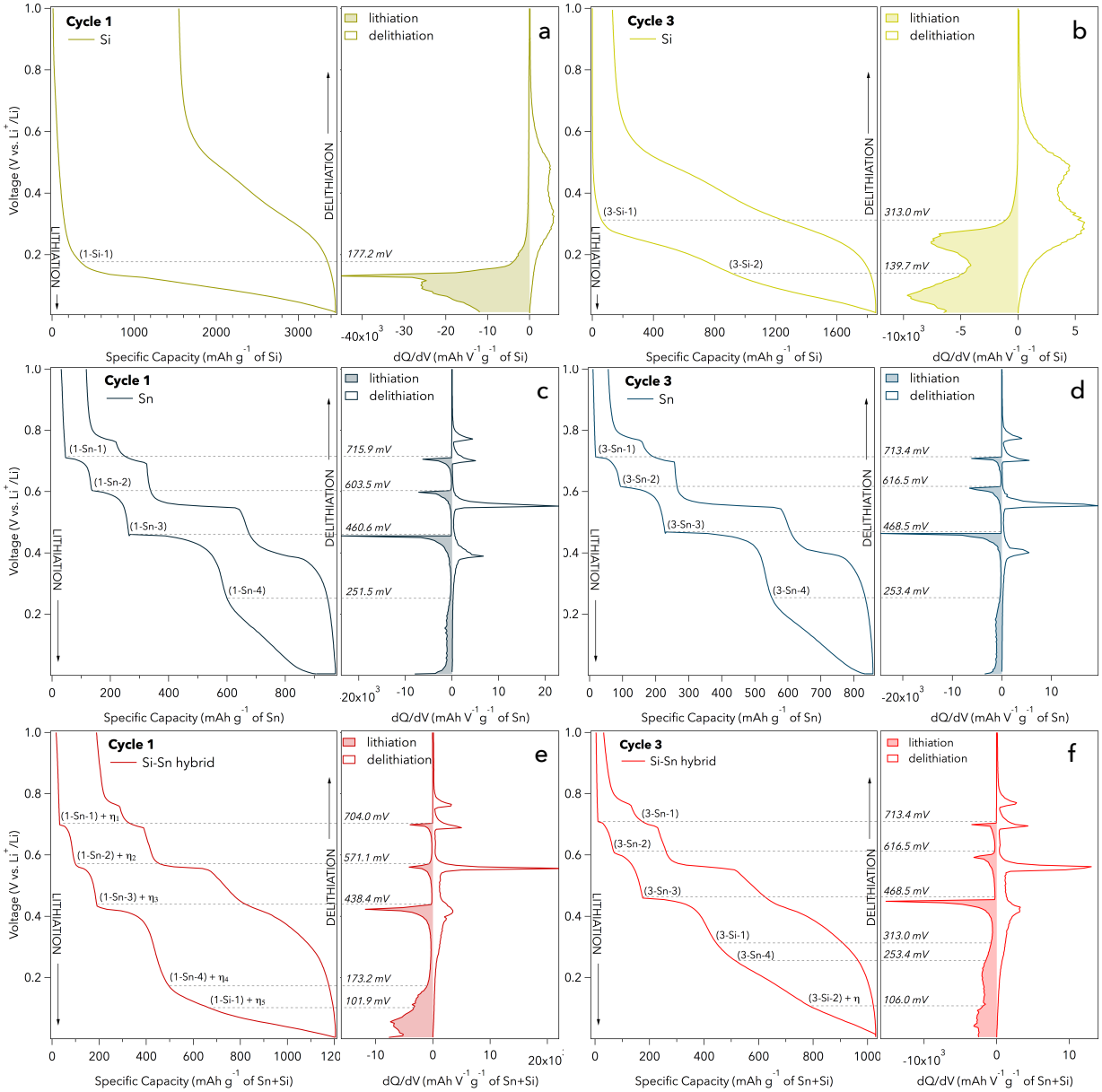

Figure 3.2: Si anode in solid-state voltage profiles and corresponding dQ/dV spectrum for the first cycle (a), and third cycle (b). Sn anode in solid-state voltage profiles and corresponding dQ/dV spectrum for the first cycle (c), and third cycle (d). Sn:Si hybrid anode in solid-state voltage profiles and corresponding dQ/dV spectrum for the first cycle (e), and third cycle (f). Distinct lithiation regions are assigned for (a) through (d) and overlapped onto (e) and (f). Overpotentials η_1 through η_5 present a hindrance to the volumetric expansion in Sn (e) but disappear once Si has fully amorphized (f).

solid-state.[167] These cells used small mass loadings of Si to achieve good stability thus it is assumed that full utilization of Si occurred. The system clearly represents the Si characteristic: the first cycle

contains a single region (1-Si-1) which reflects Sis initial two-phase lithiation where the crystalline Si is consumed to form lithiated amorphous (Li_xSi), the third cycle contains two unique regions (3-Si-1, 3-Si-2) which correspond to amorphous Li_xSi-alloys (the structural changes responsible for these peaks are not clearly understood yet, but thought to be a result of short-range ordering in the amorphous Li_xSi).[186] Figure 3.2c and 3.2d are the first and third cycle voltage profiles, respectively, of a Sn cell in solid-state.[173] Sn retains a relatively well-ordered voltage profile from the first to the third cycle. The four distinct regions (1-Sn-1 to 1-Sn-4) represent changes through 7 distinct crystallographic phases culminating in the highest lithiated phase, $Li_{17}Sn_4$.[178] Lastly Figure 3.2e and 3.2f are the first and third cycle voltage profiles, respectively, of the Sn-Si hybrid cell under study. The Si and Sn voltage regions have been overlaid onto the profile as well as the differential capacity plotted alongside for convenience. All cells run in Figure 3.2 use a similar current density per unit mass (approximately 100 mA g^{-1} active) and temperature of operation (60°C) therefore, they are all comparable. Interestingly, the Sn regions exhibit an overpotential on the first cycle (depicted as η_1, η_2, η_3, η_4 in Figure 3.2e) compared to the pure Sn cell. This is most likely due to the addition of Si preventing free initial expansion. By the third cycle, however, the Sn regions in the Sn-Si cell overlap exactly with the pure Sn. The contribution of the Si is clear in the hybrid cell not just by the increased capacity of the system but its unique print in the voltage profile. Similar to the Sn, Si exhibits a small overpotential (η_5) of about 75.3 mV. This will be explained in the upcoming section. By the third cycle this overpotential nearly disappears except for the lower lithiation voltage which maintains a constant overpotential (η) throughout the cycling of the cell enabling a remarkably reversible Si material. This is the result of a constant external pressure on Si imposed by the active and expanding Sn during its lithiation.[167]

In order to fully determine the extent at which Si is utilized, we examine how much Sn is lithiated. Figure 3.3 shows the XRD pattern of a hybrid cell which has been discharged to 5 mV [galvanostatic equivalent to the parameters in Figures 3.1 and 3.2 (C/20 rate)]. The distinct peaks at 22.1°, 23.5°, and 38.9° (2θ) are attributed to $Li_{17}Sn_{44}$. Smaller peaks at 32.5°, 37.4°, and 39.7° (2θ) also pertain to the fingerprint of such phase. Facile kinetics of solid state phase transformation

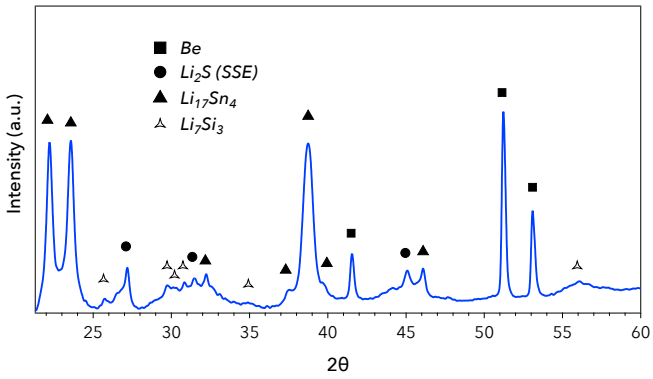

Figure 3.3: (a) Ex-situ XRD spectrum of Sn:Si:SSE anode discharged to 5 mV vs. Li. Sn fully lithiates to $Li_{17}Sn_4$ phase. In-situ derived pressure from Sn expansion allows Si to crystallize to the Li_7Si_3 phase rather than remaining in the amorphous analogue.

allow for this fully lithiated phase to be achieved at room temperature.[181] In our earlier work on the Sn system, we achieved theoretical capacity on the first lithiation.[173] We therefore assume the full lithiation and utilization of the Sn matrix in the hybrid composite anode. Backing out the theoretical capacity of Sn from the actual achieved capacity, we determine that Si alloys with approximately 2.3 mol of Li. Although in this range Si should typically be found in the a-Li_xSi alloy,[187] unspecified peaks in Figure 3.3 fit remarkably well with the Li_7Si_3 phase typically only present at high temperatures.[188] The solid-state amorphization of Si has been proposed many times to be caused by the high nucleation barrier caused by the high interfacial energy.[186,189] Indeed the activation energy for the thermodynamically stable crystalline Li_xSi phases is quite high.[190] Only one study has investigated the effect of compressive stress on silicon alloy dynamics[167] but did not investigate how this impacted nucleation kinetics. Since this hybrid system has Sn, which expands prior to Si lithiation (an expansion on the order of 200% by this stage[173]), an enormous pressure is exerted on Si. This manifests itself as a large strain energy or elastic energy in homogeneous nucleation theory.[191] Thus we propose volumetric barriers overtake interfacial barriers as the limiting factor in the formation of the Li_xSi alloy. In this case, the molar volume of Li_7Si_3 is less than that of the molar volume of a-Li_7Si_3 and therefore is preferential. The presence of an initial 75 mV overpotential (η_5) could indicate the additional driving force for silicon crystallization.

Unfortunately, this is not an ideal system to study this effect due to the heterogeneity of the electrode. Therefore, we propose to study further this effect by encapsulating Si with Sn to provide a system that can be modeled.

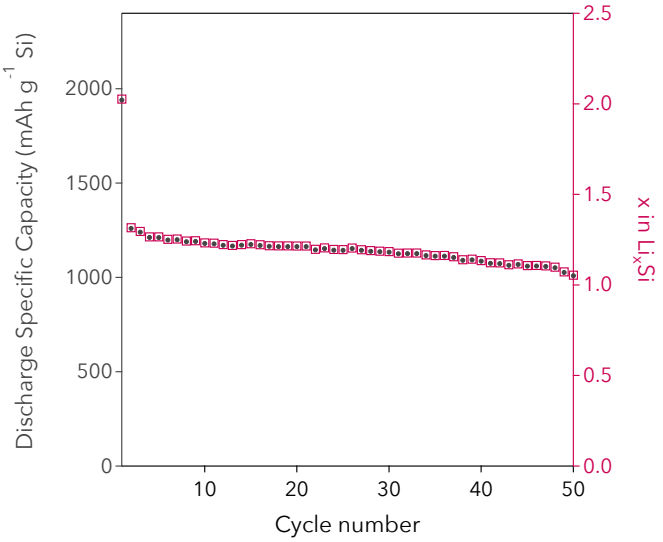

Figure 3.4: Moles of Li per Si or specific capacity of Si in the Sn:Si:SSE anode in Figure 3.1. The value is developed assuming Sn fully lithiates every cycle.

If we continue to make the assumption that Sn is fully lithiated throughout cycling, then we can back out the amount of silicon utilization throughout the course of the 50 cycles. Figure 3.4 presents the extent of Si lithiation. The excellent reversibility of moles of lithium inserted into Si is far greater than our previous report.[167] Previously, we found similar moles of lithium to alloy with Si but using small and external compressive stresses. However, poor stability was shown most likely as compression was applied uni-axially. The inherent stability in this new hybrid can therefore be attributed to the much more uniform application of stress to all sides of the silicon particles. As this appears to be the case, we propose further work to investigate even better methods of encapsulating Si in Sn such as sputtering.

3.3 Conclusion

This study presents a proof-of-concept idea of pairing high capacity anode materials, Sn and

Si together. By doing so, we present a cell with a reversible capacity of 700 mAh g^{-1} (normalized to electrode) for 50 cycles. This is a substantial increase from previous work which already demonstrated some of the best performance characteristics of any anode in solid-state to date. We confirm through electrochemical analysis and XRD that Sn is fully utilized and calculate the extent of Si utilization. With Sn lithiating prior to Si, we create an in situ pressure that acts conformally on Si. Therefore we achieve greater extent of lithiation and better reversibility than our previous studies using uni-axial pressure for reversible Si alloying. The idea of using Sn as a mixed conductive, electrochemically active matrix to imbed Si is a new concept. New architectures will be investigated further to get better encapsulation of Si such as sputtering.

Chapter 4

A Silicon-Based Superionic Conductor for Enhanced Lithium Metal Stability

4.1 Introduction

Advanced energy storage applications, such as electric vehicles and grid energy storage, require the next generation of batteries to exhibit high energy density, enhanced safety, and utilization of cost effective materials.[3,192] Commercial lithium-ion batteries employing organic liquid electrolytes suffer from flammability issues due to overheating and overcharging.[193,194] Replacement of the liquid electrolyte with a solid electrolyte resolves these concerns as well as enables the use of higher energy density materials.[122,126,195] The main issue regarding solid electrolytes has been low lithium ion conductivities with respect to liquid electrolytes.[18] Recently, the lithium ion superconductor $Li_{10}GeP_2S_{12}$ (LGPS) demonstrated conductivities on the order of liquid electrolytes.[72] An analog to LGPS was also reported, $Li_{10}SnP_2S_{12}$ (LSnPS), which sacrifices ionic conductivity but provides cheap replacement for the more expensive germanium.[196]

Classification of these solid electrolytes can be misleading the properties reported might differ from those exhibited during battery operation. First, the high lithium ion conductivities for these electrolytes were reported following sintering ($> 500°C$) of the raw, crystalline electrolyte powder. Sintering may not be a possibility due to low decomposition temperatures or undesired reactions with active materials in electrodes.[168] Second, electrolyte chemical stability versus lithium is claimed by nature of cyclic voltammetry despite reports that metastable crystalline solid electrolytes spontaneously decompose in the lithium-reducing environment.[104,197,198] Therefore, to

empower the lithium metal battery, an electrolyte exhibiting high ionic conductivity in powder form with superior lithium stability is critical.

In this study, we have synthesized and characterized the third analog to LGPS, via mechanochemical milling, using the isovalent ion of silicon to displace germanium as a cost effective constituent. Silicon has long been studied as a basis for solid electrolytes such as the Li_4SiS_4 crystal,[199] $Li_2S - SiS_2$ system,[200,201] $Li_2S - SiS_2 - Li_xMO_y$ glasses,[202,203] and the $Li_{4-x}Si_{1-x}P_xS_4$ thio-LISICON derivative.[204] However, none of these solid electrolytes reached conductivities greater than 10^{-3} S cm^{-1} or demonstrated suitable stability versus lithium metal. The crystal $Li_{10}SiP_2S_{12}$ (LSiPS) displays a conductivity of 2.3 x 10^{-3} S cm^{-1} prior to sintering, which is greater than LGPS under the same conditions. Additionally, LSiPS demonstrates an excellent chemical stability versus lithium metal and compatibility with high voltage cathode materials; these advantageous properties manifest in superior cycling stability of LSiPS over LGPS in a secondary lithium metal battery configuration. Performance, purity, and thermodynamic stability of LSiPS are correlated to the state of precursor amorphization prior to crystallization. The crystalline properties of LSiPS along with ionic conduction capabilities are in excellent agreement with the predictive modeling previously performed for this material.[198] After completion of our study, we became aware of an independent attempt by Kuhn et al. to synthesis the LSiPS crystal.[205] This study, however, could not achieve the desired stoichiometry as is presented in this study.

4.2 Results and Discussion

This work is reported in the 2014 publication.[100] Synchrotron x-ray diffraction (XRD) was used to probe the crystalline properties of LSiPS and in-house synthesized LGPS. Figure 4.1 depicts the measured XRD patterns for the crystallized LSiPS_20 and LGPS samples as well as corresponding computed Le Bail refinement profiles. Le Bail refinements confirmed the presence of the previously reported LGPS structure[72] and confirmed that LSiPS_20 is isostructural in the $P4_2/nmc$ space group (no. 137). Le Bail refinements provided the following cell parameters for LGPS: $a = 8.7082(2)$ Å, $c = 12.6286(3)$ Å; and for LSiPS_20: $a = 8.6512(5)$ Å, $c = 12.5095(8)$ Å.

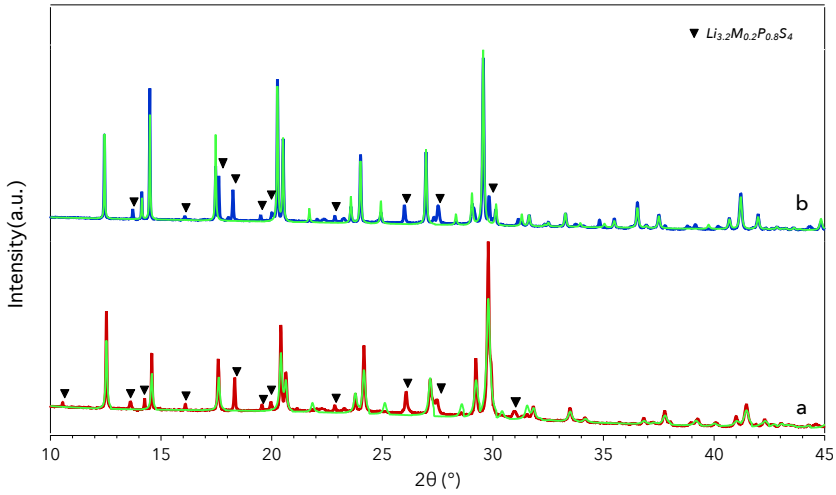

Figure 4.1: Synchrotron XRD patterns of: a) LSiPS_20 sample following crystallization, b) LGPS sample following crystallization. The obtained Le Bail refinement profiles are overlaid (green) for each sample. For the identified phases, M = Si or Ge in the corresponding samples.

The parameters computed for LGPS are both within 0.1% of the previous reports by Kamaya et al. and Kuhn et al. indicating a near identical structure was synthesized.[72,206] The LSiPS crystal showed a decrease in both lattice parameters from LGPS. While this doesnt fully fit the trend for the a parameter, it does for the c parameter as shown by predictive modeling and between the other analogs to LSiPS.[72,196,198]

For both samples, secondary phases were detected which precluded the use of Rietveld refinement. Upon further examination, no unanticipated peaks are present in the initial milled samples (not shown) indicating that most likely no impurities were introduced during the initial amorphization process. Comparison with previous reports has shown that the secondary phase is most likely attributed to the thio-LISICON $Li_{4-x}Si_{1-x}P_xS_4$[204] and $Li_{4-x}Ge_{1-x}P_xS_4$[69] superconducting analog in LSiPS and LGPS, respectively. The shared thio-LISICON peaks between LSiPS_20 and LGPS samples are as follows: 16.1°, 17.6°, 18.3°, 19.5°, 20.0°, 22.9°, 26.0°, 27.5° (2θ). The aforementioned peaks are all within 0.05 2θ between the two samples and are highlighted in Figure 4.1a and 4.1b. These peaks provide good agreement with the previously reported XRD patterns for $Li_{3.2}Si_{0.2}P_{0.8}S_4$ and $Li_{3.2}Ge_{0.2}P_{0.8}S_4$.[69,204] As both of these structures are very close in formula to

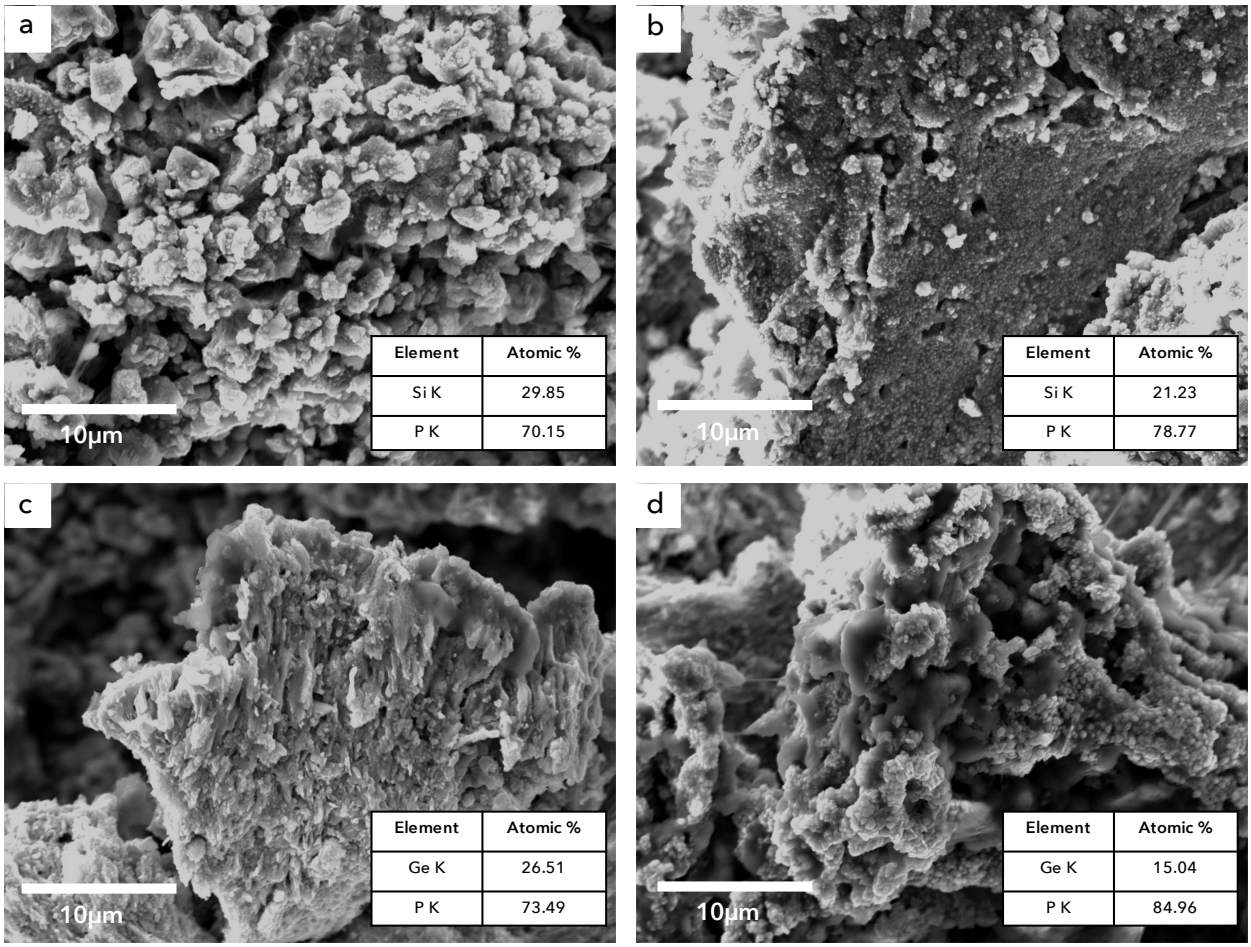

Figure 4.2: SEM-EDS images with atomic percentages of Si-K and P-K displayed in the table insets: a) LSiPS_20 sample phase 1, b) LSiPS_20 sample phase 2, c) LGPS sample phase 1, d) LGPS sample phase 2. The analysis confirms the presence of two phases: phase 1 being the tetragonal $Li_{10}MP_2S_{12}$ superionic conductor in (a) and (c), phase 2 being the monoclinic $Li_{3.2}M_{0.2}P_{0.8}S_4$ thio-LISICON in (b) and (d).

$Li_{10}MP_2S_{12}$, it is reasonable to assume thio-LISICON is the secondary phase. Scanning electron microscopy-energy dispersive spectroscopy (SEM-EDS) analysis was performed to further illustrate the presence of two phases; results for the LSiPS_20 and LGPS samples are displayed in Figure 4.2. Specifically, radiation from Si-K and P-K were compared as this ratio differentiates the respective phases. Results confirm the presence of two phases: one with a silicon (or germanium) to phosphorus ratio of 1:2 indicative of the tetragonal $Li_{10}SiP_2S_{12}$ crystal (Figure 4.2a and 4.2c) and one with a silicon (or germanium) to phosphorus ratio of 1:4 indicative of the monoclinic thio-LISICON $Li_{3.2}M_{0.2}P_{0.8}S_4$ (M = Si,Ge) crystal (Figure 4.2b and 4.2d). Both measurements are within exper-

imental error for the determined compositions; additional error is most likely introduced as both samples were briefly exposed to air during sample preparation.

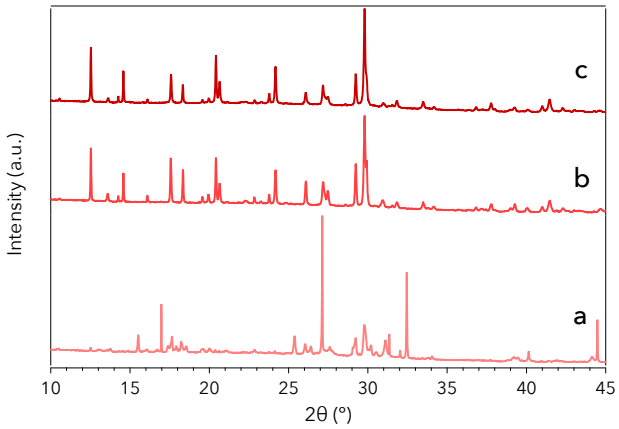

Figure 4.3: Synchrotron XRD patterns of: a) LSiPS_0 following crystallization, b) LSiPS_1 sample following crystallization, c) LSiPS_20 sample following crystallization. From the XRD patterns it is apparent that only LSiPS_20 and LSiPS_1 achieved the desired crystalline structure.

Figure 4.3 displays XRD patterns for LSiPS_0, LSiPS_1, and LSiPS_20. LSiPS_0 did not achieve the desired structure and is most likely an intermediary phase of $Li_{4-x}Si_{1-x}P_xS_4$. LSiPS_1 shows evidence of a $P4_2/nmc$ crystal with lattice parameters of $a = 8.6483(4)$ Å and $c = 12.5073$ Å. However, a higher percentage of the thio-LISICON secondary phase is present as compared with the LSiPS_20 sample. For LSiPS_20 and LGPS, it was computed that about 15% secondary phase is present; therefore, these samples are comparable. Most likely, the thio-LISICON acts as a hinderance to performance as the pure tetragonal superionic conductor is the higher conducting phase. It appears that the LGPS and LSiPS structure is very sensitive to the heat treatment environment and temperature as other attempts have also shown variation in structure purity with varying preparation conditions.[207] Further work will be performed to optimize the structure.

Figure 4.4 shows the Arrhenius relationship in ionic conductivity of the three LSiPS and LGPS crystalline samples. Conductivity values are calculated by taking the sum of the grain boundary and grain resistance values observed in impedance plots. The frequency range used is not capable of discerning the separate contributions in the samples. Activation energies are calculated directly from the slope of these plots over the temperature range; these values are presented in the table

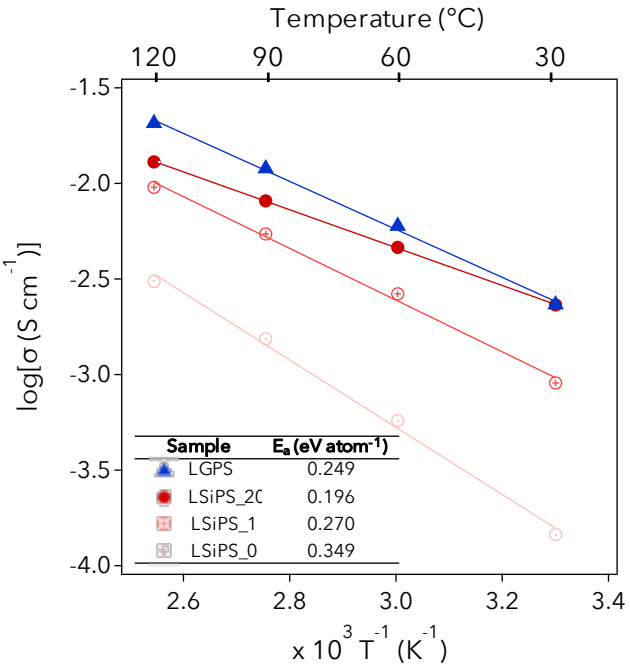

Figure 4.4: Temperature dependence for the ionic conductivity measurements of LSiPS_0, LSiPS_1, LSiPS_20, and LGPS. Activation energies were calculated from the slopes of the plots and displayed in the legend. As a general trend, with increased initial ball-milling, the conductivity increased and activation energy decreased.

inset. LSiPS_20 exhibits a room temperature conductivity of 2.3 x 10^{-3} S cm^{-1} which is greater than the LGPS sample with a conductivity of 2.1 x 10^{-3} S cm^{-1} prepared in the same conditions. To the best of our knowledge, this is the highest conductivity reported for an unsintered silicon-based solid electrolyte. It should also be noted that all these conductivity values are representative of the material prior to sintering: the crystalline powder was simply cold-pressed prior to AC impedance measurements. As mentioned previously, this is a better representation of the actual material parameters that are exhibited during battery operation. This also allows comparison with other electrolytes which typically are not sintered prior to determination of ionic conductivity values.

It is apparent that the conductivity of LSiPS drastically increases with a longer initial ball-mill time and thusly, a greater state of amorphization as presented by the XRD patterns. Additionally, the activation energy decreases with longer milling times. LSiPS_20 sample demonstrates an activation energy of 0.196 eV $atom^{-1}$. This is in excellent agreement with the first principles pre-

diction of LSiPS.[208] The activation energy for LGPS is 0.249 eV atom^{-1}, agreeing with previous experimental studies[72] and predictive modeling[198] an indication that a similar structured sample was synthesized.

Previous reports have demonstrated the enhanced conductivity of crystals precipitated from the glassy phase rather than by a solid-state reaction for the $Li_2S - P_2S_5$ system.[70] This is attributed to a greater dispersion of elements allowing for a smaller diffusion distances for reactions. This helps explain the incremental increase in conductivity of LSiPS simply by creating a more amorphous precursor to crystallization. Expectedly, as the LSiPS_20 sample exhibits a greater crystallinity, and larger channel size due to the increased lattice parameters than the LSiPS_1 sample, the conductivity is greater and activation energy is smaller.

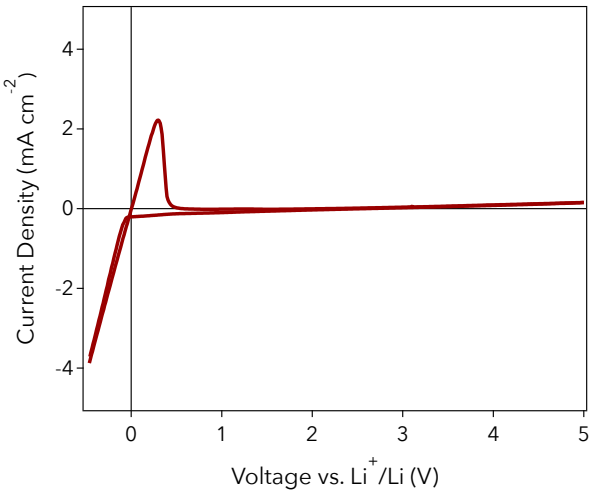

Figure 4.5: Cyclic voltammetry sweep of LSiPS_20 against lithium and titanium electrodes. Lithium plating and stripping peaks are identifiable around 0 V. While this test confirms the electrochemical stability of LSiPS from 0 to 5 V, it provides no indication of the interaction at the electrolyte-lithium interface.

Many studies utilize a cyclic voltammetry (CV) sweep of a solid electrolyte against a lithium counter to determine the stability window against lithium metal.[72,197,200,201] While this is an indication of electrolyte decomposition at higher voltages (electrochemical stability), it neglects spontaneous decomposition (chemical stability) that is often undetectable in this configuration. Figure 4.5 is a CV of LSiPS_20 confirming electrochemical stability from 0 - 5 V. Although LSiPS

is electrochemically stable in this voltage window, it can be seen this gives no indication of chemical stability at the electrolyte-lithium interface. Metastable crystalline solid electrolytes are theorized to decompose to either more stable crystalline phases or amorphous layers at the lithium interface. These layers often have much lower conductivities than the unreacted electrolyte, therefore, it is favorable to minimize the magnitude and effect of decomposition.

LSiPS and LGPS were "stored" against lithium, periodically measuring the decomposition growth by virtue of AC Impedance Spectroscopy (Figure 4.6). A time dependent increase in resistance can be directly attributed to the growth of the decomposition layer as the bulk and grain boundary conductivity values of the electrolyte remain unchanged (concurrently making the assumption that the thickness of the decomposition layer is much smaller than the thickness of the entire electrolyte layer). Figure 4.6a is a schematic of the electrolyte-lithium storage cell. A symmetric lithium-lithium cell is used and therefore, similar reactions occur on both interfaces. The electrolyte decomposition layer, henceforth called the passivation layer, forms at the electrolyte-lithium interface. We assume an infinite reservoir of lithium and therefore can assume the passivation layer grows into the bulk electrolyte layer.

Figure 4.6b is a representation of the Voigt equivalent circuit for the symmetrical cells. The main components include R_B (bulk electrolyte), $R_P(t)||CPE_P(t)$ (passivation layer), $R_{CT}(t)||CPE_{DL}(t)$ (charge transfer), Z_{DIFF} (Warburg diffusion impedance). Normally used capacitors for this setup are replaced with constant phase elements due to the inhomogeneity of the cell, ie. porosity, non-uniform interfaces, etc. This equivalent circuit model is similar to previous models of solid-electrolyte-interphase formations in liquid cells.[209] R_B, the bulk resistance, is a sum of the grain boundary and grain conductivities, determined during the first scan at 0 hours (insets shown in Figure 4.6c and 4.6e). The passivation layer is most likely a mixed conducting interface (MCI),[210] therefore, R_P would include contributions from the ionic and electronic conductivities of the MCI. Due to the frequency resolution limitations, the exact contributions from ionic and electronic cannot be separated; however, the sum of the two can be represented by the single element. R_{CT}, charge transfer resistance, is a measure of the resistance for the reaction of $Li^+ + e^- \rightarrow Li$ at

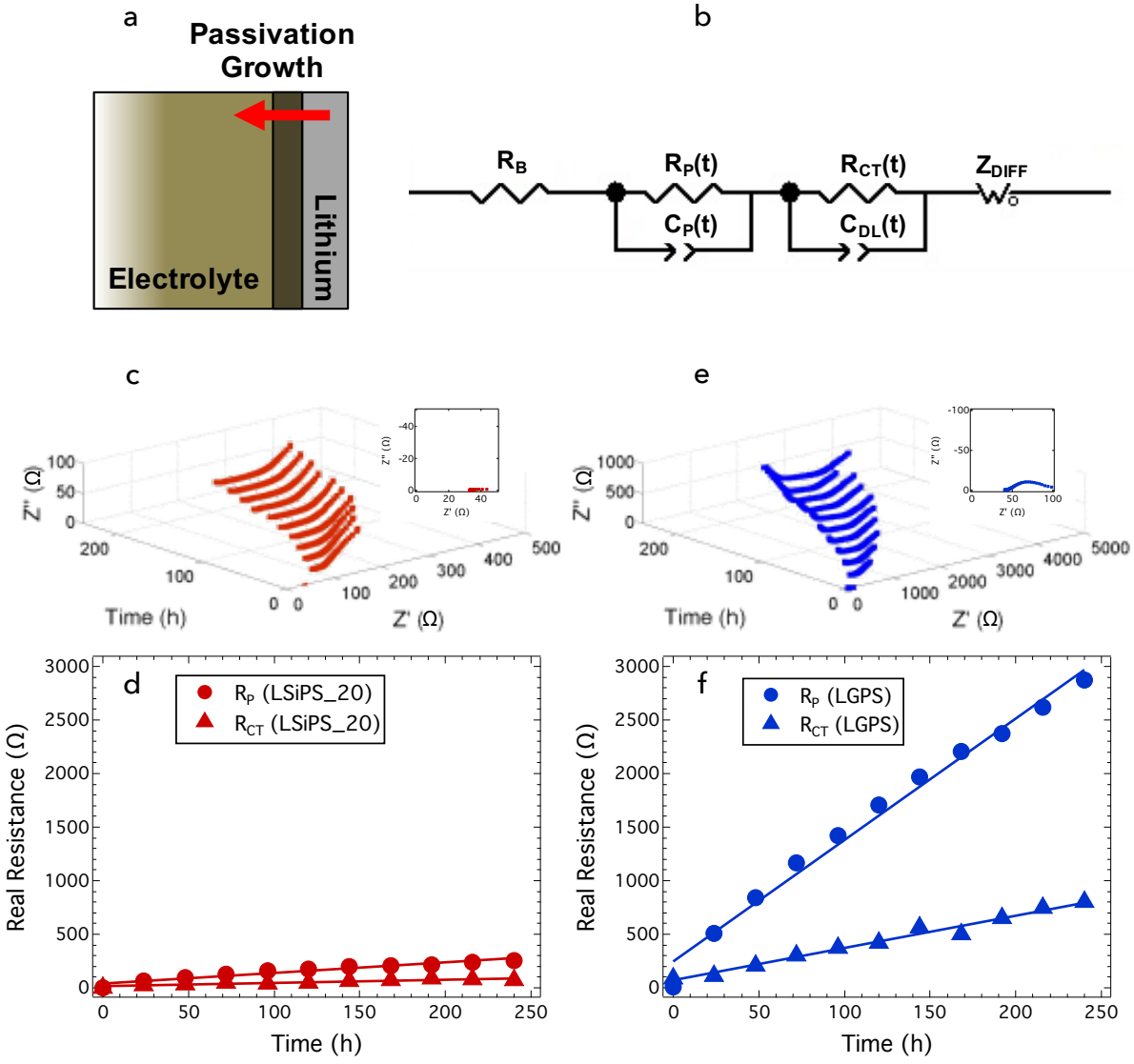

Figure 4.6: a) Schematic of passivation layer development at electrolyte-lithium interface with growth direction into the bulk electrolyte region, b) The Voigt-type equivalent circuit representation of the lithium-lithium symmetric cells, c) Nyquist Plot of LSiPS_20 over a 10-day period. The inset enlarges the scan at 0 hours, d) Plotted values for the transient resistive elements representing the passivation layer development in LSiPS_20, e) Nyquist Plot of LGPS over a 10-day period. The inset enlarges the scan at 0 hours, f) Plotted values for the transient resistive elements representing the passivation layer development in LGPS. Overall, the time-dependent circuit values for LGPS are approximately 10 times as resistive as LSiPS_20.

the interface between the electrolyte and passivation layers. The values of R_P and R_{CT} are both functions of time as the decomposition of the electrolyte is considered continuous. These transient circuit elements are determined by fitting the equivalent circuit to each data set and taking the

corresponding real impedance values on the Nyquist plots. Figure4.6c and 4.6e demonstrates the Nyquist plot of LSiPS_20 and LGPS, respectively, in the symmetric setup occurring over a 10 day period. Both LSiPS and LGPS suffer from decomposition at contact sites between lithium and electrolyte, however, the layer formed by LSiPS is either more ionically conductive or of a smaller thickness due to the drastically reduced electronic resistance. Recent reports have claimed that the layer formed by the decomposition products is a mixed conductor.[210] This stability data is corroborated by results of computer modeling by Ong et al. demonstrating that the LSiPS system has a lower decomposition energy than LGPS, indicating greater stability (in this case lower energy means a more thermodynamically stable system).[198] LSiPS also seems to be more stable than other metastable crystals reported when comparing resistance growths with time.[197]

R_P and R_{CT} are plotted for LSiPS_20 and LGPS in Figure 4.6e and 4.6f, respectively. The passivation layer resistance and charge transfer resistance both exhibit nearly linear behavior after 24 hours of storing, indicating a steady-state uniaxial growth in the passivation layer. The passivation layer resistance for LGPS grows approximately six times as much as LSiPS; similarly the charge transfer resistance grows five times as much. Overall, the time-dependent circuit values for LGPS are approximately 10 times as resistive as LSiPS. Interestingly, the ratio of passivation to charge transfer resistance in both samples is about 3 to 1. This could indicate that similar degradation mechanisms occur in both crystals. We propose that the passivation layer for LSiPS grows slower than LGPS not only because of the greater stability versus lithium but the more electronically insulating nature of the passivation layer. The decomposition byproducts as proposed by Ong et al. includes the $Li_{15}M_4$ (M = Si, Ge) alloy[198] - the silicon derivative having lower electronic conductivity and lithium diffusivity than germanium. The properties of the passivation layer as well as the mechanism for decomposition will be the subject of a later study.

Figure 4.7 shows the stability for all three LSiPS samples. It is apparent that LSiPS_1 is not as stable as LSiPS_20. As LSiPS_1 contains a greater percentage of thio-LISICON, this can be a direct indication that the $Li_{3.2}Si_{0.2}P_{0.8}S_4$ phase is not as stable as the $Li_{10}SiP_2S_{12}$ phase achievement of a pure LSiPS phase could then produce an even more stable configuration. Interestingly, LSiPS_0

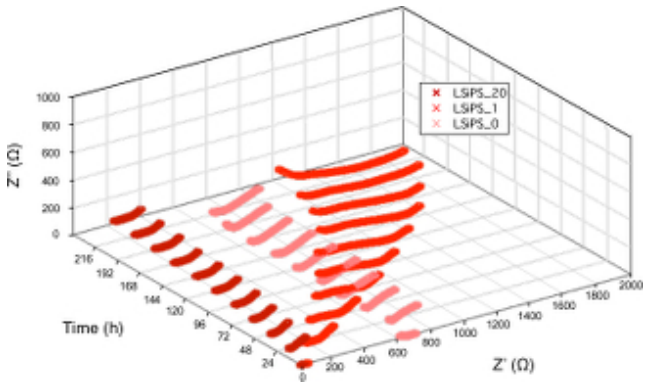

Figure 4.7: Time dependence Nyquist Plot of LSiPS_20 (dark red), LSiPS_1 (red), and LSiPS_0 (light red) in a symmetric cell versus lithium metal. The axis going into the page represents time. Despite LSiPS_20 and LSiPS_1 containing the same crystal, LSiPS_1 demonstrates a much larger growth in resistance due to electrolyte decomposition. This is proposed to be due to the larger amount of $Li_{3.2}Si_{0.2}P_{0.8}S_4$ contained in the sample.

appears to be near completely stable versus lithium, however, its low conductivity does not make it a good candidate for a superionic conducting electrolyte.

LSiPS_20 and LGPS were assembled into half-cells with a 4 cycles of atomic layer deposition (ALD) Al_2O_3 coated $Li(Ni_{1/3}Mn_{1/3}Co_{1/3})O_2$ working electrode and a lithium metal counter electrode. Figure 4.8a shows the first 75 cycles of the cells at a rate of C/10 at 30°C. Expectedly, the LGPS-based cell degrades quite readily whereas LSiPS is exceptionally stable. The capacity degradation is further elucidated when analyzing capacity normalized to the third cycle (Figure 4.8b). Previous reports have focused on the enhanced compatibility of ALD-coatings with solid electrolytes, therefore, cycling stability in this case is a direct indication of lithium stability. Figure 4.8c, 4.8d, and 4.8e assess the varying overpotentials of both cells during cycling by comparing each cell's voltage profile to equilibrium points obtained for a $Li(Ni_{1/3}Mn_{1/3}Co_{1/3})O_2$/Li half cell. During the first discharge and second charge, both samples have near identical profiles, however LSiPS_20 exhibits a slightly smaller overpotential and higher average voltage. By cycle 37, the LGPS cell's voltage plateau has dropped significantly (Figure 4.8d) and further compounded to a near unusable state by the 75th cycle (Figure 4.8e). This lowering of the voltage becomes extremely important when assessing energy density. In both samples, the discharge overpotentials are much greater than the same cycles' charge overpotentials. It is proposed that this is due to lithium ion

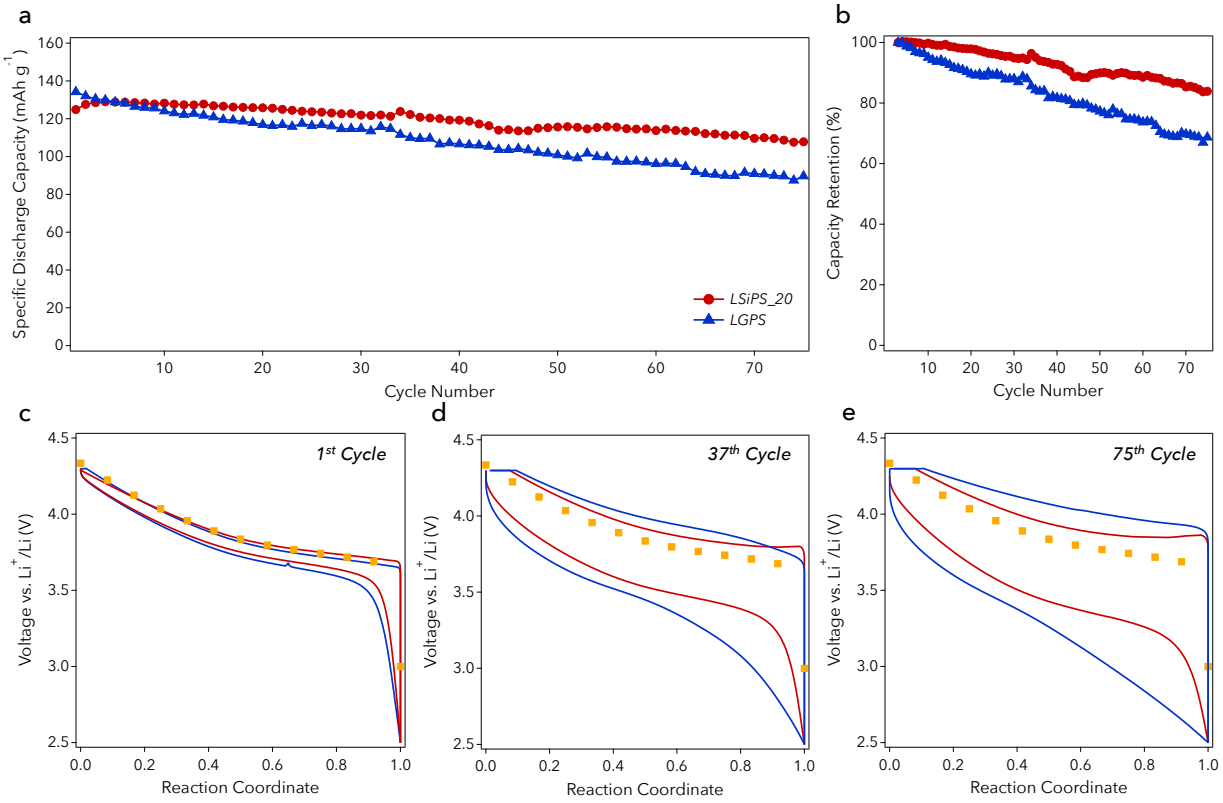

Figure 4.8: a) The 1st 75 cycles of $Li(Ni_{1/3}Mn_{1/3}Co_{1/3})O_2$ electrodes using LSiPS_20 (red) and LGPS (blue) as electrolytes galvanostatically cycled at C/10, b) Capacity retention of cells shown in Figure a. Values are normalized to their respective third cycle capacity's, c) The first discharge and second charge voltage profiles of the cells, d) The 37th discharge and 38th charge voltage profiles of the cells, e) The 75th discharge and 76th charge voltage profiles of the cells. For c-e, profiles are normalized to 100 of their maximum capacity for easy comparison. Orange markers are the equilibrium values obtained through GITT of $Li(Ni_{1/3}Mn_{1/3}Co_{1/3})O_2$ in a liquid cell.

movement across the passivation layer during discharge, and reduction of lithium at the passivation layer interface upon charge. The lower ionic conductivity of the passivation layer would then be the most significant factor attributing to the mass transfer overpotential. Further studies are currently being performed to optimize the use of LSiPS against lithium metal which would aid in the production of a longer cycling cell.

4.3 Conclusion

We have reported on the third analog to the superionic conductor of LGPS. Replacement of costly germanium with silicon produced the LSiPS crystal, $Li_{10}SiP_2S_{12}$, displaying a conductivity

of 2.3 x 10^{-3} S cm^{-1} prior to sintering, which is greater than LGPS under the same conditions. Additionally, LSiPS demonstrates an excellent stability versus lithium metal and compatibility with high voltage cathode materials, manifested in enhanced cycling stability over LGPS in a secondary lithium metal battery configuration. This report also represents experimental verification of predictive modeling performed on the family of $Li_{10}MP_2S_{12}$ superionic conductors.

Chapter 5

Ultrathin Solid-State Li-Ion Electrolyte Membrane Facilitated by a Self-Healing Polymer Matrix

5.1 Introduction

Emergent technologies are driving iterations of the lithium-ion battery to exhibit enhanced safety and higher temperature capabilities.[44,211] The commercial lithium-ion battery remains relatively unchanged since its inception in 1991. As such, it would be challenging to adopt the current liquid electrolyte system ($LiPF_6$ dissolved in ethylene carbonate/diethyl carbonate) for safety concerns due to flammability.[193] Batteries encompassing inorganic solid electrolytes, known as solid-state batteries, have attracted significant attention in recent years due to resolution of overheating and thermal runaway, as well as lithium ion conductivities matching liquids yet still maintaining a lithium transference number of unity.[72,100,152] With commercial deployment rapidly approaching, most solid-state research focuses on electrode compositions or electrolyte chemistries.[76,173,195] Few reports emphasize the implicit challenges in the design of an all-solid-state battery, often reworking the solid system to mimic processing of a liquid-based system.[150] However, solids present vastly different mechanical and fundamental properties. Novel processes and approaches must be employed if solid electrolyte batteries are to be advanced to commercial viability.

Liquid electrolyte systems have the inherent advantage of maintaining intimate contact with electrode materials. A successful solid electrolyte must likewise conform its surface to establish close contact with electrode surfaces.[57,153] There are two main classes of inorganic, solid, lithium

electrolytes: oxides and sulfides. Oxide electrolytes, while maintaining stability in air, suffer from a lack of compatibility with standard electrode materials, require sintering at elevated temperatures, and possess high charge transfer resistances due to poor electrolyte-electrode contact.[212,213] Oxide electrolytes tend to exhibit shear moduli of greater than 50 GPa. Intimate contact with battery materials is therefore precluded due to the lack of plastic deformation under stress.[214] On the other hand, the sulfide family of solid electrolytes, such as $Li_{10}MP_2S_{12}$ crystals and $Li_2S - P_2S_5$ glass-ceramics, have lithium ion conductivities comparable to liquid electrolytes, can be simply processed by cold-compacting the powders, and exhibit ductile-like mechanical properties.[72,126,153] Thus, the present study makes use of the sulfide family of solid electrolytes, namely the "a77.5" $77.5Li_2S - 22.5P_2S_5$ glass-ceramic.

Assembly of laboratory bulk solid-state cells occurs by applying high pressures to the powder forms of the cathode, electrolyte, and anode thus forming a tri-layer pellet.[215] Due to the brittle nature of the materials being used, if the separator layer is less than approximately 1 mm, cracking tends to develop through the pellet rendering the cell useless.[216] Limited research has focused on reducing this layer thickness while maintaining a bulk configuration (non-thin film battery). PLD and CVD have been used to deposit thin solid films demonstrating excellent cycling performance;[217–219] high vacuum deposition techniques, however, are extremely expensive and do not present a scalable process for commercial development of the solid-state battery. A few studies were identified introducing the classic process of a polymeric binder to the inorganic solid.[151,216] In doing so, the polymer acts to coat the electrolyte particles impeding interparticle contact, requires a substrate to coat on negating free-standing applications, and doesn't allow absolute density which hinders electrode performance.

Therefore, an optimal method of processing a solid-state battery would encompass a cheap, scalable process, one that doesnt impede the conduction capabilities, and the materials used should be mechanically pliant to suppress cracking. In this work, we report a new method of developing a solid electrolyte-in-polymer matrix (SEPM) to form our electrolyte layer. This method takes advantage of the fact that the solid electrolyte pellet is about 15% porous in the green body

state.[220] By filling empty voids with an organic polymer, we can create a cross-linked polymer matrix in situ to provide mechanical robustness while preserving lithium ion transport pathways in between solid electrolyte particles. Using a newly derived malleable thermoset polymer paired with a $Li_2S - P_2S_5$ inorganic electrolyte, we produce a stand-alone membrane of 64 µm in thickness, high active material loading (80%), and near theoretical density. The membrane performs on par with traditionally prepared solid-state batteries yet has increased the gravimetric and volumetric cell energy densities by an order of magnitude. The processing of our SEPM is completely dry representing not only a new method of processing for batteries, but a technique to form other composites such as high mass-loading mixed matrix membranes.

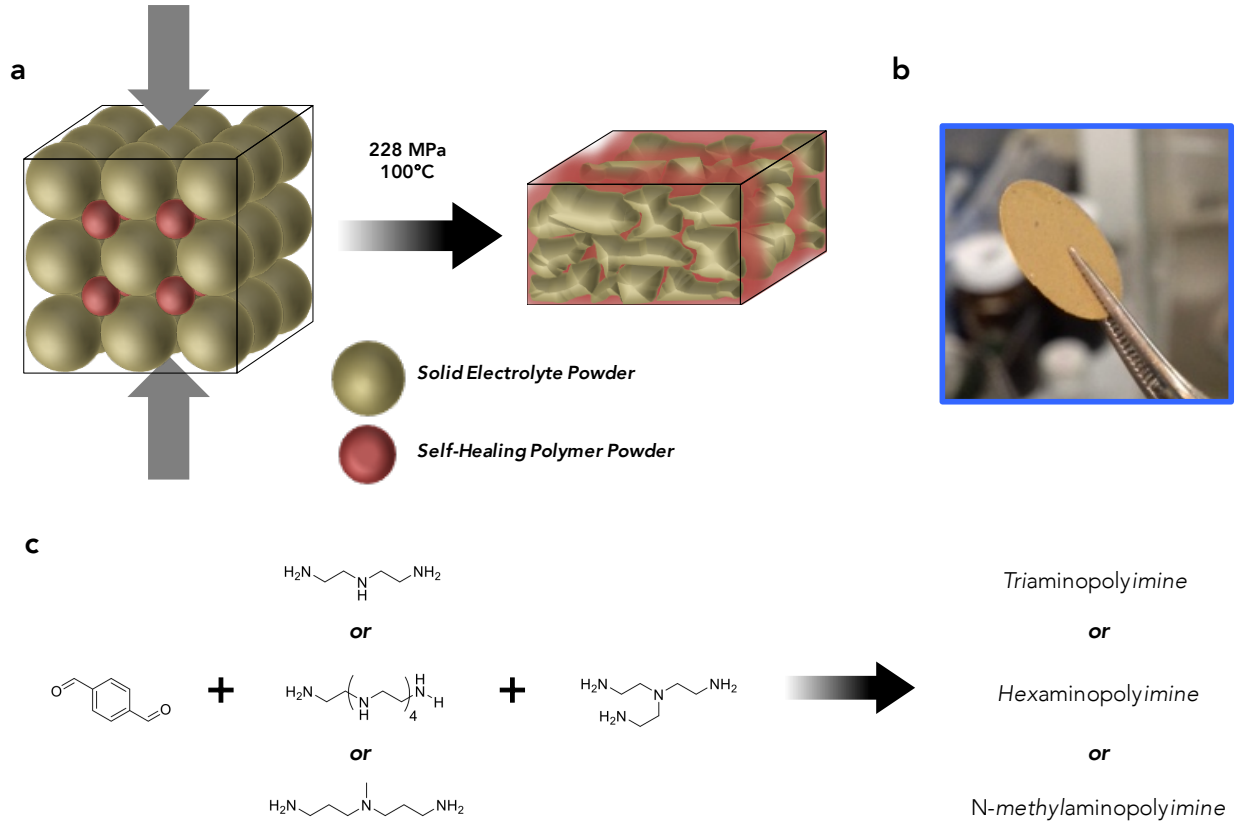

Figure 5.1: (a) Schematic for forming the solid electrolyte in polymer matrix membrane. Through the application of heat and pressure, malleability is achieved in the polyimine forming a continuous network without sacrificing solid electrolyte particle contact. (b) Free-standing solid electrolyte separators thinner than 100 µm can thus be made. (c) The synthesis process for creating the polyimine formulations: tri-imine, hexa-imine, methyl-imine.

5.2 Results and Discussion

Work in this section has been presented in the 2015 publication.[221] Membranes based on the traditional thermoplastic polymers suffer from active material agglomeration and sedimentation.[222] Additionally, the melt-flow behavior of thermoplastic polymers leads to highly resistive surface coatings that inhibit interparticle conductive contact. Thermoset materials, which must be cured in situ, exhibit the same drawbacks as the thermoplastic. Recent advances in polymer chemistry have led to the development of malleable covalent network polymers, often called vitrimers. Vitrimers are capable of stress-relaxation and flow due to dynamic covalent bonding of reversible crosslinks within the network.[223–225] Network polyimines were used in this study: they are simple to prepare (one step from commercially available monomers), and contain no metal catalysts, which could demonstrate undesired redox activity.[226] Figure 5.1a represents the SEPM concept. Starting in a bulk powder form, and taking advantage of the malleable properties of the polyimine, our hot iso-static press will theoretically form a continuous cross-linked network interspersed between the voids of the glass-ceramic solid electrolyte. The malleability of polyimines allows for material flow to increase the density of the composite, and instill mechanical toughness, with a minimal impact on the ionic conductivity of the electrolyte. This process does not preclude interparticle contact of the solid electrolyte particles as only a few domains of polymer are introduced. This stands in stark contrast to polymeric binders used in solution processes; these act to coat all surfaces of each individual solid electrolyte particle. Figure 5.1b is an image of a prepared SEPM membrane approximately 100 μm in thickness with 80% mass loading solid electrolyte.

The original polyimine synthesis was reported previously.[226] In this work, new variations of the polyimine were developed by replacing the monomer diethlyene triamine with pentaethylene hexamine or 3,3'-diaminodipropyl-N-methylamine. The structures of the monomers are given in Figure 5.1c along with nomenclature used for the rest of this study: tri-imine, hexa-imine, methyl-imine. Increased elasticity is achieved by either creating a more open framework (hexa-imine) or reducing the degree of hydrogen bonding (methyl-imine). Figure 5.2 reveals the room temperature

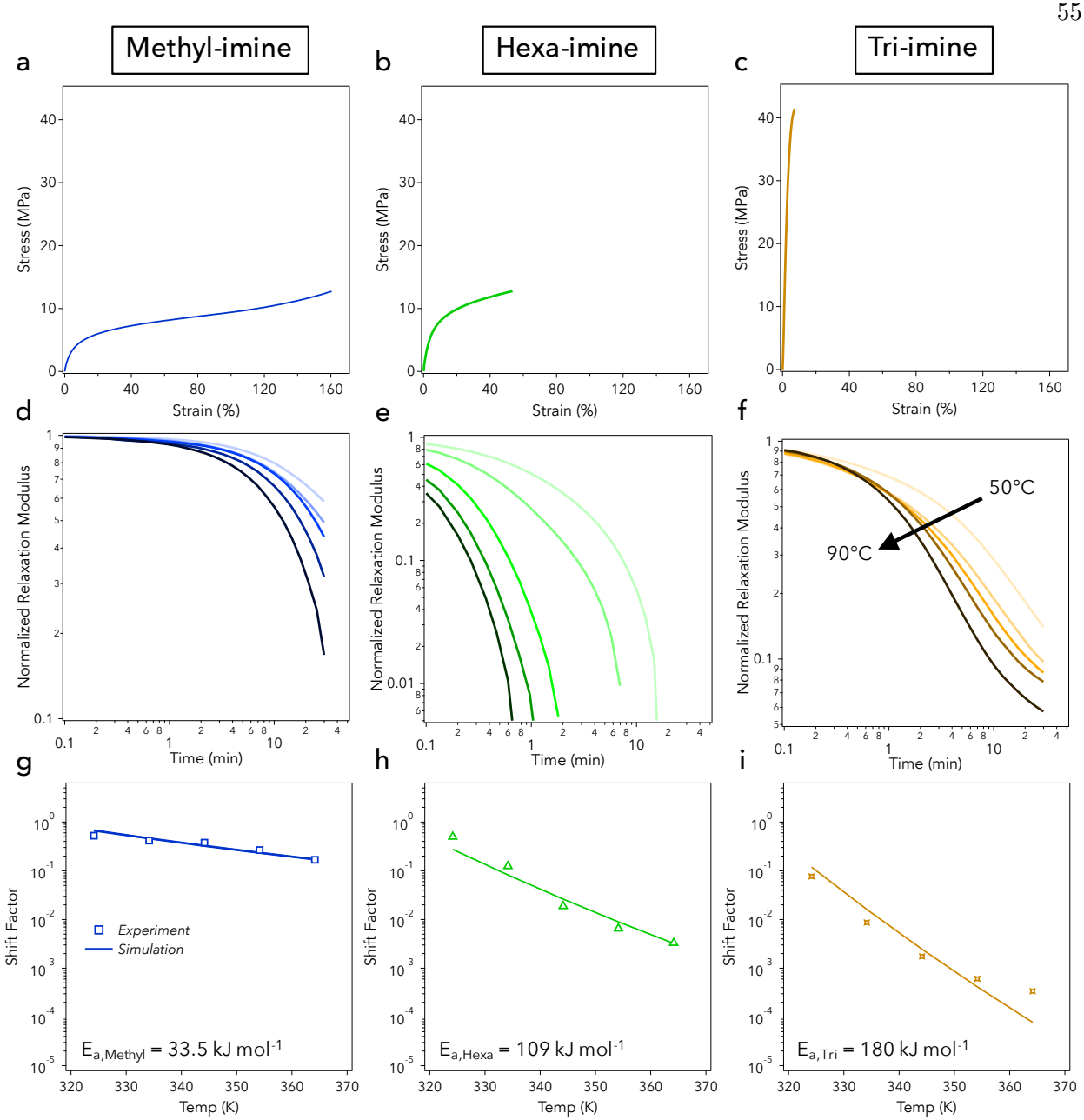

Figure 5.2: Room temperature stress-strain curves for methyl-imine (a), hexa-imine (b), and tri-imine (c). Stress relaxation curves at various temperatures a 30 minute period for methyl-imine (d), hexa-imine (e), and tri-imine (f). Shift-factor vs. temperature plot of temperature-time superposition experiment for methyl-imine (g), hexa-imine (h), and tri-imine (i).

mechanical performance, as well as temperature-dependent stress-relaxation of 3 formulations of network polyimine. The polymers were prepared by mixing the ethanolic solutions of the monomers in molar ratios of 1:0.45:0.367 (terephthaldehyde to diamino linker to tris(2-aminoethyl)amine). The mixture was added to a tray of silicone-coated paper, and the ethanol was allowed to evaporate.

After curing the films in a heat press (1 hr 100°C), the solid polymers were ground to powder using sand paper. The self-healing behavior of the methyl-imine formulation is due to its room temperature malleability, and the powders and films of this formulation are observed to heal into coherent solids when left under gentle pressures at room temperature. Full characterization of the self-healing behavior and healing efficiencies is forthcoming.

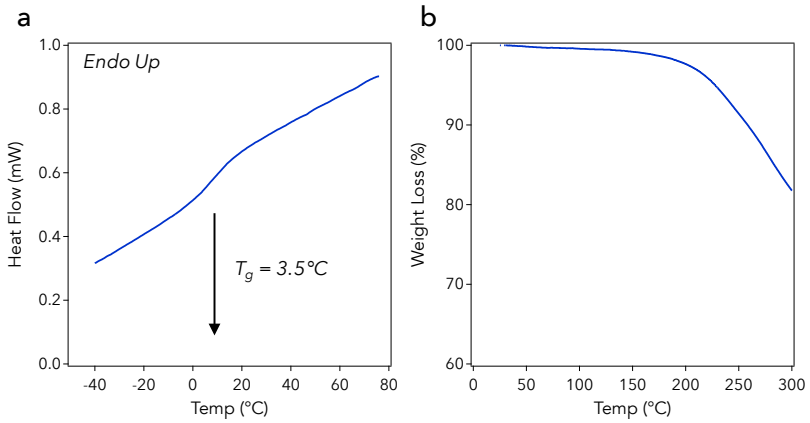

Figure 5.3: (a) DSC thermogram of methyl-imine and determination of T_g by the onset method. (b) TGA curve of methyl-imine.

Figure 5.3a and 5.3b presents the differential scanning calorimetry (DSC) and thermogravimetric analysis (TGA) results of the methyl-imine formulation. DSC measurements were carried out on a Mettler Toledo DSC823e at a 5°C min^{-1} scan rate. Samples were run on a TA Instruments Q-500 series thermal gravimetric analyzer with samples held in a platinum pan under nitrogen atmosphere; a 10°C min^{-1} ramp rate was used. Methyl-imine has a glass transition temperature at 3.5°C and loses about 1 of its mass by 162°C. This mass loss would be the limiting factor for using SEPM based solid-state batteries at elevated temperatures as the a77.5 solid electrolyte is stable up to the crystallization temperature.[227]

To compare membrane properties, all the formulations as well as pure solid electrolyte were prepared into pellets approximately 1 mm thick. Table 5.1 presents the densities, room temperature ionic conductivity, and activation energies of the SEPMs. Figure 5.4a to 5.4d are the AC impedance results of a77.5 and the three SEPMs. A steep tail at low frequencies indicates good contact was made between the Ag-blocking electrodes and electrolyte layer. The measured experimental

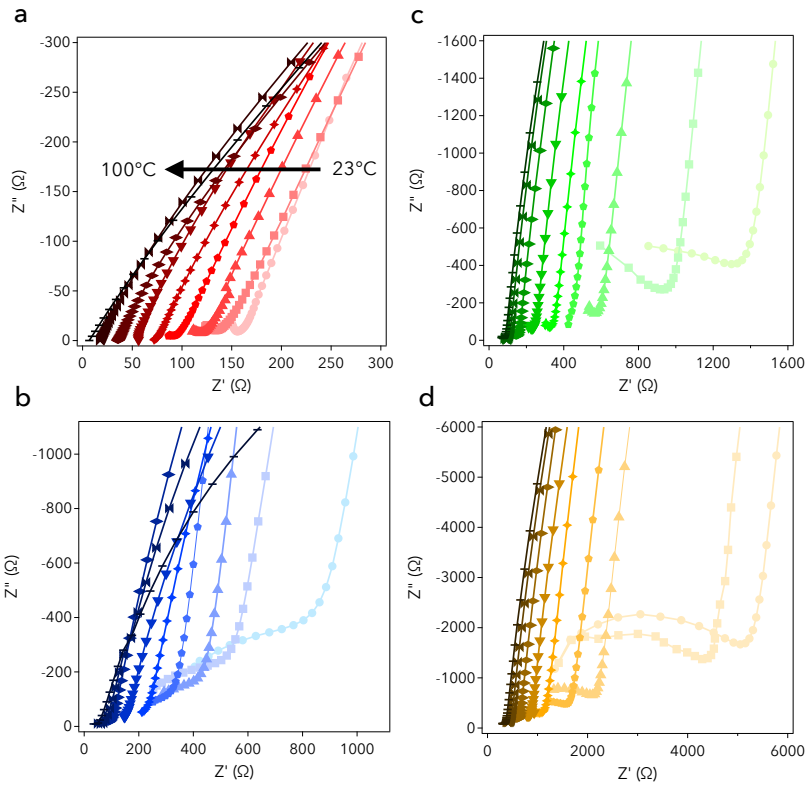

Figure 5.4: Nyquist plot as determined by AC Impedance for the temperature range between 23°C to 100°C for a77.5 (a), methyl-imine composite (b), hexa-imine composite (c), tri-imine composite (d).

densities of the SEPMs as a function of the theoretical density are displayed in Figure 5.5a. The pure a77.5 pellet measures a relative density of 0.85 or about 15% porous. The most elastomeric polyimine, methyl-imine, forms an SEPM with a relative density of about 0.97. This is an excellent result as full density improves solid electrolyte contact. Although addition of the polyimine does reduce overall conductivity, methyl-imine SEPM achieves a room temperature conductivity of 1 x 10^{-4} S cm^{-1}. This is on the same order of magnitude as the bulk electrolyte. It is important to determine if there is any impact of the polyimine on conductive abilities of a77.5; this can be seen in the Arrhenius plots for the SEPMs (Figure 5.5b). It is clear that for each polyimine, no change in activation energy occurs. Activation energy is a fundamental material property for ionic motion that defines the energy barrier to ion hopping, and it can therefore be concluded that any decrease in conductivity from a pure a77.5 separator by the addition of polyimine is simply due to the inclusion of resistive domains. This is supported by the trend of decreasing ionic conductivity

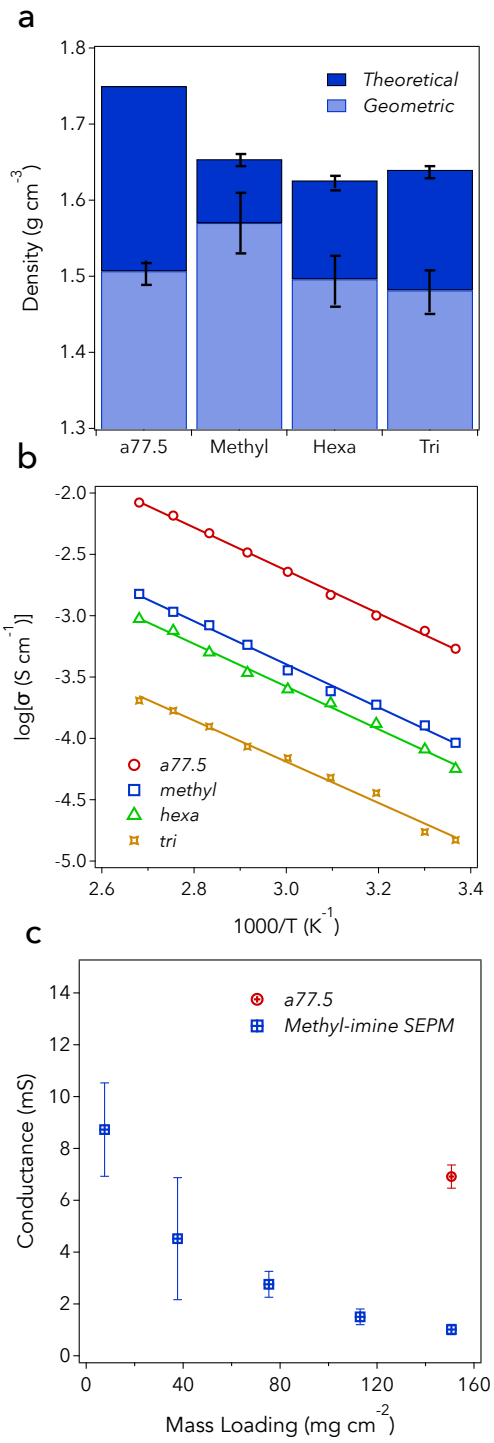

Figure 5.5: (a) Theoretical and geometric densities of SEPM membranes consisting of 80% a77.5 and 20% polyimine. The most elastomeric polyimine formulation, methyl-imine, achieves a relative density approximately 0.97 indicating a microstructure without voids is created. (b) Arrhenius plot of SEPMs. (c) Conductance of electrolyte membranes as a function of mass loading (thickness). The methyl-imine based SEPM achieves a conductance greater than a pure a77.5 separator at a mass loading of 7.5 mg cm^{-2} which corresponds to a thickness of 63.7 µm.

with decreasing elasticity of the polyimine, ie. larger domain sizes.

Table 5.1: Summary of SEPM composite membrane properties. All composites consist of 80% solid electrolyte by weight.

Material	Theoretical Density [g cm^{-3}]	Composite Relative Density	Composite $\sigma_{25°C}$ [mS cm^{-1}]	Composite Activation Energy [kJ mol^{-1}]
a77.5	1.75	0.85 ± 0.01	0.54	34.7
Methyl-imine	1.07 ± 0.02	0.97 ± 0.02	0.092	34.8
Hexa-imine	0.93 ± 0.02	0.94 ± 0.02	0.056	34.5
Tri-imine	1.00 ± 0.02	0.92 ± 0.02	0.015	33.3

The overarching goal is to achieve a membrane with thickness less than 100 μm with a greater conductance than a pure a77.5 separator. The methyl-imine SEPM is pursued due to its high bulk conductivity. The thickness of the methyl-imine SEPM is reduced and its conductance value is measured rather than conductivity, more reflective of battery performance. The mass loading of the separator is normalized to area to account for any variations in thickness between the samples. Results are displayed in Figure 5.5c. It should be noted that although these SEPMs were processed at elevated temperature, these same structures could also be formed at room temperature as methyl-imine demonstrates malleable properties at ambient conditions. However, in order to speed up this process, increased temperature is applied. A clear inverse trend is evident meaning a linear resistance decrease is present with decreasing SEPM thickness. At a mass loading of 7.5 mg cm^{-2}, the SEPM achieves a greater conductance than a pure solid electrolyte membrane. This could be extrapolated for any solid electrolyte used, so that one should always be able to achieve a greater conductance than the solid electrolyte counterpart at this thickness level. Increased amount of error occurred at the thinner levels due to variations in the Ag-blocking electrode areas.

Figure 5.6 displays this measurement on un-heat-treated composites in contact with lithium metal at 60°C to exacerbate any possible interactions. This serves the dual purpose of also measuring long-term stability with lithium and polyimine. As it can be seen, there are no general increases across any samples. a77.5 is already known to be stable in contact with lithium metal.

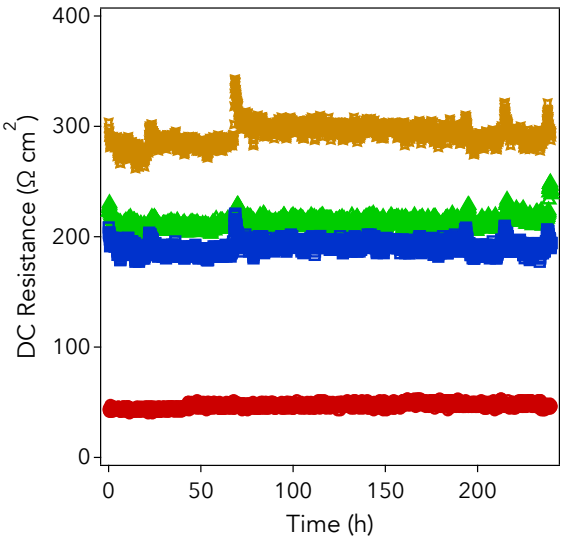

Figure 5.6: Long-term DC resistance of SEPMs in contact with lithium metal electrodes at 60°C; fluctuations are due to changes in oven temperature.

A few fluctuations occur across the 10 days in the polyimine samples. As they occur at the same times, it can be concluded that this is directly due to temperature changes in the oven (opening the oven door).

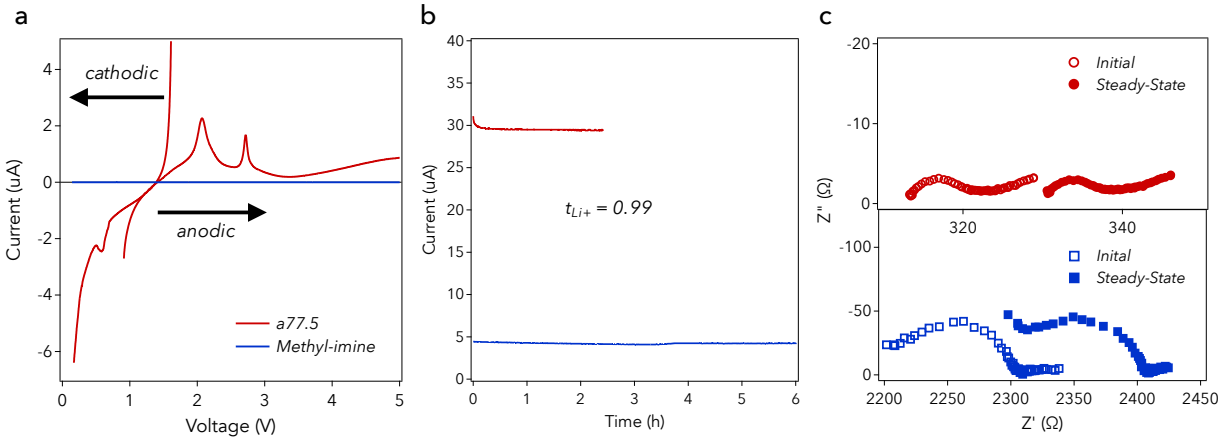

Figure 5.7: (a) Cathodic and anodic linear sweep voltammetry of pure a77.5 and methyl-imine. Peaks in the anodic a77.5 sweep are attributed to excess Li_2S in the electrolyte. Methyl-imine appears to be electrochemically inert to lithium in the range of 0 - 5 V. (b) Transference number of pure a77.5 separator and methyl-imine SEPM. Both cases exhibit a lithium ion transference number of 0.99 indicating methyl-imine does not contain any mobile species and does not affect conductive abilities of the solid electrolyte. (c) Initial and steady-state impedance sweeps required to calculate transference number values.

We wanted to further probe the electrochemical characteristics of the polyimine material.

First, it is worth seeing if the polyimine is lithium active. Electrochemical stability (Figure 5.7a) is tested using linear sweep voltammetry (LSV) with a lithium/a77.5/polyimine/titanium construction at a scan rate of 1 mV s^{-1}. LSVs are performed from OCV up to 5 V and down to 0.1 V corresponding to anodic and cathodic sweeps, respectively. Anodic and cathodic sweeps yielded no response meaning no interaction between the two. This is expected as methyl-imine is neither electrically or ionically conductive, a necessity to have some reduction of lithium ions. Second, in order to see if there are any mobile species within methyl-imine, we tested lithium ion transference number in both pure a77.5 and the methyl SEPM (Figure 5.7b). Solid superionic conductors are well known for having transference values of unity meaning the only mobile species are lithium ions hopping between vacancies. In the SEPM, we see the same value showing no negative interactions caused by the addition of polyimine. Figure 5.7c displays the initial and steady-state impedance sweeps used to calculate transference number.

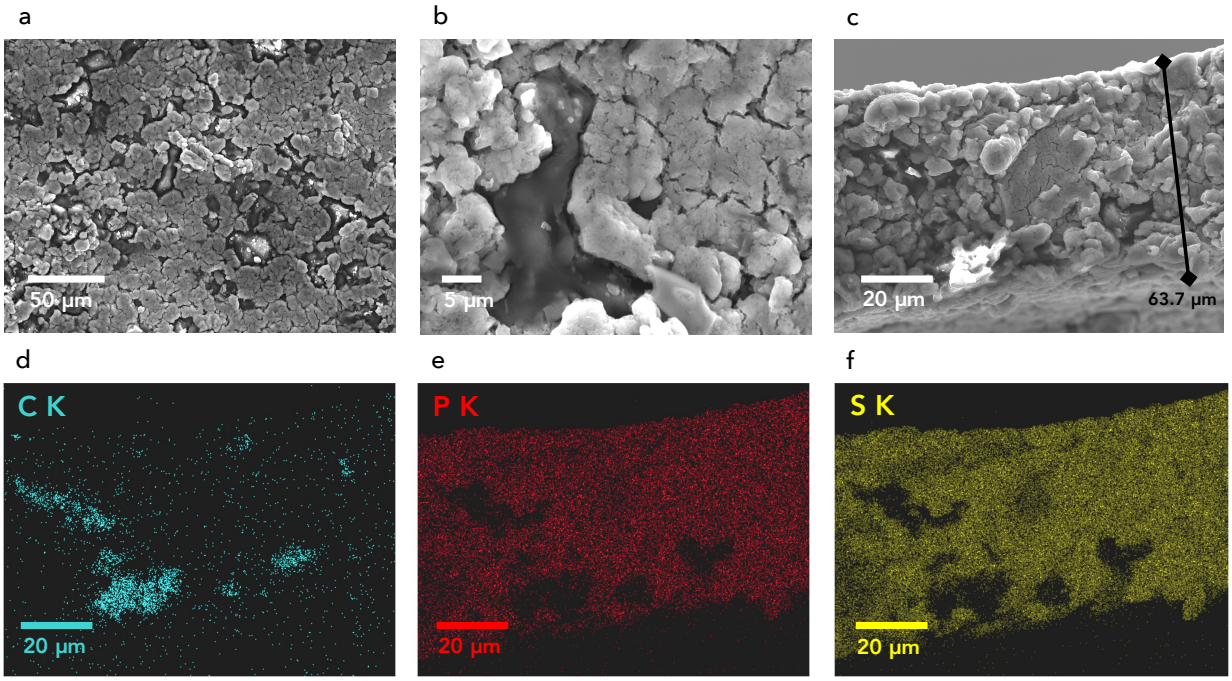

Figure 5.8: SEM of 7.5 mg cm^{-2} methyl-imine SEPM top (a), zoomed in interface of polyimine and electrolyte (b), and cross-section, (c). EDS map of C-K, (d), P-K (e), and S-K (f) in cross-section. The polyimine, registered as carbon, penetrates the voids between the solid electrolyte.

To confirm the hypothesized structure of self-healing polymer dispersed throughout a densi-

fied solid electrolyte, SEM is used to image the top and cross-sectioned view of the 7.5 mg cm^{-2} methyl-imine SEPM, Figure 5.8a and 5.8c, respectively. Methyl-imine is observed to be well-dispersed with domain sizes on the order of a few microns. Figure 5.8b is an enhanced view of the interface between polyimine and a77.5. The interface appears to be continuous, demonstrating the ability of the methyl-imine to flow through the electrolyte pore-space. This confirms the idealized structural mechanism of filling the voids of the solid electrolyte with polymer. The cross-section of SEPM methyl-imine reveals a thickness of 63.7 μm. To track dispersion and interconnectedness of polyimine, EDS is used to distinguish between polyimine and a77.5. Figure 5.8d, EDS map of C K signal, represents the polyimine and Figure 5.8e and 5.8f, EDS maps of P-K and S-K respectively, represents the a77.5. It is clear that the polyimine is well-dispersed and domains appear connected. Ostensibly, the bottleneck for reducing the thickness of the SEPM further is dependent on the following polyimine parameters: flow, particle size, and distribution within composite. Further work will be focused on using a lower cross-linked density polyimine and exploring techniques such as cryogenic ball-milling.

To demonstrate its application, the methyl-imine SEPM is investigated as a functional separator in an all solid-state lithium ion battery. A cathode containing 45% weight FeS_2 is mounted on an SEPM of mass loading 7.5 mg cm^{-2} using uni-axial compression.[173] Figure 5.9a displays a symmetric rate study comparing discharge performance of the SEPM cell to a standard a77.5 construction. Associated voltage profiles are shown in Figure 5.10. It can be seen that the main difference between the two cells is the larger ohmic overpotential associated with the a77.5 separator leading to lower capacity. At cycle 5, the cell achieves a specific capacity of around 450 mAh g^{-1} (mass normalized with respect to the full electrode). This corresponds to a FeS_2 specific capacity of 1000 mAh g^{-1}. Greater than theoretical capacity can be achieved through electrochemical activation of the sulfide components of the electrolyte.[228] The SEPM shows enhanced rate capability due to the greater conductance value of the separator manifesting in a smaller ohmic overpotential. The identical capacity retention of both cells results from identical FeS_2 reaction kinetics, inherent to the cathode itself. Figure 5.9b shows long-term cycling at a rate of C/5. Over 200 cycles, the

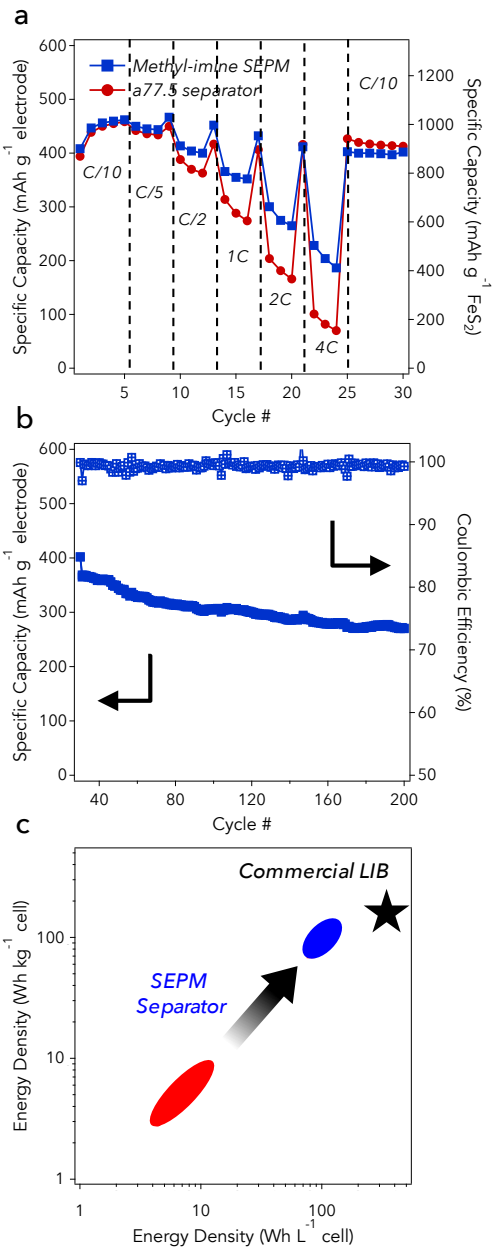

Figure 5.9: (a) Rate study of an FeS_2 cell using a standard a77.5 separator and a methyl-imine SEPM separator. Greater capacity values are attributed to greater conductance and thus less ohmic overpotential. (b) Long-term cycling of cell at C/5. 74% capacity retention is achieved after the 200th cycle. (c) Enhancement in gravimetric and volumetric energy densities by moving to a SEPM configuration.

SEPM-based battery retains 74% capacity constituting one of the longest-lasting bulk FeS_2 cells reported to date.[126,168,228] Evolution of the voltage profile in this region is displayed in Figure 5.10. The loss in capacity is attributed to a shortening of the lower plateau due to the slower kinetics in the conversion reaction. While capacity is lost during this period of cycling, the energy density does not degrade nearly as much as the high voltage region remains relatively intact. By measuring out the cathode tap density, we report on the volumetric and gravimetric cell-based energy density values. By replacing the thick a77.5 separator with the methyl-imine SEPM, the cell-level energy density values are increased by an order of magnitude and rapidly approach commercial lithium-ion battery values.[179] Additional work to improve cathode capacity can further enhance this value.

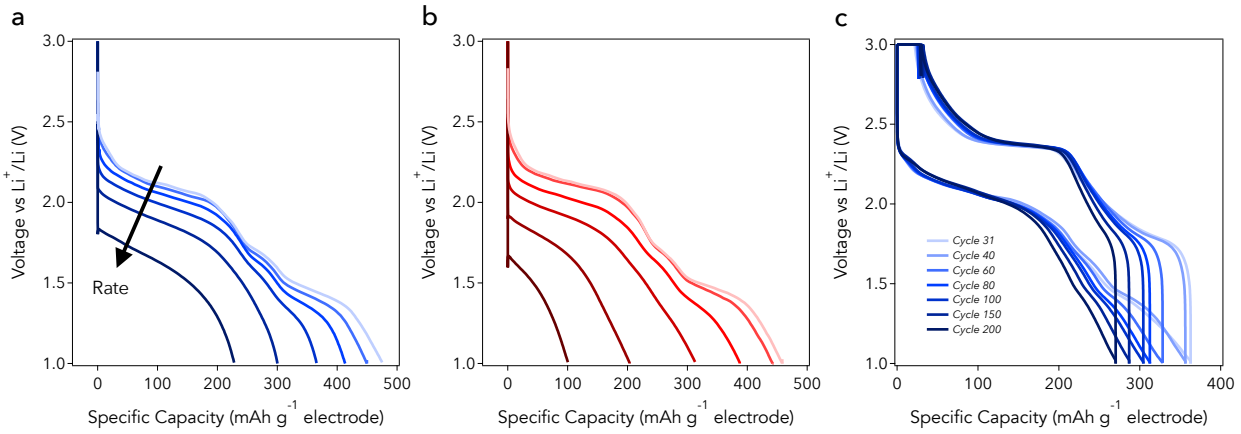

Figure 5.10: (a) Voltage profiles of rate study using methyl-imine SEPM, (b) Voltage profiles of rate study using a77.5 separator, (c) long-term cycling voltage profile evolution of methyl-imine SEPM cell.

5.3 Conclusion

We have presented a new strategy for forming a thin electrolyte membrane by creating a solid electrolyte-in-polymer matrix. An in-situ derived polymer matrix can be formed by penetrating the void space of an inorganic solid, green compact through reversible cross-links of the self-healing polymer. Essentially a mixed-matrix is formed with a high mass loading of 80% solid electrolyte by weight. This constitutes an order of magnitude improvement in thickness from a 1 mm to a 64 μm separator, achieving a greater conductance, and increasing relative density to 97%. The

desired structure is confirmed with SEM and EDS. The SEPM, when used as a separator in an all-solid-state battery with a FeS_2-based cathode, achieves excellent rate capability and stable cycling for over 200 cycles. This is the first report of a self-healing material being used to create a solid membrane and first application in a solid-state battery. Processing in the dry condition could represent a paradigm shift for incorporating high active material mass loadings into mixed-matrix membranes.

Chapter 6

Stable Lithium Deposition Using a Self-Optimizing Solid Electrolyte Composite

6.1 Introduction

The most energy dense battery configuration utilizes lithium metal as an anode material providing a large specific capacity and high operating voltage. However, upon charging, lithium forms heterogeneous depositions, which propagate into moss-like strands called dendrites. Full growth through the cell causes a short and many safety issues especially in commercially available configurations such as thermal runaway and combustion.

In the 1960s, dendrite growth was studied and modeled in Silver and Zinc deposits by Barton and Diggle, respectively.[229,230] Yamaki later studied the morphology of lithium depositions developing a correlation between the critical radius for the onset of dendrite growth and interfacial energy between lithium and the separator.[231] These models, among others, were incorporated by Monroe and Newman to predict that for dendrite suppression the ratio of electrolyte to lithium metal shear moduli only be 1.8 or greater (for materials with comparable Poissons ratio with lithium).[232] Dendrite suppression is predicted for materials exhibiting a negative stability parameter. These models were focused on liquid and polymer electrolytes, and the principles are tougher to translate to solid separators. Sulfide glass-ceramic electrolyte cold-compacted has been shown to have a shear modulus meeting the requirement laid out by Monroe and Newman. However, it has been observed that dendrites grow along solid electrolyte particle boundaries. In fact, due to surface roughness of a solid electrolyte separator, most likely dendrite precursor tips are already formed on

either plating of lithium or attachment of lithium to make adequate contact. Once dendrites begin to form in the solid separator, the simple shear modulus requirement to prevent dendritic onset will no longer be valid. A variety of parameters will most likely come into play such as the plating mechanism, porosity of compact, and Youngs Modulus of the electrolyte. Surprisingly, there have been no models of dendrites growing through solids and therefore, solid dendrite growth is not well understood.

There have been a variety of methods attempted to surpress dendrite growth using a solid electrolyte. Some of these focus on improving the overall quality of interface between lithium/electrolyte,[118] some introduce a buffer layer between lithium and the solid electrolyte,[233] changes to electrolyte density are performed,[234] or others changes the lithium microstructure.[235] The results of these attempts are mixed and none truly demonstrate a definitive dendrite blockage.

Herein, we investigate the ability of our solid electrolyte in polymer membrane (SEPM) system, developed in Section 5, to suppress lithium dendrites. We discover a correlation between the ease of self-healing with the amount of capacity passed and rate capability. We conclude that this is not an effect of the introduction of any polymer into the solid electrolyte system, but is specific to the imine-based self-healing polymer. We postulate that the polymer acts to optimize an interface between lithium and the solid electrolyte as well as form an optimized matrix between solid electrolyte particles.

6.2 Results and Discussion

Figure 6.1 is a scanning electron microscopy (SEM) top view of the microstructure formed by including methyl-imine self-healing polymer (polyimine) with the sulfide solid electrolyte (SSE). The weight percent of polyimine is 30%. Intimate interfaces are evidently formed between electrolyte and polymer, however, the polymer originates as large domains.[221] There are clearly many SSE/SSE interfaces without the presence of polyimine. In the upcoming sections, it will be discussed how these large domains of polyimine are beneficial over the course of lithium deposition.

For lithium deposition tests, symmetric cells with lithium foil electrodes are used. The sepa-

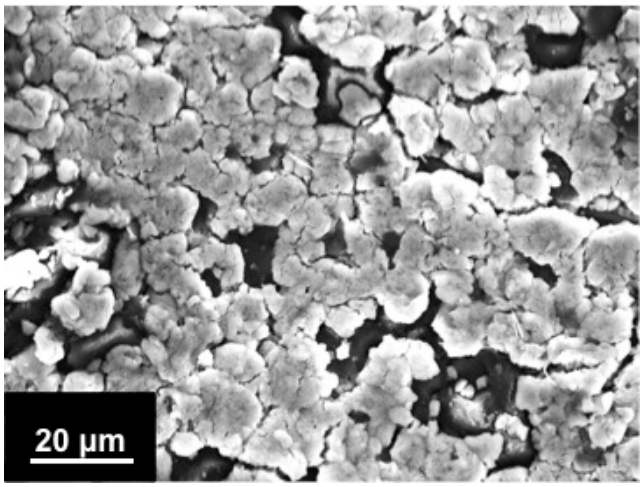

Figure 6.1: SEM of top view of composite consisting of 70% solid electrolyte (light) and 30% methyl-imine (dark). The polyimine is well dispersed and there is intimate contact between SSE and polyimine. The particle size of the polyimine is also quite large, from 1 to 20 µm.

rator is formed using the methodology in Section 5 which includes a heated press. The separators are approximately 0.5 mm in thickness. Lithium is then attached on either side using consistent pressure. The amount of pressure has been optimized to allow for an effective interface to form between the solid separator and lithium. Cells are then applied a fixed current density and run until short (voltage drops to approximately 0 V). Figure 6.2 demonstrates the results of deposition tests using a variety of methyl-imine weights. With a low methyl-imine loading such as 20% weight, the system performs worse than a pure a77.5 separator. However, once the weight loading of methyl-imine is increased, the performance increases dramatically. A maximum is achieved with 30% methyl-imine loading in the hot-pressed separator; this is approximately nine times the performance of pure a77.5. A lower performance and significant oscillation in the voltage response in the 40% sample is most likely due to a poor interface formed from resistive polymer domains in contact with lithium metal and the formation of constriction resistances at the lithium/solid electrolyte interface.

The hot-pressed composite was investigated versus a separator prepared by cold-pressing the polyimine with the solid electrolyte. In this case, the polymer will act more like a filler and no bonding between polymer particles is expected. The result of this deposition test is also displayed

in Figure 6.2. The new separator passes significantly more charge than any of the hot-pressed separators, and doesn't short until about 61 mAh cm^{-2}. This is an unprecedented result and will be the subject of the rest of this section.

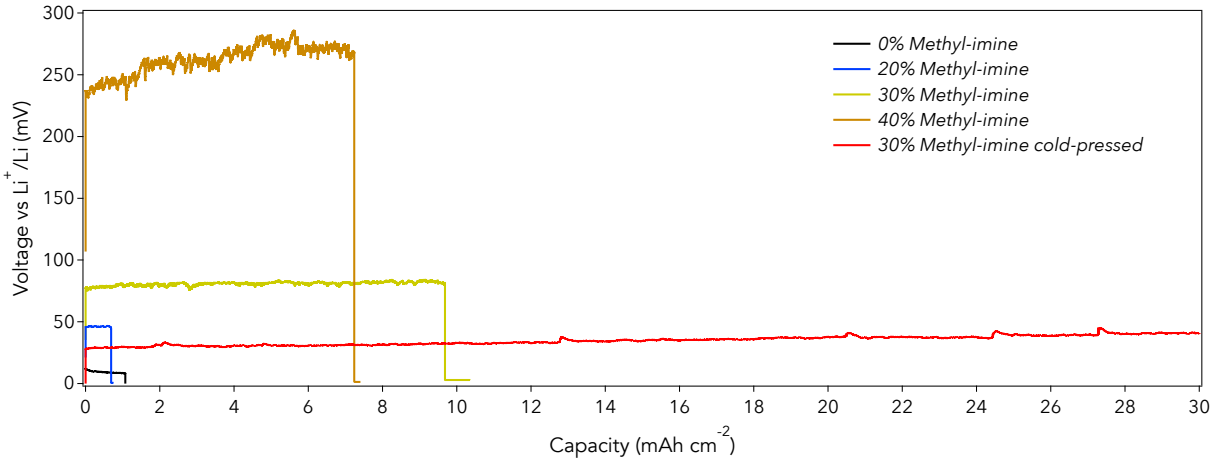

Figure 6.2: Galvanostatic plating in lithium symmetric cells containing a compositional range of increasing amount of polyimine for hot-pressed separators. For comparison, a test using a cold-pressed separator is also displayed. All tests occur at 0.1 mA cm^{-2} and 60°C. Separators are approximately 500 µm.

Figure 6.3 displays the effect of increasing amount of methyl-imine in the separator (cold-pressed) by means the of galvanostatic polarization tests at 0.1 mA cm^{-2} current density and 60 °C. A pure SSE separator will short close to 2 mA cm^{-2}. Even a small inclusion of polyimine allows for extended passage of lithium. All compositions pass over 25 mAh cm^{-2} without shorting. With only 10% polyimine, the overall cell resistance is only increased by approximately 10%. The higher conductivity of the separator is a benefit of using a small amount of polyimine. Additionally, the resistance with time (rising voltage) is smallest with the least amount of polyimine. This phenomenon will be addressed shortly.

For higher current tests, we focus on the conservative case of using 30% polyimine. Figure 6.4a is an example of a galvanostatic polarization test at 0.5 mA cm^{-2} current density and 60 °C operation. The pure SSE cell shorts at about 1 mAh cm^{-2}, an impracticable amount of capacity. Although the voltage doesnt fully drop to 0 at this value, this is what is referred to as a soft short. While it looks unsubstantial in this particular test, this feature will render a cell useless.[118] With the

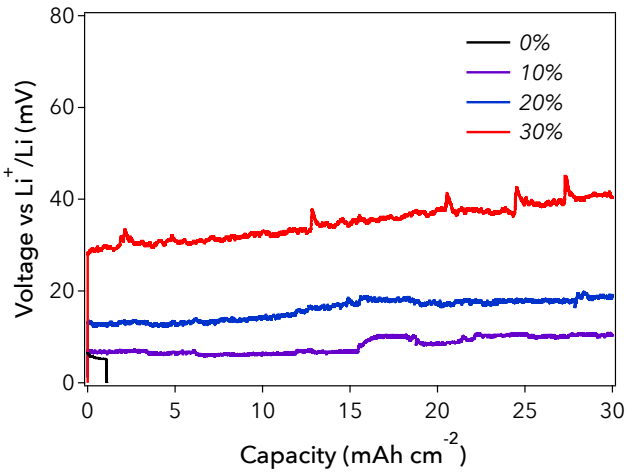

Figure 6.3: Composition study of cold-pressed separators with increasing amounts of polyimine. Even with 10% weight polyimine, the separator can pass over 30 mAh cm^{-2}. All tests occur at 0.1 mA cm^{-2} and 60°C. Separators are approximately 500 µm.

inclusion of polyimine, the capacity until short improves to 23 mAh cm^{-2}, a remarkable increase. A gradual resistance increase is detectable which will be explained in the upcoming section.

Figure 6.4b is a comparison of short circuit times (displayed in capacity) to current density applied for either the pure SSE or SSE/polyimine systems. Pure SSE can pass modest amounts of capacity at slower rates with a maximum of about 6 mAh cm^{-2} at 0.1 mA cm^{-2}. Once rate is increased to 0.5 mA cm^{-2} and above, there is little correlation between short capacity and rate for pure SE. A constant 1 mAh cm^{-2} is passed until short. It can be concluded that lithium dendrite morphology is not different at high rates in the solid as typically is found in liquid.[231] Since it is postulated lithium grows along particle boundaries, the 1 mAh cm^{-2} is directly related to the thickness of separator and is an analogue for the amount of lithium needed to traverse the 0.5 mm of the separator. A stark contrast is developed once polyimine is included into the composite. At slow current rates (0.1 mA cm^{-2} and 0.25 mA cm^{-2}), the composite is able to pass 25 mAh cm^{-2} without any short. These are incredibly high values being that current commercial cathodes do not exceed 3 mAh cm^{-2}. At extremely high current densities (1 mA cm^{-2}), the composite passes a similar amount of capacity as the pure SE; reasoning for this result is covered in the next section.

Figure 6.4c is short circuit capacity as a function of temperature at the fixed current density

of 0.5 mA cm^{-2}. For the pure SE, incremental increases in amount of capacity passed is apparent. Most likely, this could be from enhanced conductivity in the electrolyte.[236] However, just as with varying current densities, there are significant deviations once polyimine is used. At 30°C, both systems function similarly. At this low temperature, the polyimine has limited malleability. Once temperature is increased, a significant improvement is made in total capacity before short. The SE/polyimine system passes a full 25 mAh cm^{-2} without shorting at 90°C whereas the pure SSE only has a small boost in capacity due to increases in temperatures. Therefore there is an obvious trend in dendrite prevention and polyimine malleability.

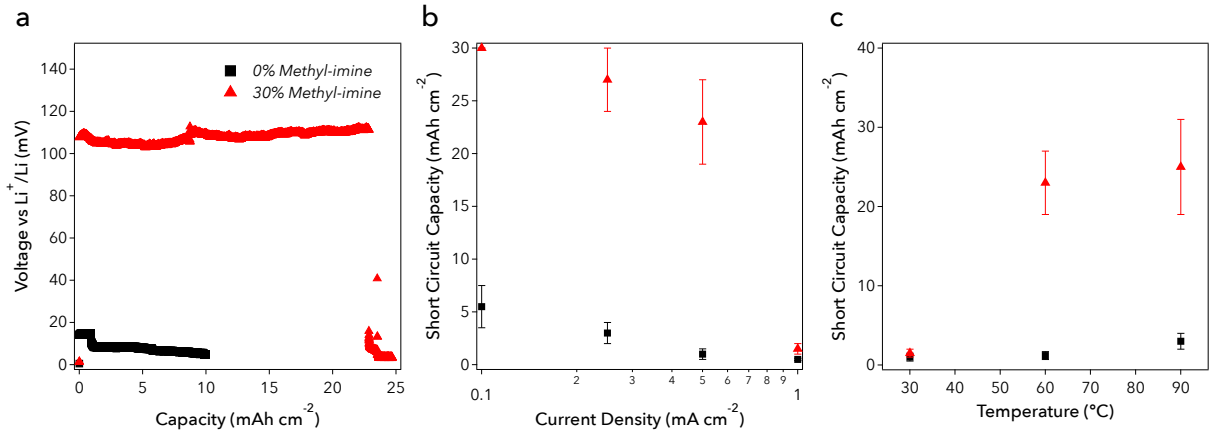

Figure 6.4: Lithium symmetric cells containing a pure SSE separator (0% polyimine) and composite with 30% polyimine, a) Galvanostatic plating of lithium at 0.5 mA cm^{-2} and 60°C, b) Aerial short circuit capacity versus current density at 60°C, c) Aerial short circuit capacity at 0.5 mA cm^{-2} with increasing cell temperature. There is a clear trend with the self-healing ability and amount of charge passed. Higher currents past a threshold will force the polyimine to not contribute to performance. Activating the polyimine with temperature allows for enhanced performance.

In order to rule out the possibility performance improvements are a function of any polymer inclusion, Figure 6.5 looks at the same composite concept except replace the self-healing polyimine polymer with another glassy polymer in polyethylene oxide (PEO). The systems were put through the same galvanostatic polarization as before with a current density of 0.1 mA cm^{-2} at 60°C. The PEO actually acts to worsen system performance compared to pure SE, whereas as previously mentioned, the SE/polyimine does not short at all. Therefore this concept is particular to the self-healing polymer.

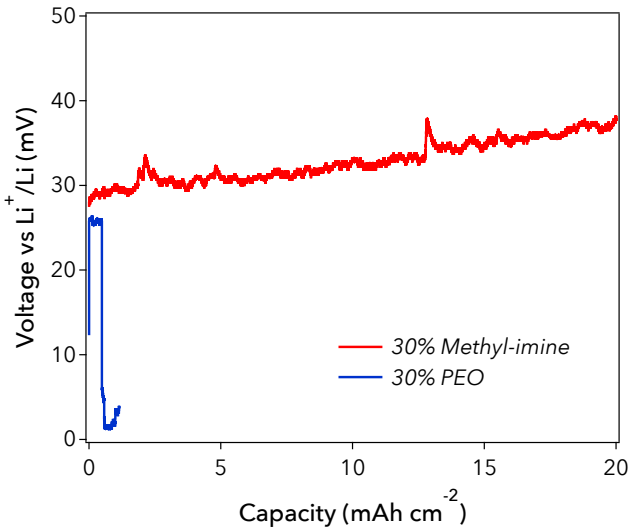

Figure 6.5: The effect of using PEO instead of methyl-imine at the same weight loading during a galvanostatic plating test at 0.1 mA cm^{-2} and 60°C. PEO is above its glass transition temperature at this point. Therefore the polyimine seems to differentiate itself from other malleable polymers.

To test the effect of the polymers inherent strength on its ability to inhibit dendrites, a range of polyimines are used displaying strengths from a classic thermoset (tri-imine) to an elastomer (methyl-imine). These polyimines are detailed in synthesis and characterization in Section 5. Figure 6.6 displays the results of the deposition tests with the various polyimines. Only methyl-imine has a significant impact on performance. Similar to PEO, both tri-imine and hexa-imine do not display an improvement in performance. This could be for a variety of reasons. First, the temperature (60°C) may not be high enough to get tri-imine and hexa-imine significantly self-healing. Second, the performance may not be dependent on the polymers strength. Instead, perhaps a self-healing system with lower energy barrier is in fact more favorable.

After establishing that the best performance occurs with a separator including 30% methyl-imine cold-pressed, the symmetric cell is again constructed but the desired test is a cycling test. A cycling test will flip the current sign after a fixed amount of time or capacity has passed. This test is more similar to the actual charge/discharge conditions in a battery. The cycling test used fixes the capacity at 1 mAh cm^{-2}. Figure 6.7a is the cycling test performed with a pure SSE separator and 30% methyl-imine. The pure separator shorts after 2.5 cycles highlighting the extreme condition

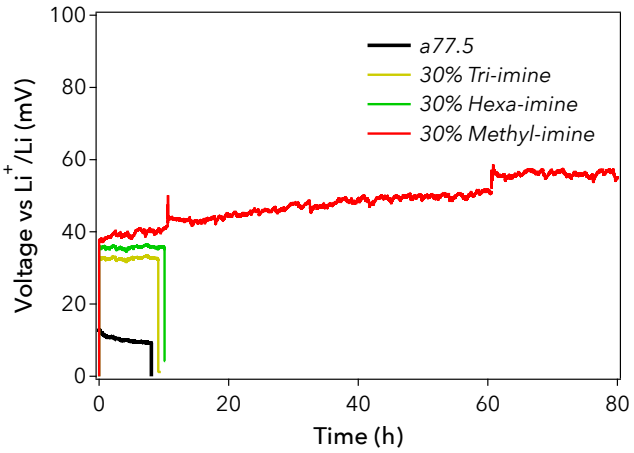

Figure 6.6: Galvanostatic plating of lithium in a symmetric cell using a cold-pressed separators with different variants of polyimine. Only the methyl-imine has a significant impact on performance. Methyl-imine is the most elastomeric, therefore malleability might be key in this design. All tests occur at 0.1 mA cm^{-2} and 60°C. Separators are approximately 500 µm.

dendrites manifest as. The 30% sample cycles for over 50 cycles before short. This is approximately 1 month of cycling time. While this constitutes a dramatic improvement, more design needs to occur to fully develop the result.

Figure 6.7b displays cycling for using the 30% methyl-imine separator at a variety of current densities. Higher current densities of 0.25 mA cm^{-2} and 0.5 mA cm^{-2}, while lasting for a significant amount of time, eventually short after approximately 20 cycles each. It should be noted that a cell using lithium on either side is harsher than a typical battery which has lithium only on a single side.

Figure 6.8 is a schematic of the proposed mechanism in this work. In all these studies, we chose an amorphous solid electrolyte. Since the electrolyte is amorphous, there will be a lack of grain boundaries and therefore lithium metal will grow along the particle boundary of the solid electrolyte. This is markably different than traditional dendrite mechanisms as the solid electrolyte plays a supporting and deposition function. Dendrites traditionally are classified by their growth and formation from lack of concentration gradients on the lithium electrode. As this definition doesn't fully apply to lithium growing through a solid, we title the growths in this system as "inter-particle lithium growth" (IPL) rather than a lithium dendrite. There have been limited studies

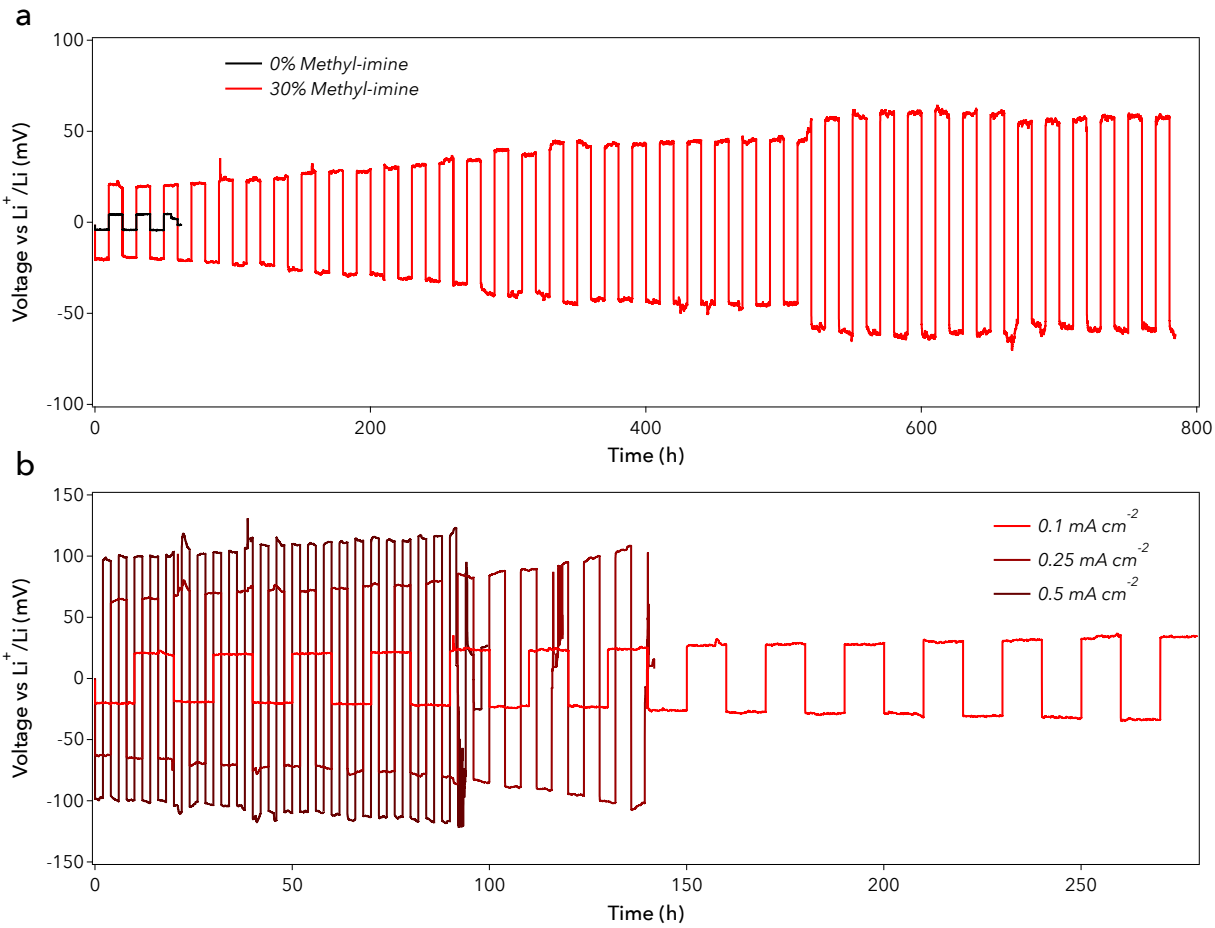

Figure 6.7: a) Cycling test of pure SSE versus 30% methyl-imine at 0.1 mA cm^{-2}, b) Various current densities for cycling of 30% methyl-imine separator. While the pure SSE only lasts for 2.5 cycles, the 30% sample lasts for over 50 cycles. All tests are performed at 60°C.

on IPLs in solid-state and no studies investigating and modeling the IPL formation. We do know though that the motive force for the dendrite tip in liquid is quite strong. Thus we can make this same assumption for the IPL. In a pure SSE separator, there will be pores within the structure (approximately 15% porous). The IPL will force solid electrolyte out of the way into the void space of the separator. The IPL will continue to perform this function until short occurs (Figure 6.4).

The inclusion of self-healing polymer changes the nature of the system on a macroscopic and microscopic scale. Solid electrolyte will still be deformed by the IPL. Any solid electrolyte that acts to compress self-healing polymer will force the polymer to conform to relieve stresses generated in the system. The polymer will grow along particle boundaries until coming into contact with more

polymer and form bonds across the interface, strengthening the interface. Macroscopically, the SE/polyimine system is adaptive. By starting with large domains of polyimine, the system will self-optimize to block IPL growth. Interfaces where polymer meets solid electrolyte will either slow IPL growth or completely block growth all together, the microscopic function of the system.

An adaptive system, one in which the microstructure is actively changing, explains the resistance rise during galvanostatic operation. For all galvanostatic tests in Figure 6.6, the polyimine system increased with resistance over time indicating polymer increasingly dispersing through the structure, impacting SSE/SSE interfaces. The proposed mechanism additionally explains why inclusion of self-healing polymer does not improve system performance at lower temperatures. The system must be significantly self-healing in order to work. The mechanism also correlates current and temperature. With a more self-healing system (more temperature), higher currents will last for longer periods of time. PEO, with no "self-healing" ability, only a glassy function can not perform like the polyimine. PEO cannot relieve stress and is most likely not strong enough to prevent dendrites at polymer/electrolyte interfaces.

6.3 Conclusion

Future work is anticipated beyond the scope of this thesis. The future work is threefold: (1) confirm the mechanism, (2) to improve performance by enhancing processing techniques for producing the membranes, and (3) optimize the system to be used under harsh operating conditions, i.e. $< 30°C$ and > 1 mA cm^{-2}.

1. We plan on performing mechanical measurements of the SE/polyimine composites with varying amounts of polyimine. A transducer will be mounted on top of prepared composites covered in mineral oil, a technique that has been used in other studies. We will also experiment with the possibility of tracking mechanical strength during dendrite growth by stopping IPL growth at different stages and using the transducer method. This would help confirm the movement of the self-healing polymer.

IPL are notoriously hard to detect in the solid-state. They could be anywhere from a micron

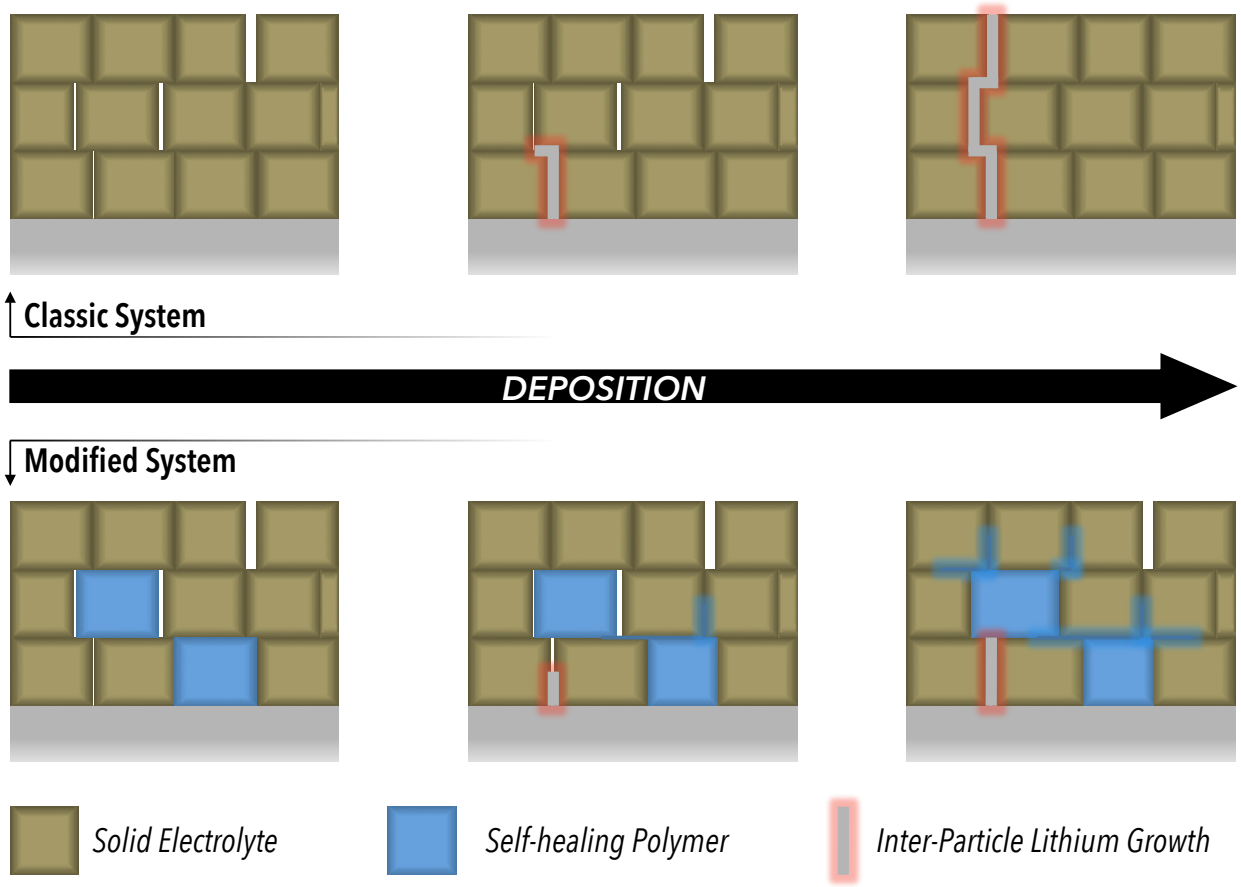

Figure 6.8: Schematic of the proposed mechanism for IPL prevention using polyimine. In a pure SSE system, particles are compacted to form a porous compact. Motive force of the IPL displaces particles and grows along particle boundaries. By inserting a self-healing polymer, any stress applied to the polymer by the electrolyte forces the polyimine to deform along the particle boundaries filling in void space. Therefore the modified system has adaptive interfaces that are constantly conforming to any IPL growth.

to nanometers in diameter and segregated to certain parts of the separator. Therefore, in the absence of detecting IPL growth, we plan on investigating polyimine migration using SEM of cross-sections of the composite at various stages of lithium deposition. SEM and EDS are capable of detecting polyimine by tracking carbon.

2. Currently, polyimine powders are introduced through mixing of solid electrolyte and polymer powders by hand grinding in mortar and pestle. This can lead to heterogeneous mixtures and lack of dispersion. Mixing of powders will be investigated through planetary ball-milling. This will allow for larger batches of composite to be prepared, as well as grinding of polyimine to reduce

particle size, and a more homogeneous dispersion. With smaller particle sizes of the polyimine produced, the overall polymer weight loading in the composite can be reduced which will increase the bulk conductivity.

Another technique to be explored will be similar to the conventional slurry casting performed for batteries. During the synthesis of the polyimine, solid electrolyte powder will be added. Thin membranes can then be cast from the viscous solution. During the drying of the solvent, the polymer will form into domains within the solid electrolyte. Calendaring will then produce dense membranes. Tuning the properties of the slurry will be vital to ensure the lack of polyimine coverage on the solid electrolyte particles.

3. In preliminary results, significant dendrite suppression is only achieved at elevated temperature ($> 30°C$) and lower current densities (< 1 mA cm^{-2}). Both of these thresholds are more desirable design and operation parameters. Therefore, this task will focus on improving performance at both of these conditions. As we demonstrate in Figure 6.4, the ability to prevent IPL is directly related to the rate of self-healing in the polyimine. This is why with higher temperatures, greater rate performance is achieved. Conversely, better performance at lower temperatures can be achieved if the rate of self-healing is sufficiently high at low temperatures. The polyimine can achieve this property if the degree of cross-linking is reduced. Where all preliminary tests use a 55% cross-linked polyimine, reducing this amount significantly improves flow at lower temperatures. Production of low cross-linked polyimine will rely heavily on the ability of cryo-grinding or a slurry coating system as proposed in the previous section. Another method we plan on investigating will be the use of a microstructural formation step of sorts. Significant performance is achieved at lower currents and elevated temperatures currently. If the proposed mechanism is such, then an optimized structure is formed during this period. We plan on forming this desirable structure through a formation step of lower currents at elevated temperatures. Then the cell will be moved to lower temperatures and proceeded to be run faster.

Chapter 7

FeS_2-Imbedded Mixed Conducting Matrix as a Solid Battery Cathode

7.1 Introduction

Numerous designs of all solid batteries have been proposed and developed for superior safety and stability. Whether the construction is the slurry-binder technique,[216,237] deposition,[218,219] or follows the dynamic compaction strategy,[58,173] all bulk designs (non-thin film) differ fundamentally from liquid-based systems. The predominant difference between a conventional Li-ion battery electrode and a solid-state electrode: electrolyte pervasion of empty space. In the solid-state, the electrolyte cannot be added in the final stages to fill in the voids. Instead, solid electrolyte powder must be added directly to the original electrode synthesis, leading to many of the obstacles encountered in solid batteries.

Charge transfer in essence requires the presence of an ionic conductor, electronic conductor, and active material (assuming the active material is a pure insulator). Figure 7.1 displays a schematic of this basic requirement. The conductors act as diffusional pathways for both ions and electrons. Perceptively, charge transfer is limited to the triple point of materials. With a liquid, the triple point is virtually guaranteed, whereas if all phases are solid, the presence of the triple point will be far more infrequent. To ensure greater electrolyte/active material boundaries, solid electrolytes exhibiting ductility are preferential.[238] Unfortunately, obligatory ductility limits the selection of solid electrolytes considerably. Even under high compaction pressures, full density will never be achieved such as permeating an empty space with a liquid. Thus naturally, the total

charge transfer sites are limited. The lack of sites leads to "poor rate capability."

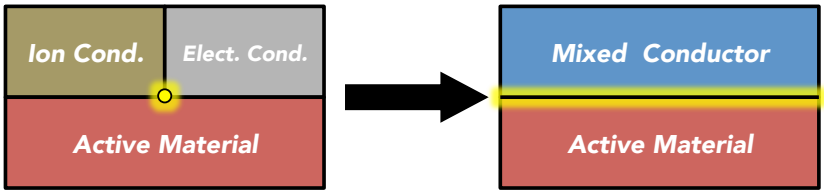

Figure 7.1: Simplification of a standard solid-state electrode design: charge transfer occurs at the triple point between a solid electrolyte, conductive additive, and active material (with the assumption the active material is a pure insulator). This study proposes a new design of replacing both additives with a mixed conductor, enhancing the charge transfer interface.

Active materials naturally exhibit volume expansions and contractions over the course of cycling.[187] In a conventional Li-ion design, the liquid electrolyte can saturate the porous structure and accommodate any expansion without ever losing contact, while a solid will most likely not be able to reform to original conditions. In perspective of Figure 7.1, if one of the conductive additives loses contact with the active material, diffusional pathways are severed and principally transport must take place within the active material, often a strenuous process. This is a common problem in solid designs referred to as "active material isolation."

Finally, the presence of a solid electrolyte powder generates additional variables. Not only can there be chemical instabilities leading to chemical decomposition,[100,198,239] but typically solid electrolytes are difficult to synthesize,[205] and are unstable in most solvents used in battery preparation.[216] Variability in the particle sizes of both active material and solid electrolyte add to "heterogeneity of the electrode design," complicating repeatability.

Therefore, we pose the question: can the solid electrode design be simplified?

This study investigates the effect of replacing both the ionic conductor (solid electrolyte) and electronic conductor (carbon) with a single mixed conductor. By doing so, the theoretical interface for charge transfer is enhanced immensely. Any material contact between active material and mixed conductor will ensure diffusional pathways for both ions and electrons. If the transport of charged particles is high enough, there would be no need for additional electrolyte or carbon.

The concept of pairing a mixed conductor and insulative active material, while not entirely

new, has not been studied in depth.[240,241] Recently, studies using a mixed conductor of TiS_2 with sulfur have been reported;[242] however, the purpose of these studies were to protect the active material from electrolytic attack and dissolution, common problems in liquid batteries yet not applicable to solid-state.[243] Other pairings include CuF_2 with MoO_3 to enhance utilization of the active material.[244] Yet even these systems still used carbon as a conductive additive and no fundamental charge transfer investigations were conducted. To the best of our knowledge, this is the first report of pairing only a mixed conductor with active material excluding both ionic and electronic additives in liquid or solid configuration.

The system we test the hypothetical design on is an active material of FeS_2 and a mixed conductor of $LiTiS_2$. FeS_2 has recently proven to have potential in a solid battery due to its high theoretical capacity (894 mAh g^{-1}),[126] conductive discharge products (iron metal),[245] and tremendous stability.[246] $LiTiS_2$ (LTS) has a diminutive, low-voltage capacity (227 mAh g^{-1}) to be useful singularly;[247] however, LTS is one of the best lithium mixed conductors known with a Li-ion self-diffusion coefficient of approximately 1 x 10^{-9} cm^2 s^{-1} at room temperature[248] and an electronic conductivity in excess of 1 S cm^{-1}.[249] The system is advantageous as the lithiation voltage of TiS_2 is greater than that of orthorhombic FeS_2 (marcasite) and thus can act as a solid electrolyte. The new system is characterized via transmission electron microscopy (TEM) and electron energy loss spectroscopy (EELS) to demonstrate uniform dispersion of nano-FeS_2 in an amorphous LTS matrix. Mass transfer measurements, via electrode diffusion coefficients, indicate high diffusion capabilities at initial stages of lithiation. Charge transfer is measured using a Tafel analysis revealing that the FeS_2-LTS system has over double the exchange current as a standardly prepared solid cathode of the same composition. The result is a hybrid power-energy system where a prominent capacity (567 mAh g^{-1} can be achieved at moderate rates (C/10) and a capacity greater than 400 mAh g^{-1} of electrode can be achieved at high rates of C/2. The new system persists for over 500 cycles, with a 62% capacity retention and 99.8% average coulombic efficiency, and is able to recover near theoretical capacity following rate reduction. Comparison of the new mixed conductor/active material design to a standard solid electrode system demonstrates the stark

contract in minimal active material isolation. The more homogenized electrode design now allows for better repeatability as the cathode composite can be produced at the mass scale.

7.2 Results and Discussion

Work in this section has been presented in the 2016 publication.[250] An important aspect of any cathode is maximal contact between active material and conductors. Therefore, the optimal structure of the proposed design will have nano-domains of active material imbedded in a matrix of the mixed conductor to amplify charge transfer surface area. The continuous mixed conductor matrix will also act as diffusion pathways for both Li ions and electrons. The design is accomplished by concurrently reducing FeS_2 particle size whilst forming an in situ matrix of LTS through planetary ball-milling of FeS_2, TiS_2, and Li_3N. By maintaining a low weight loading of FeS_2, particle agglomeration is prevented and FeS_2 domain size is continually reduced. Other studies have investigated the effects of using a solid dispersant to achieve nano-FeS_2, therefore LTS acts as a solid dispersant in this design.[251]

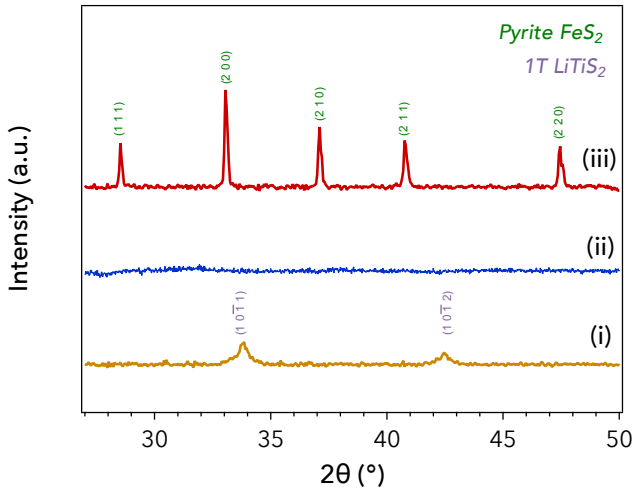

Figure 7.2: XRD pattern of: (i) TiS_2 and Li_3N (3 to 1 molar ratio) ball-milled 2 hours to form crystalline 1*T*-$LiTiS_2$, (ii) TiS_2 and Li_3N (3 to 1 molar ratio) ball-milled 20 hours to form amorphous $LiTiS_2$, (iii) FeS_2, TiS_2, and Li_3N (3.1, 3, 1 molar ratio) ball-milled 20 hours to cathode in study. Only cubic FeS_2 peaks are present demonstrating that amorphous $LiTiS_2$ can also be formed without reacting with FeS_2.

The other important aspect of any electrode is to achieve prominent Li-ion diffusion. LTS

naturally forms in the $1T$ hexagonal layered structure.[247] Although the Li self-diffusion in $1T$-LTS is quite high,[252,253] the material suffers from having highly anisotropic diffusion in two dimensions. We discover an interesting effect and new method to amorphize LTS by ball-milling TiS_2 and Li_3N for extended periods of time. The addition of Li_3N reduces TiS_2 particle size through an in situ lithiation.[124,254] Figure 7.2 is an XRD pattern of the prepared electrode with amorphous LTS, amorphous LTS singularly, and $1T$-LTS. The method for preparing $1T$-LTS was previously reported.[254] It is concluded that LTS is amorphous due to the lack of XRD peaks. The FeS_2-LTS cathode in Figure 7.2iii does not contain the crystalline LTS peaks at 33.5° and 42°. Thus, LTS can still amorphize even with inclusion of FeS_2 during the milling process. We are aware of only one study that has been able to achieve an amorphous LTS; both theoretically and experimentally, three dimensional diffusion was achieved.[255] Having a more isotropic diffusion without preferential pathways will enhance the active material/mixed conductor interface. As FeS_2 retains cubic peaks after milling with the other precursors, it would appear that FeS_2 does not chemically interact with Li_3N or TiS_2. An explanation for this behavior is derived from investigating the theoretical solid-state reaction enthalpies, as computed by the Materials Project,[256] and displayed as Equation 7.1 and 7.2

$$6TiS_2 + 2Li_3N \rightarrow 6LiTiS_2 + N_2 \qquad \Delta H = -734kJmol^{-1} \tag{7.1}$$

$$3FeS_2 + 2Li_3N \rightarrow 3Li_2FeS_2 + N_2 \qquad \Delta H = -488kJmol^{-1} \tag{7.2}$$

While not definitive, this gives an indication that the reaction of Li_3N with TiS_2 is more spontaneous and favorable. Additionally, TiS_2 has diffusion pathways to accommodate lithium. Cubic FeS_2 is known to have a strong activation energy during initial lithiation which helps explain the role of Li_3N.[126]

The theoretical structure of the solid cathode is confirmed using TEM (Figure 7.3). Using an FIB mill to cross-section the uncycled and 10th cycle electrode,[182] the compacted structure is revealed a more accurate representation of performance than free-formed powders. Intial FeS_2

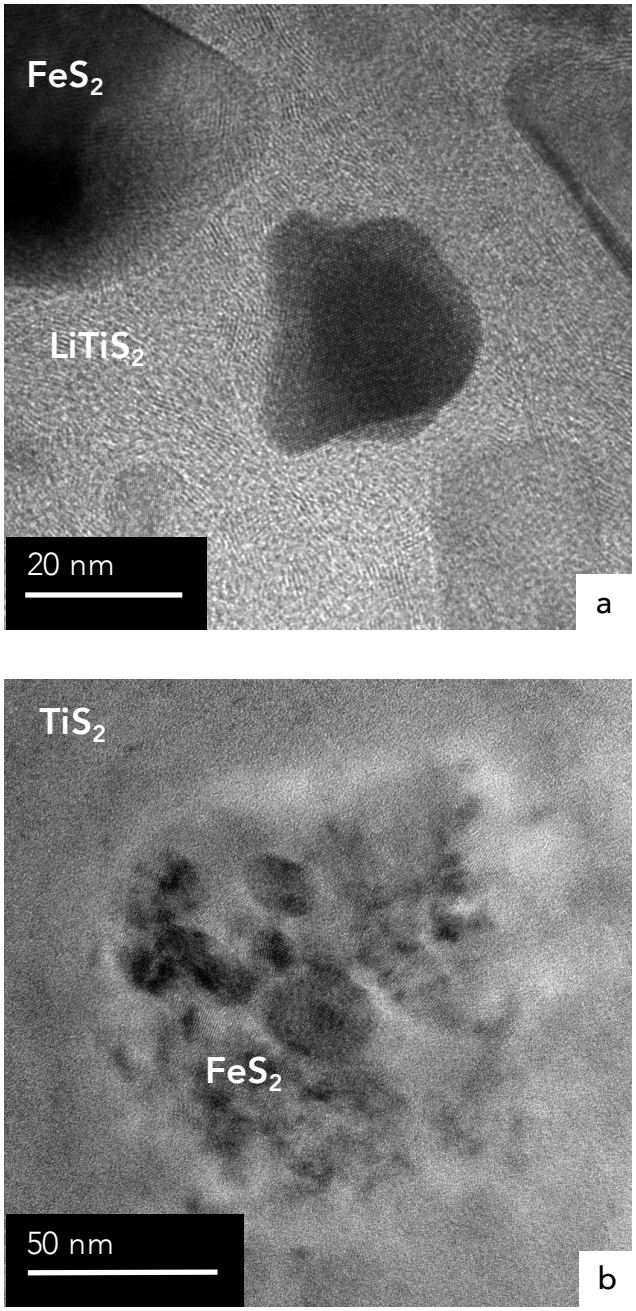

Figure 7.3: a) HR-TEM of interface between amorphous $LiTiS_2$ matrix and FeS_2 nano-domains in uncycled electrode, b) 10th cycle charge HR-TEM of interface between amorphous TiS_2 and FeS_2. FeS_2 has pulverized into nano-domains that remain clustered. Intimate contact is preserved between mixed conductor and active material.

domains are detected on the order of 10-100 nm in Figure 7.3a. The LTS matrix appears to have disordered domains on the order of a nanometer. The size of these domains would correspond to only a few TiS_2 slabs. While not truly amorphous, the severe disordering on this length scale

would contribute to three-dimensional diffusion. Therefore references to amorphous LTS in this text refer to the x-ray amorphous property. Intimate contact is developed between LTS and FeS_2. To understand the microstructural changes that occur during cycling, a cross-section of the 10th cycle FeS_2-LTS electrode following full charge to 3 V is investigated by HR-TEM in Figure 7.3b. The large FeS_2 particles pulverize into smaller domains yet remain clustered together. This is in accord with previous studies that only reported this behavior after the first charge.[126] The TiS_2 matrix now appears to be completely amorphous yet remains in excellent contact with the pulverized FeS_2.

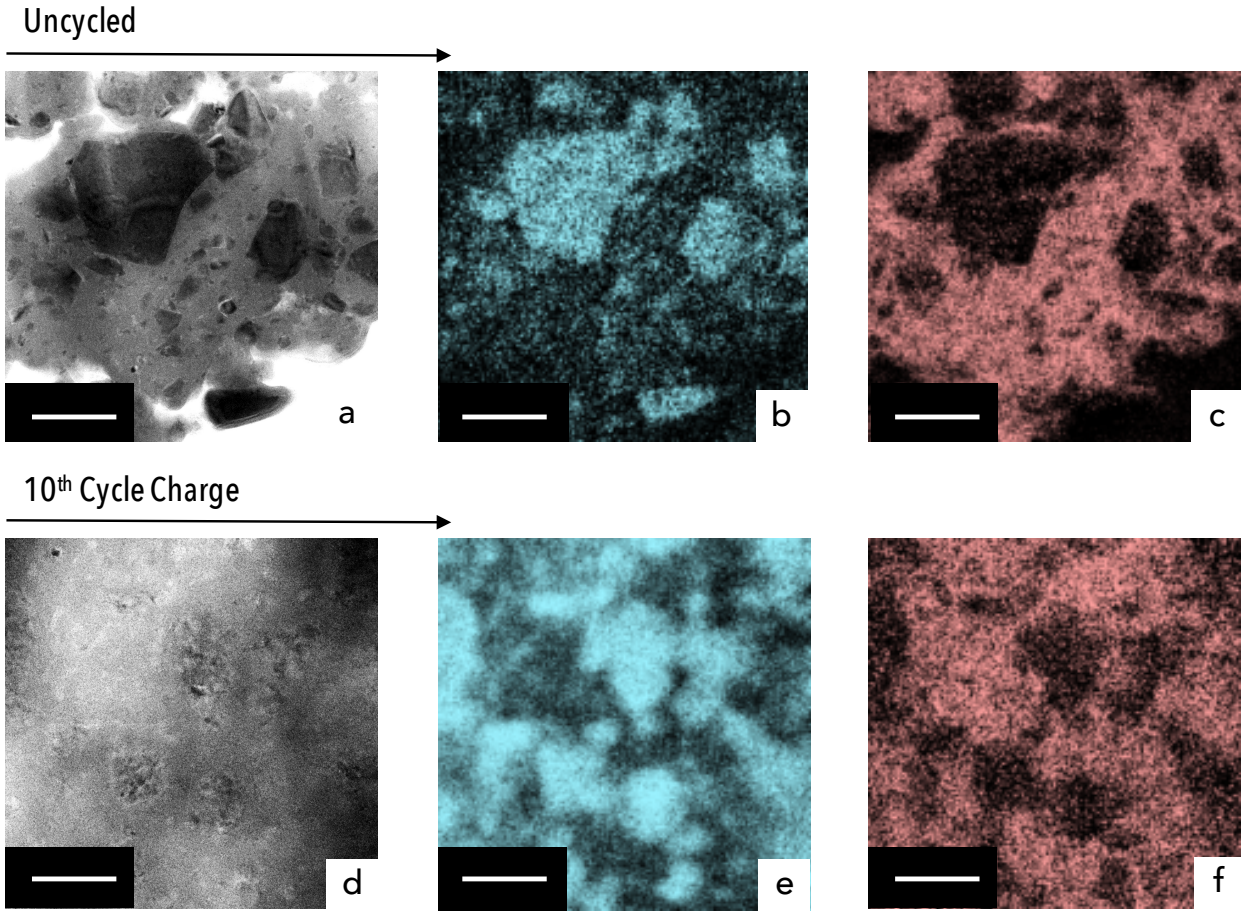

Figure 7.4: a) TEM of FeS_2 (dark) imbedded in LTS (grey) matrix, b) zero loss elemental mapping of iron in uncycled electrode, c) zero loss elemental mapping of titanium in uncycled electrode. It is clear that FeS_2 and LTS remain separated and not chemically mixed. d) TEM of 10th cycle charge cross-section, e) zero loss elemental mapping of iron, f) zero loss elemental mapping of titanium. Whilst FeS_2 has agglomerated into larger domain sizes over cycling, the LTS matrix remains in contact without any indication of a chemical decomposition.

TEM and EELS elemental mapping of iron and titanium in the uncycled electrode is displayed in Figure 7.4a, 7.4b, and 7.4c, respectively. Due to partial oxidation, it is impossible to confirm an exact 2 to 1 sulfur to iron or sulfur to titanium in both active material and matrix. XRD in Figure 7.2 along with the distinct domains of FeS_2 would suggest no chemical interaction occurs between FeS_2 and TiS_2 in the prepared state. This is an added benefit of not using solid electrolyte as solid electrolytes can decompose against active materials or even low voltage mixed conductors.[51,239] EELS elemental mapping is again used to probe iron and titanium following the 10th cycle charge in Figures 7.4e and 7.4f, respectively. There is a stronger iron signal in this case that could be due to the pulverization of particles. The two materials are still somewhat separated but the FeS_2 appears to form a more continuous matrix rather than localized clusters. Two matrices in contact with one another is still an ideal structure in the solid-state for performance.[173] While a definitive statement cannot be made that chemical interaction is not occurring, due to the electrochemical response during cycling in the upcoming section, it appears that neither the lithiation of FeS_2 nor conduction capabilities of TiS_2 are being hindered. Inference of replacing a metastable solid electrolyte with a thermodynamically stable TiS_2 would suggest less chemical decomposition is expected.

Figure 7.5 displays the basic electrochemical properties via cyclic voltammetry (CV) of the FeS_2-LTS cathode against a standard cathode using FeS_2, solid electrolyte, and carbon. The standard cathode is investigated for the rest of this study to provide a stark contrast with the new design. Figure 7.5a and 7.5b are CVs of the FeS_2-LTS and standard systems at various sweep rates, respectively. All values are normalized per gram of composite to make accurate comparisons between the two electrodes. The most noticeable difference is the shape of the first cathodic peak with increased sweep rates. Since the cathodic peak potential shift is much larger than the corresponding anodic peak potential shift, it can be inferred this is due to a significant activation overpotential in the standard system compared to the FeS_2-LTS system.[257] This will be explored more in the upcoming sections. For the other main cathodic peak and two main anodic peaks, there is not a substantial difference in peak potential; this is further displayed in Figure 7.5c

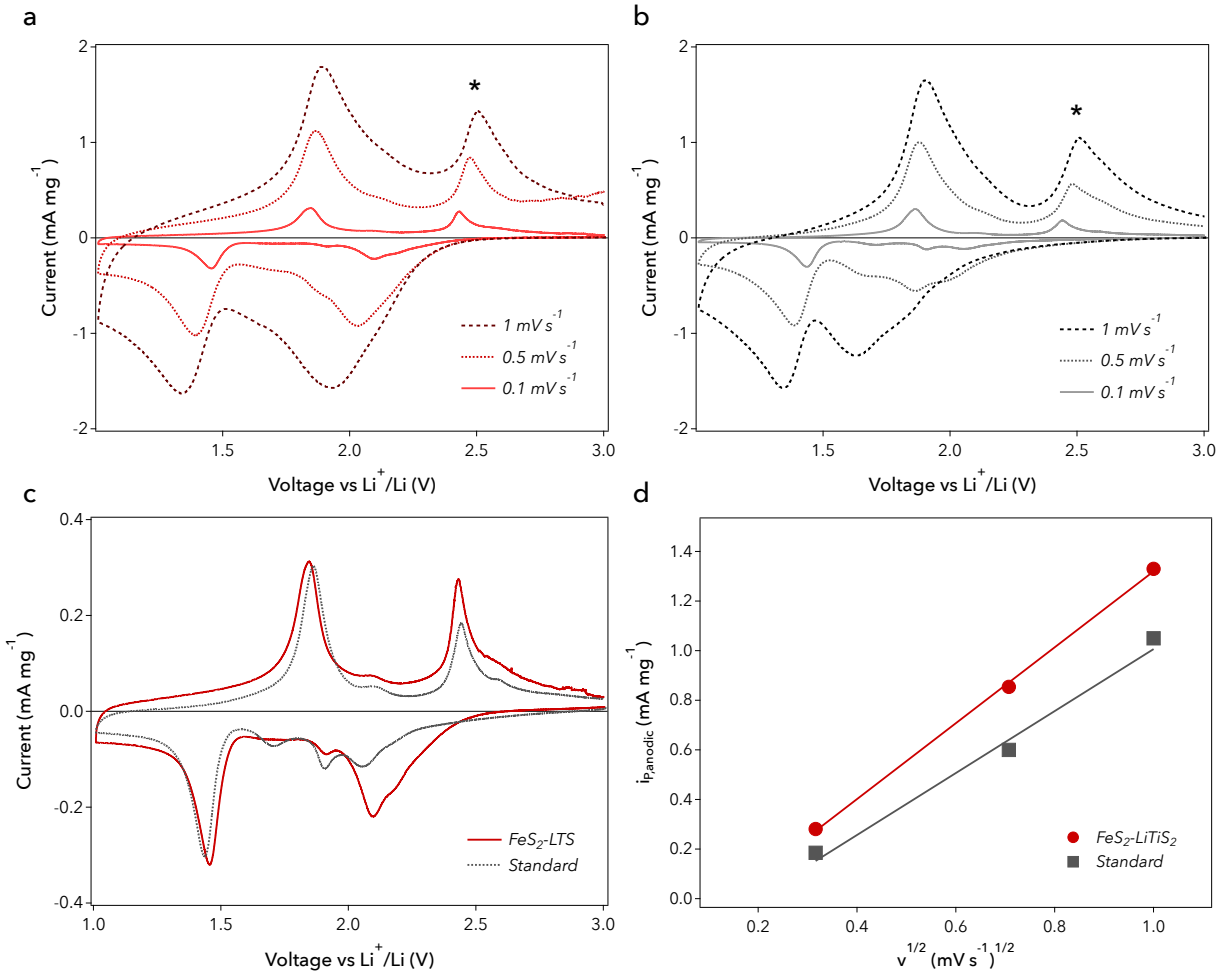

Figure 7.5: a) CVs at various sweep rates for the FeS_2-LTS system. Asterisk denotes anodic peak for analysis in (d). b) CVs at various sweep rates for standard system. Clearly there is a large voltage shift in the first cathodic peak for higher sweep rates. This remains in stark contrast to the FeS_2-LTS system and highlights the advantage of LTS. c) Overlap of 0.1 mV s^{-1} sweep rates for the two systems, d) Peak current of second anodic peak (asterisk) versus square root of the sweep rate for the two systems.

which overlaps the slow sweep rate of 0.1 mV s^{-1} for both systems. An asterisk is used in Figure 7.5a and 7.5b to denote the anodic peak used for analysis. Figure 7.5d plots the peak current of the second anodic peak for both systems versus the square root of the sweep rate. The steeper slope of the FeS_2-LTS system indicates either a larger diffusion coefficient or greater lithium ion concentration.[257] Due to the fact that the same active material is being used and greater lithium ion concentration in the solid electrolyte than in the TiS_2 matrix, the difference is most likely due

to the larger diffusion coefficient now explored more directly.

To analyze mass transfer polarization, the most important term will be Li ion self-diffusion (D_{Li}) apparent in Ficks second law. We analyze D_{Li} by means of the galvanostatic intermittent titration technique (GITT) developed by Weppner and Huggins[258] and furthered by Wen et al.[259] This technique applies a current pulse to the system and measures the relaxation voltage. The calculation is given by Equation 7.3

$$D_{Li} = \frac{4}{\pi\tau} L^2 \left(\frac{\Delta E_s}{\Delta E_t} \right)^2 \qquad t << \frac{L^2}{D} \tag{7.3}$$

Where τ is the time of the current pulse, L is the length of the electrode, ΔE_s is the change in steady-state voltage as a result of the current pulse, and ΔE_t is the total change in voltage during the application of constant current (subtracting out uncompensated ohmic effects).[258]

The diffusion coefficient will vary as a function of lithium content in the electrode; therefore D_{Li} is measured over the course of a full discharge and charge. The third cycle is chosen to obtain relevant values due to allotropic transformation in FeS_2 from cubic to orthorhombic during the first cycle.[123,126,260] Figure 7.6a and 7.6b plots the diffusion coefficient as a function of voltage over the 3rd cycle for the FeS_2-LTS and standard systems, respectively. Obtained values are in agreement to the only other study for determining D_{Li} in Li_xFeS_2.[261] As the reduction of the $(S-S)_2^{2-}$ persulfide units in marcasite proceed, a minimum in D_{Li} is present. Lack of diffusion pathways and vast structural changes lead to this occurrence. A maximum in D_{Li} is achieved once the layered γ-phase of Li_xFeS_2 is formed and continues for the full intercalation region up to Li_2FeS_2 is formed, whereby the persulfide units are fully reduced to S^{2-} anions.[261,262] A local minimum is again achieved during the redox of Fe^{2+} to Fe^0. While there are no studies investigating diffusion in this region, we postulate a low coefficient is the direct result of a two-phase formation as well as creation of resistive Li_2S. Evidently, there is scarcely a difference in D_{Li} between the two systems; however, there is a dramatic change during initial stages of lithiation. In the first few pulses of current in the FeS_2-LTS cathode, only the TiS_2 is lithiating due to the higher lithiation voltage. LTS has an extraordinarily

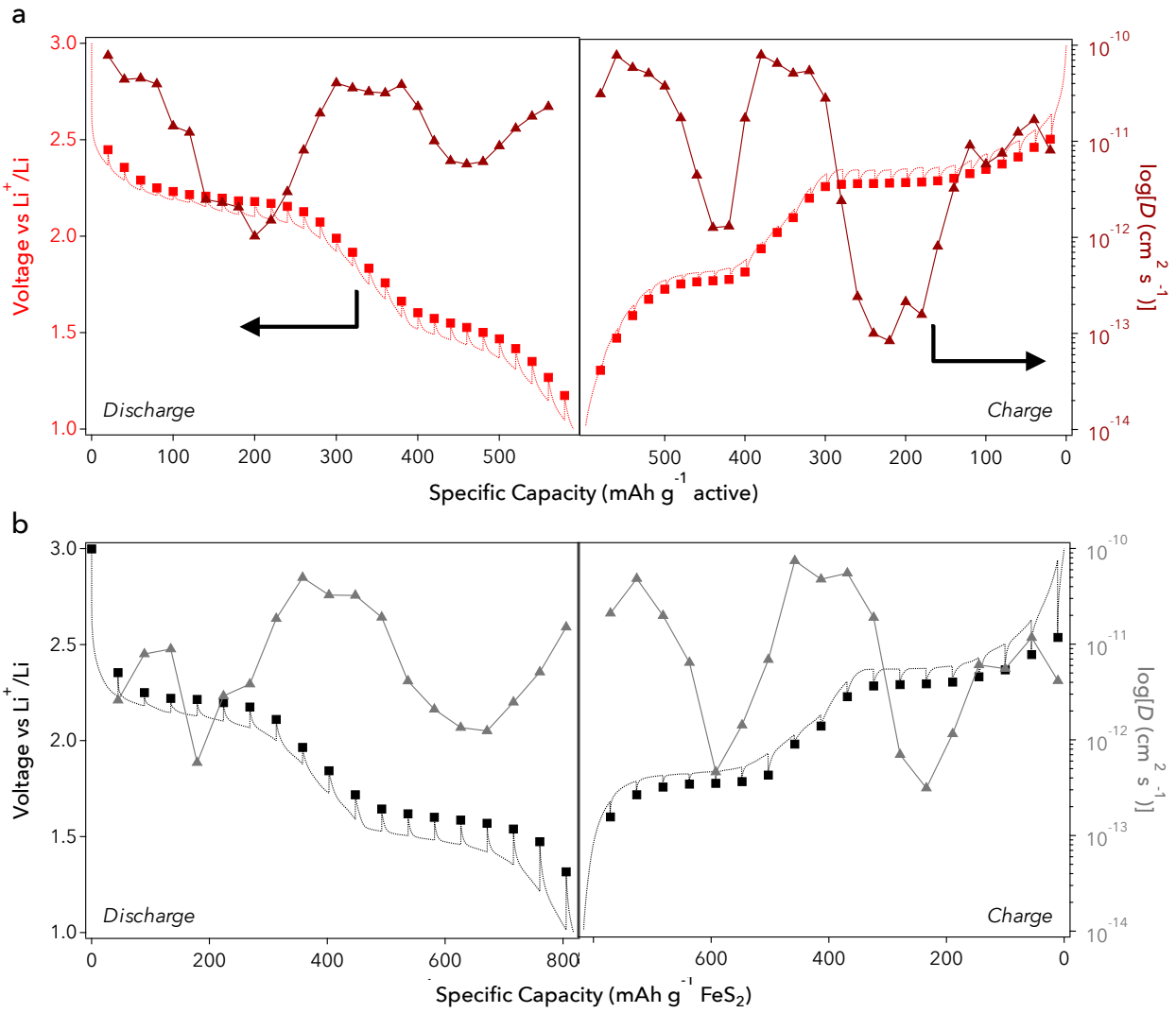

Figure 7.6: a) GITT of FeS_2-LTS system over 3rd discharge and 3rd charge, b) GITT of FeS_2 standard system over 3rd discharge and 3rd charge. C/20 current pulses are used for 1-hour increments followed by a 6-hour relaxation. Both tests are at 60°C. (Squares) are relaxed voltages, (triangles) are calculated diffusion coefficients. While both tests yield relatively same diffusion coefficients, they differ significantly at initial lithiation as only LTS is utilized during these stages.

high value of D_{Li}, even higher than many sulfide solid electrolytes.[196,248,263] This process is not apparent on delithiation as the delithiation voltage of FeS_2 and TiS_2 almost overlap. Interestingly, mass transfer is not significantly affected by removing the solid electrolyte. An attempt was made to measure the ionic conductivity directly of the electrodes using DC polarization, however, due to conflicting ionic/electron flow,[264] these values were indeterminate.

Perhaps the most important polarization impacting system performance for this design is charge transfer, as previously discussed. In order to measure charge transfer, a Tafel analysis is used.[265] While this technique may appear unconventional, more common techniques such as Electrochemical Impedance Spectroscopy is severely impacted from poor interfaces such as those found in solid-state.[100,168] Additionally, Tafel analyzes have been used on a variety of cathode and anode materials.[266–269] A Tafel analysis measures exchange current (i_0) representative of a balanced faradaic activity at equilibrium and is therefore relatable to the reaction rate and contributing factors. Equation 7.4 is the cathodic Tafel equation:

$$\eta = \frac{RT}{\alpha F} ln i_0 - \frac{RT}{\alpha F} ln i \tag{7.4}$$

Where η is the polarization, R is the gas constant, T is the temperature, α is the charge transfer coefficient, and F is Faradays constant.[257]

By polarizing a system far enough from equilibrium, the forward or backward reaction will dominate. Extrapolating the linear segment back to equilibrium yields the exchange current. Using linear sweeps in both the upper plateau (intercalation) and lower plateau (conversion) on the 3rd cycle for each system, rearrangement yields overpotential as a function of current. Figure 7.7a gives the Tafel plot of both systems at 60°C. Appropriate Tafel behavior is observed. Due to the reversibility of the system, we replot the measurements in an Allen-Hickling plot in Figure 7.7b. Allen-Hickling proposed a rearrangement of the Butler-Volmer equation (Equation 7.5) which ignores the reverse reaction as to isolate the forward reaction.[270]

$$ln\left[i_0/(1 - e^{\frac{F\eta}{RT}})\right] = ln i_0 - \frac{\alpha F}{RT}\eta \tag{7.5}$$

From the y-axis intercept in Figure 7.7b, the exchange current is determined and displayed in Table 7.1. Normalized charge transfer resistance is calculated using the following relationship,

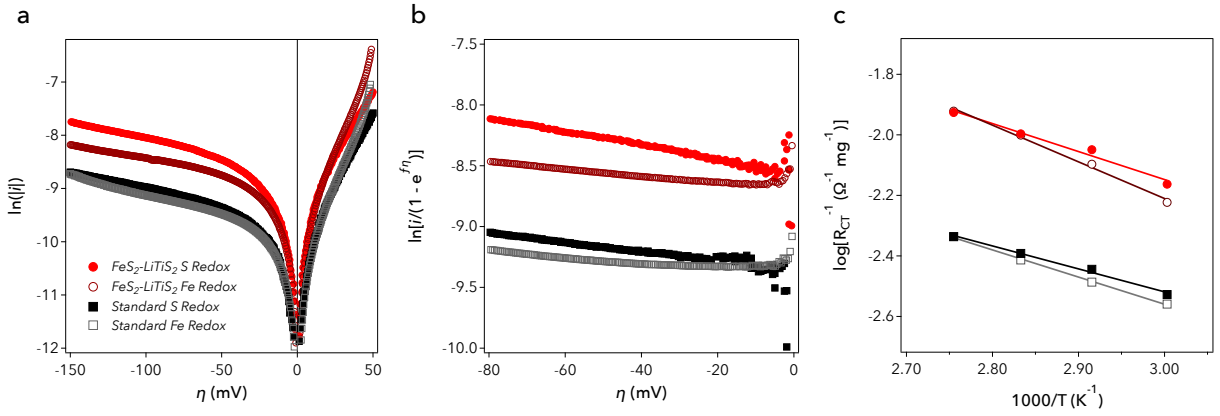

Figure 7.7: a) Tafel plot of both FeS_2-LTS and standard systems during lithiation in the S redox plateau (intercalation) and Fe redox (conversion), b) Allen-Hickling plot with intercepts on vertical axis yielding exchange current, c) Exchange current as a function of temperature. Vastly superior charge transfer is exhibited in the FeS_2-LTS system. Computed resistances are in Table 1.

whilst additionally dividing by the mass of the electrode:[265]

$$R_{CT} = \frac{RT}{Fi_0} \tag{7.6}$$

In Figure 7.7b, the relative measurements between the two systems have similar slopes; this outcome is expected as this represents the FeS_2 reaction barrier and should be analogous for both systems. To the best of our knowledge, we have not found any Tafel analyses performed on an FeS_2 material or a conversion material for that matter. However, exchange currents have been measured between a solid electrolyte and metallic interface.[266,267] These reported exchange currents are higher than what is measured in this study, but rationalized due to known facile kinetics for metallic stripping and deposition. Exchange currents measured for the intercalation cathode material, $LiFePO_4$ is very similar to this study however.[269]

Exchange current and thus charge transfer resistance measurements were taken for temperatures between 60-90°C and plotted in Figure 7.7c. Plots using an Arrhenius relationship between temperature and inverse resistance has been used previously to extract a charge transfer activation energy.[271,272] Tabulated activation energies are displayed in Table 7.1. In Table 7.1, the most drastic difference between the two systems is that the FeS_2-LTS system is over half as resistive as

Table 7.1: Results of Tafel Analysis on FeS_2-LTS and standard systems. Exchange current at 60°C, charge transfer resistance, and charge transfer activation energy are tabulated.

	$i_{0,60°C}$ [mA mg^{-1}]	R_{CT} [Ω mg^{-1}]	E_a [eV $atom^{-1}$]
FeS2-LTS Intercalation	0.197	145	25.0
FeS2-LTS Conversion	0.162	172	30.7
Standard Intercalation	0.085	367	18.0
Standard Conversion	0.079	427	20.7

the standard system. In both cases, the charge transfer resistance is more profound for the conversion region of the system. The conversion region generally demonstrates more sluggish kinetics than the intercalation portion and therefore should decrease the exchange current. Although the precise reason for the smaller charge transfer resistance in the FeS_2-LTS is difficult to specifically assign, we postulate that this is due to the enhanced contact area for charge transfer to occur. And as indicated by Figure 7.3, the FeS_2 is almost completely encapsulated in LTS promoting near theoretical charge transfer whereas the standard system will not be able to achieve this connection. The charge transfer activation energies are greater for the conversion regions as compared to the intercalation region. It should be noted that the experimentally derived activation energies are quite a bit smaller than those measured for liquid systems.[266,271] In a solid system, there is no solvation and desolvation of the ion, nor specific adsorption. Thus a smaller energy barrier is incurred and charge transfer resistance is much less than a solvated interface, chronicling the benefits of solid-solid interfaces.[272] High charge transfer resistance in the standard system at end of lithiation could be attributed to differences in concentration gradients developed in LTS versus the solid electrolyte. Future work will have to be pursued in a thin film format, where near theoretical interfaces can be formed and more accurate measurements of charge transfer can occur.[273]

Figure 7.8a is a rate study of the FeS_2-LTS and standard systems. Rate is symmetrically increased every 3 cycles from C/10 to 4C with C/10 recovery cycles allowed between rate changes. Corresponding voltage profiles are displayed in Figure 7.8c and 7.8d along with differential capacity plots for the FeS_2-LTS and standard systems, respectively. The FeS_2-LTS cathode achieves near

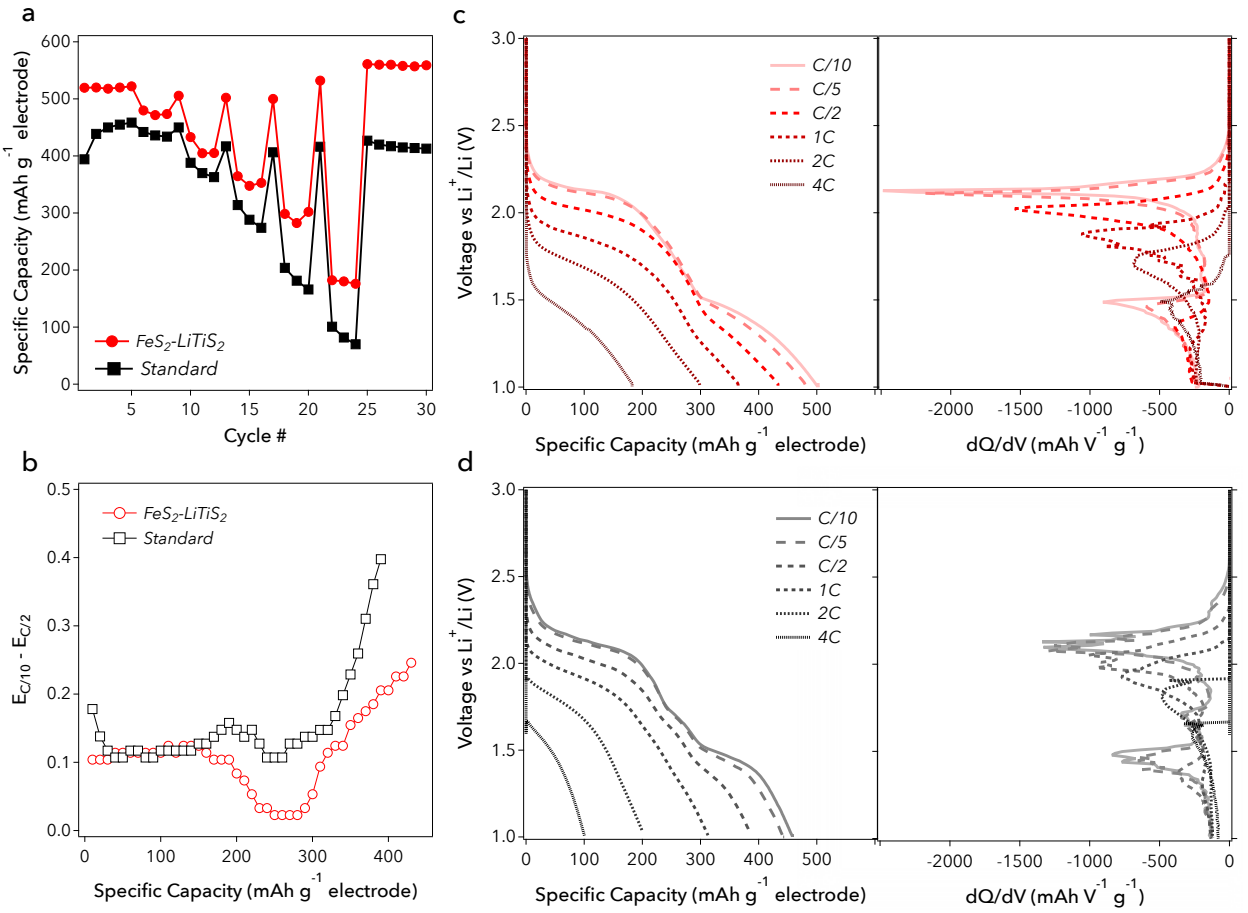

Figure 7.8: a) Rate study of FeS_2-LTS and standard systems. FeS_2-LTS achieves theoretical capacity at a C/10 rate. The system also shows high stability at extreme rates whereas the standard system shows poor stability at rates greater than C/5. b) Polarization of C/2 with respect to C/10 voltage profiles for both systems. The standard system has a greater ohmic polarization at low capacities and charge transfer polarization at high capacities. c) Discharge voltage profiles of the FeS_2-LTS system with respective dQ/dV values on the right-hand side. Not only sharp plateaus are seen at all rates, but the Fe redox plateau (lower) is present even at a 2C rate. d) Discharge voltage profiles of the FeS_2 standard system with respective dQ/dV values on the right-hand side. Fe redox plateau disappears at rates greater than C/2.

theoretical capacity (567 mAh g^{-1} electrode) at a rate of C/10. Additionally, no electrolyte activation is noticeable in the LTS system, whereas in the standard system, it has been well documented that electrolyte activation adds additional capacity manifesting in a gradual capacity increase.[272] The LTS system achieves greater capacity with better stability at higher rates - the voltage profiles provide evidence for why this is possible. At higher rates, the superior diffusion coefficient in LTS acts to "absorb" much of the current shock to the system, expressed in a smoothing effect

at immediate application of current. In the standard system, a sharp ohmic drop is perceived followed by a recovery. The smoothing effect is a product or both the lower activation overpotential (as probed by CV) and higher diffusion coefficient (from GITT). Larger capacities arise from the presence of the iron redox (conversion) reaction even at higher rates. The conversion plateau is present in the LTS system even at a rate of 2C. Lower charge transfer resistance exhibited in this region, as detailed in the Tafel analysis, provides evidence for how this is possible. One way to visualize the drastic differences between the two systems is to subtract out the C/2 voltage profile from the C/10 voltage profile for each system. This is displayed in Figure 7.8b. In doing so, the relative polarization between high and low rates is observed. The LTS system has a smaller ohmic overpotential (initial capacity) and despite having a small overpotential during the sulfur redox (intercalation) region, full utilization actually occurs as the overpotential drops to zero. Finally, only a gradual rise in polarization occurs at the final stages of lithiation in the LTS system due to a smaller charge transfer resistance. Contrastingly, the standard system has a steep tail at final stages of lithiation due to a greater charge transfer resistance.

Long-term cycling of the two systems at a high rate of C/2 is presented in Figure 7.9a. The standard system undergoes a rapid capacity fade, common to the FeS_2 active material and is attributed to discharge product isolation and poor recombination.[258,264,272,273] The FeS_2-LTS system, on the other hand, is able to maintain 62% capacity over 500 cycles an unprecedented value for a solid-state, high capacity electrode at high rates. Figures 7.9b and 7.9c are the evolving voltage profiles of the FeS_2-LTS and standard systems, respectively. The LTS system maintains the conversion region throughout the course of cycling. The standard system loses the lower plateau and then gradually loses capacity from the upper plateau. This results from active material isolation of FeS_2 due to electrode heterogeneity, implicating that FeS_2 cannot reform upon charging and the majority of retainable capacity transitions to a sulfur active material.[272] The delithiation profile of the FeS_2-LTS system regains a higher proportion of capacity during the 3 V hold than the standard system a behavior explained by results in Figure 7.6. The diffusion coefficient is the same on the charging cycles as the FeS_2 delithiation voltage shifts to higher potentials than the delithiation of

TiS_2. Thus, higher voltages are necessary to completely delithiate the system.

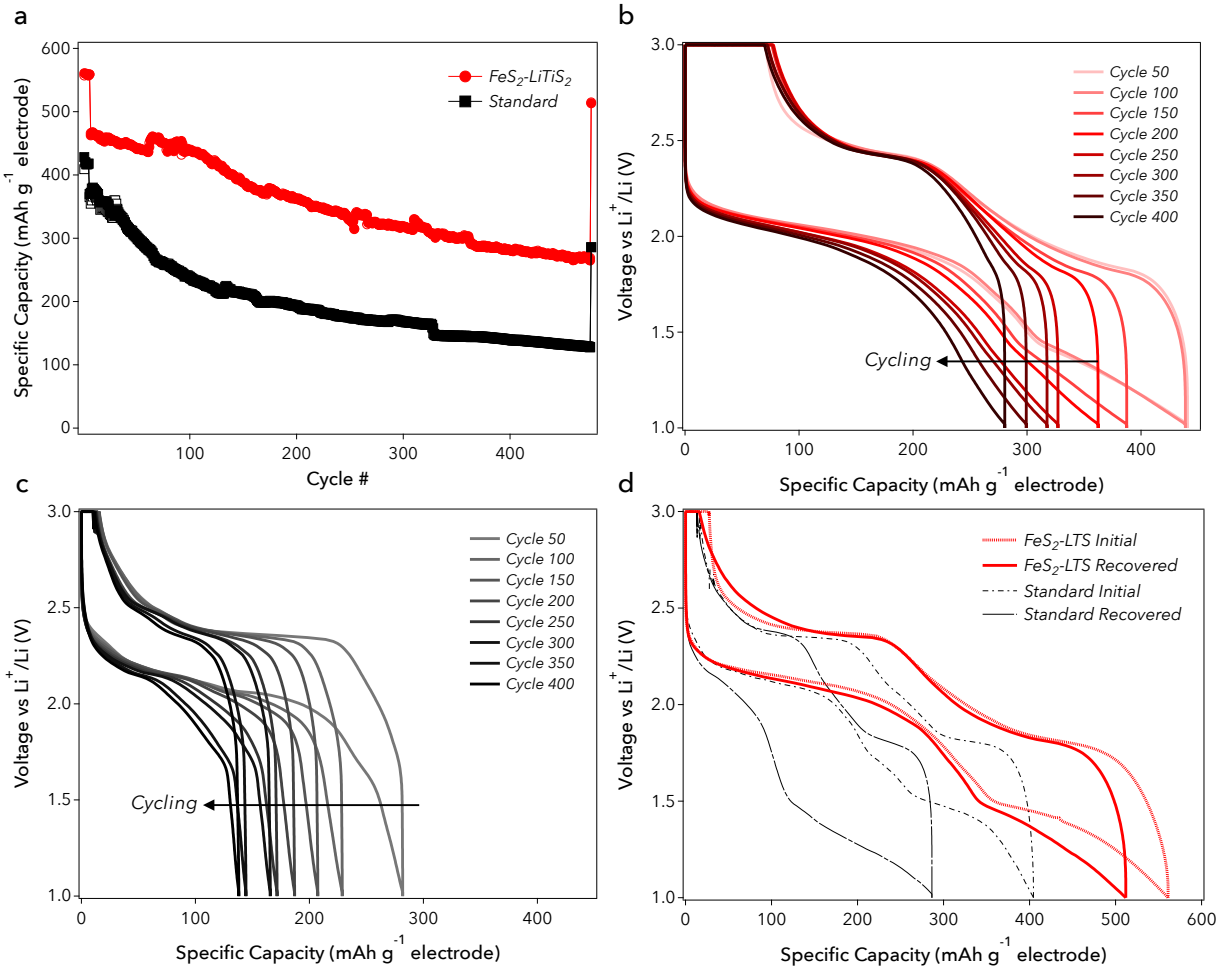

Figure 7.9: a) Cycling at C/2 (1.05 mA cm^{-2}) for FeS_2-LTS and standard cathodes, b) Voltage profiles for FeS_2-LTS electrode over cycling, c) Voltage profiles for standard electrode over cycling, d) 5th cycle C/10 voltage profiles and recovered cycle at C/10 following long-term cycling at C/2 for both electrodes.

One of the most interesting aspect of this new electrode design is the ability to recover capacity. Since active material isolation does not occur, as well as the lack of any chemical decompositions, once the FeS_2-LTS system is slowed back down to C/10 after 500 cycles (Figure 7.9d), nearly all capacity is regained. The standard system can only recover a small portion of this capacity. The ability to recover capacity is of monumental impact. Essentially, this gives the possibility of a "recyclable" battery in the sense that simply by slowing down the system, an original electrode design can be recovered. This will be studied in the future as this possibility could

provide a paradigm shift in discovering significantly more sustainable batteries.

7.3 Conclusion

In this study, we present a new solid-state electrode design. By using a mixed-conducting matrix, it is possible to remove the solid electrolyte and conductive additive yielding many benefits. The combination of FeS_2 and $LiTiS_2$ has the capabilities of both a high power and high-energy system. The $LiTiS_2$ provides high diffusivity during initial stages of lithiation. Charge transfer is greatly enhanced moving from a three material interface to a two material interface. Through a Tafel analysis, the exchange current of the system was shown to effectively double. By developing a possible solution to active material isolation and creating a more homogeneous electrode design, cycling at a high rate of C/2 for 500 cycles is attainable. Additionally, the electrode can recover full capacity simply by reducing system rate. Capacity recovery implicates a lack of active material isolation, a common problem in solid-state batteries.

Chapter 8

Surface Pseudocapacitive Charge Storage in Disordered $LiTiS_2$ at Solid-Solid Interfaces

8.1 Introduction

Pseudocapacitive materials offer an opportunity to bridge the energy storage gap between supercapacitor and battery technologies.[274] Exhibiting reversible faradaic charge transfer, pseudocapacitive materials have the kinetics of electrochemical double layer capacitors with enhanced charge storage due ionic interactions with the material structure.[275] Three possible mechanisms have been defined (surface, intercalation, and underpotential deposition) with a variety of materials having been introduced, most notably metal oxides for supercapacitor applications: RuO_2, MnO_2, NiO, Co_3O_4, TiO_2, Nb_2O_5, Ta_2O_5.[276–284] Yet, pseudocapacitance has only been demonstrated at a solid/liquid interface. A liquid electrolyte has been seen as essential for reversibility, in particular for delivering ions with high velocities and accessing all possible storage sites. Batteries based on solid ceramic electrolytes are widely considered a possibility for next generation energy storage.[24] Benefits such as non-flammability, reduced solid electrolyte interphase (SEI) development, active material confinement, and unity transference number, make the possibilities of the solid-state device extremely appealing.[127] Pseudocapacitance has never been explored if possible in the solid-state (with the absence of a liquid electrolyte). Studies have observed pseudocapacitance with a polymer electrolyte, however, these typically require the use a plasticizer bending the title of solid-state.[13,285]

The combinatorial obligations of an adequate material and compatible system limit the possible selection when searching for an active material to use in a solid ceramic cell. Redox charge transfer within the solid-state is often limited due to interfacing issues between solid electrolytes/active materials/conductive additive or providing atomic scale interfaces between solid electrolyte and active material.[250] For extremely fast and reversible redox charge transfer, such as in pseudocapacitance, to occur in solid-state, the active material would most likely need to be a mixed conductor to ensure diffusion pathways for ions and electrons are preserved. There has only been one study that demonstrates electrochemical double layer capacitance using a solid ceramic configuration, however capacitance values are extremely low in this case but increased by developing a more robust interface between electrolyte and carbon.[286]

Transition metal dichalcogenides (TMD) are a well known class of material to have high lithium diffusivity and decent electrical conductivity.[287] TiS_2 exhibits the greatest mixed conductivity of all the possibilities.[288,289] Since its presentation in 1976, TiS_2 was proposed as a battery and model material. However, the main drawback is the low voltage and small theoretical capacity of 240 mAh g^{-1} equating to a full mole of intercalated lithium.[253] Other TMDs have received a significant amount of attention such as MoS_2 and WS_2 due to production of these materials atomically thin.[290] Recently, pseudocapacitance was discovered in atomically thin MoS_2.[291] Following, pseudocapacitance was demonstrated in increasingly nano TiS_2 sheets.[292,293] TiS_2 is a semi metal so long as more than a single slab is present[294] whereas atomically thin MoS_2 needs to be stabilized in the correct phase or hydrogenated to obtain high levels of conductivity.[295] We have found that due to the advantageous properties of TiS_2, it can operate as a solid-state battery cathode without the use of any electrolyte. Herein, we investigate pseudocapacitance effects of atomically thin and disordered TiS_2 taking place within the structure in the absence of an electrolyte.

This report reveals pseudocapacitance in highly disordered $LiTiS_2$ that allows for surface redox of titanium on the S-Ti-S slabs. The weak interactions of Li-S allow for facile diffusion and lead to a specific capacitance value as high as 400 F g^{-1} over a 1 V. Contributions from intercalation and pseudocapacitance derive an electrode capacity in excess of 300 mAh g^{-1}, a 30% increase over

theoretical in the same voltage range. Stable cycling is demonstrated for 1000 cycles with no capacity loss and 99.7% CE at a rate of C/2. Density functional theory (DFT) and ex-situ x-ray photoelectron spectroscopy (XPS) confirm the proposed surface redox mechanism as opposed to further intercalation. With no SEI forming and little degradation occurring over cycling, a low rate recovery and additional pressure is used to recover pseudocapactive characteristics. This process is demonstrated multiple times to recover capacity, in essence providing in situ battery recycling.

8.2 Results and Discussion

TiS_2 can crystallize as either the $1T$ (layered), $3R$ (layered), or c (spinel) phases.[296,297] Focus is given to the $1T$ phase due to enhanced properties and thermodynamic stability.[298] The reaction coordinate of TiS_2 has been documented to proceed in three steps shown in Equation 1 through 3:

$$TiS_2 + Li^+ + e^- \rightarrow LiTiS_2 \qquad 2.4V vs. Li^+/Li \tag{8.1}$$

$$LiTiS_2 + Li^+ + e^- \rightarrow Li_2TiS_2 \qquad 0.5V vs. Li^+/Li \tag{8.2}$$

$$Li_2TiS_2 + 2Li^+ + 2e^- \rightarrow Ti^0 + Li_2S \qquad 0.3V vs. Li^+/Li \tag{8.3}$$

Equation 8.1 manifests as a sloping voltage profile from approximately 2.4 to 1.8 V due to a solid solution of Ti^{4+} and Ti^{3+} within the lattice during lithium intercalation.[299] Interestingly, there is little interaction between lithium and sulfur during the upper voltage intercalation with the formal charge on lithium actually closer to 0.2 rather than a full ionization to 1.0.[300] Once all the octahedral sites are saturated in the van der Waals gap with Li, a sharp voltage drop is observed. Equation 8.2 is a flat plateau with a continual saturation of Li into tetrahedral sites in between the slabs reducing titanium further to the 2+ state.[301,302] Finally, a full conversion of to titanium metal and lithium sulfide is observed at voltages close to 0 similar to other TMDs. This conversion has been documented to be rather irreversible.[303]

A novel method has been developed using Li_3N to mechanochemically lithiate TiS_2 while reducing particle size.[254] This method is used to produce few slabs thick $LiTiS_2$ domains starting from 50 μm grain sizes. Figure 8.1a are x-ray diffraction (XRD) patterns for the three samples investigated in this study: bulk TiS_2 (bTS), nano crystalline $LiTiS_2$ (aLTS), and amorphous $LiTiS_2$ (aLTS). bTS has distinguished peaks at 35 and 44 degrees 2θ; whereas nLTS shifts peaks with lithiation to 34 and 43 degrees 2θ, both indicative of the 1T polymorph. Using the Scherrer equation,[304] the particle size of bTS and nLTS is 50.2 nm and 17.5 nm, respectively. aLTS is completely x-ray amorphous as demonstrated by the lack of peaks. We are aware of only one study which was able to successfully synthesis amorphous LTS.[255] To investigate microstructure, due to extreme air sensitivity of the sample, all preparation must take place under an inert environment. Figure 8.1b is a progression for transmission electron microscopy (TEM) sample preparation. Platinum is sputtered onto a particle of interest. Focused ion beam (FIB) milling using gallium ions create a cross section. The material is then lifted out and attached to a TEM grid and additionally fine milled to an appropriate thickness. Figure 8.1c is an energy dispersive spectroscopy (EDS) spectrum taken of the particle shown in Figure 8.1b. Only Ti and S are detected in a precise 2 to 1 ratio. The sample was therefore not oxidized. Figure 8.1d is an enhanced scanning electron microscopy (SEM) image in Figure 8.1b. The particle sizes are in the range of 50 - 300 nm. As there is no solid electrolyte, it doesnt really matter what sizes the particles are, however, a distribution provides greater packing efficiency. Figure 8.1e is a TEM of aLTS. The material appears extremely disordered and no identifiable domains are detected. However, Figure 8.1f, the selected area electron diffraction (SAED) pattern of the region shown in Figure 8.1e demonstrates a polycrystalline structure in the system. The two prominent rings correspond to the (1 0 1) and (1 1 0) planes and have lattice parameters of 2.640 Å and 1.727 Å, placing them within 2% and 0.2% of reported values,[253] respectively. Figure 8.1g is an enlarged version of Figure 8.1e. Domains are seen on the order of a few nanometers, corresponding to a few slabs thick of TiS_2. These partial domains are located in an amorphous matrix.

To probe the diffusivity of the prepared TiS_2 variants, the galvanostatic intermittent titration

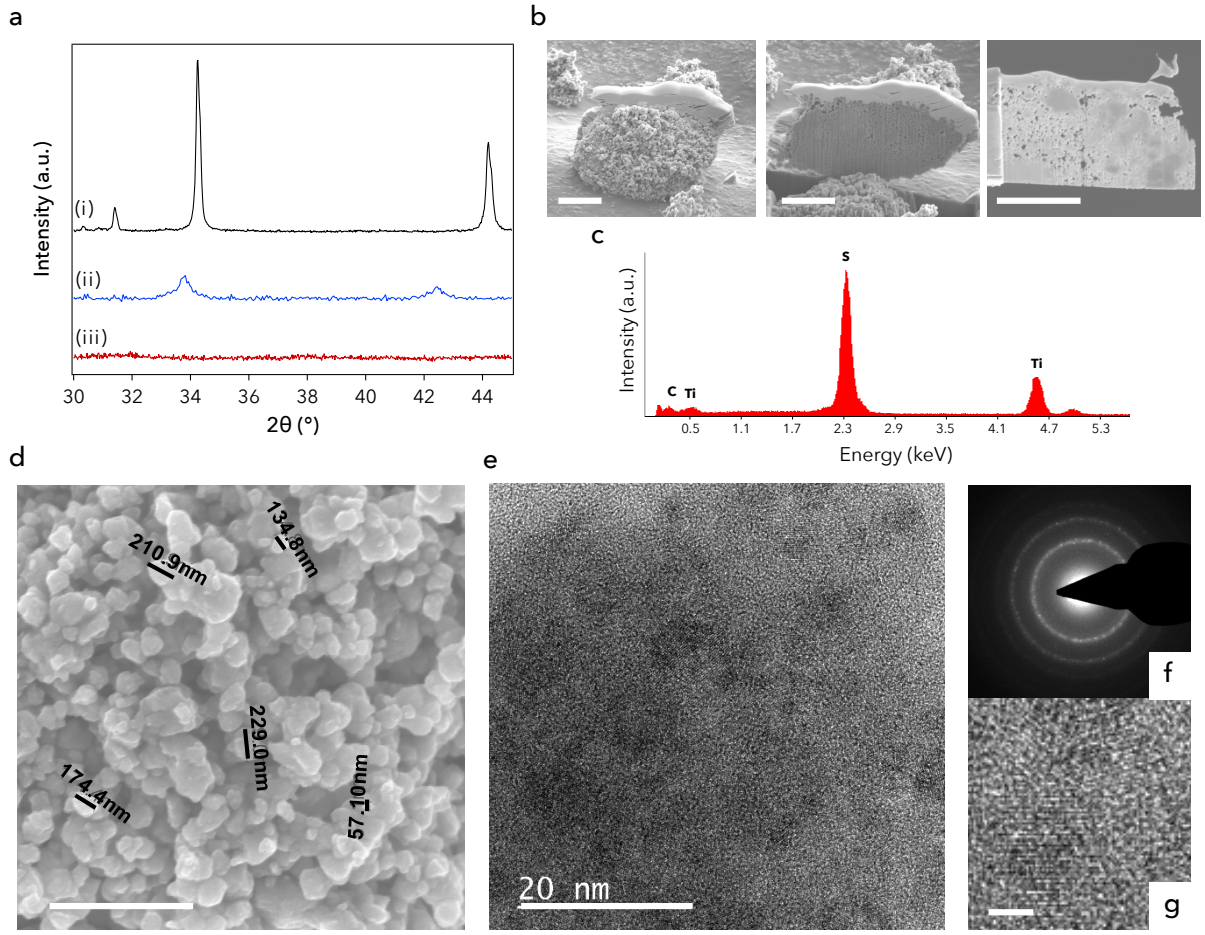

Figure 8.1: a) XRD patterns of: (i) bulk TiS_2 [bTS], (ii) nano crystalline 1T-$LiTiS_2$ [nLTS], (iii) amorphous $LiTiS_2$ [aLTS]. Peak broadening from bTS to nLTS clearly indicates a more nano structure. The lack of peaks for aLTS demonstrate an x-ray amorphous property. b) Preparation of TEM sample using a Ga ion FIB milling. Scale bars are 5 µm. c) EDS spectrum of amorphous $LiTiS_2$. d) SEM of amorphous $LiTiS_2$. Scale bar is 1 µm. e) HR-TEM of cross section of amorphous $LiTiS_2$. f) SAED of HR-TEM in Figure e. g) Enlargement of Figure e. Scale bar is 1 nm. The data presented in Figure e to g indicate a polycrystalline structure for aLTS with domains on the order of 3 - 5 nm or only a few S-Ti-S slabs thick.

technique (GITT) is used. The GITT technique was developed by Weppner and Huggins[258] and furthered by Wen et al.[259] This technique applies a current pulse to the system and measures the relaxation voltage. The calculation is given by Equation 7.3. GITT is performed by using a rate of C/20 for 1 hour followed by a 6 hour relaxation over the voltage range of 3 to 1 V on the third cycle.

Figure 8.2 displays the result of GITT experiment. Both bTS and nLTS display the familiar

characteristics of the $1T$ variant. This includes a low initial coefficient responding to initial separation of S-Ti-S slabs with increasing lithium. Once sufficient space is developed in the van der Waals gap, D_{Li} is increased to a maximum at approximately 0.6 moles of Li in Li_xTiS_2. A decline is D_{Li} is then observed as the octahedral sites in the van der Waals gap is completely saturated with Li. aLTS has very different characteristics. An extremely high D_{Li} is observed at initial stages of lithiation followed by a decrease. This could indicate that due to the disordered nature of aLTS, Li does not act to expand the van der Waals gap. Thus the decrease in D_{Li} would respond to higher levels of Li saturation. A maximum in D_{Li} is again observed at the same level as nLTS. Differing from the other samples, instead of a sharp drop-off in D_{Li}, a constant is achieved. The constant could be related to diffusion along the surface of the S-Ti-S slabs. Once the surface of these slabs begin to saturate, a drop-off is again seen in D_{Li}.

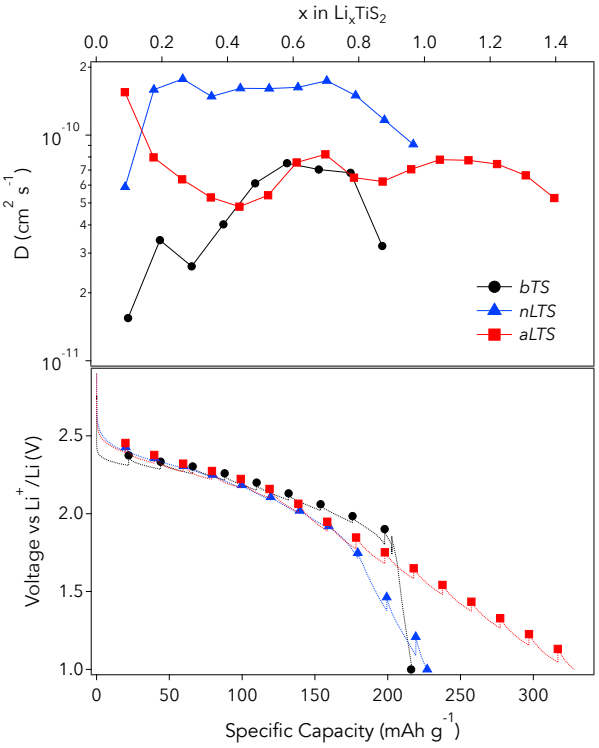

Figure 8.2: GITT for the three samples. (Upper) Computed diffusion coefficients. (Lower) Voltage profile with relaxed voltages in the solid markers. Both bTS and nLTS display well known trends in diffusion coefficient where a maximum is achieved around 0.6 moles of Li, while simultaneously achieving theoretical capacity. aLTS has an undocumented trend with a stable, high diffusion coefficient far past the thermodynamic limit for the material.

Figure 8.3 displays electron energy loss spectroscopy (EELS) of the cross-section developed in Figure 8.1 of *a*LTS. The particles, having been detailed to be in the 50 - 300 nm range in Figure 8.1d, are visible as the dark domains in Figure 8.3. The S-K and Ti-K signals (Figure 8.3b and 8.3c, respectively) are present in the dark domains; however, the Li-K signal (Figure 8.3d) is confined to the what appears the particle boundaries and what appears the much lighter domains in Figure 8.3a. Therefore, it is concluded that the lithium reacts with the gallium ion milling to form on the surface of the particles, which is consistent with literature.[305] Due to high mobility of Li in *a*LTS, we do not expect this phenomenon to significantly alter the structure detected by HR-TEM in Figure 8.1.

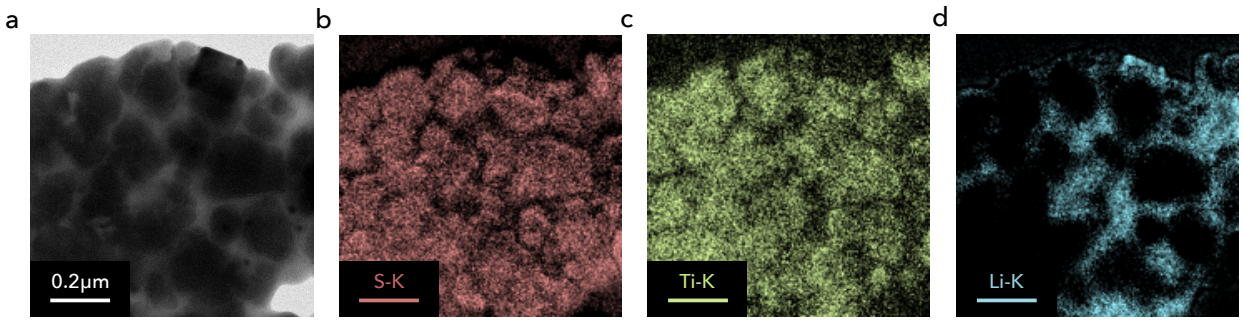

Figure 8.3: a) SEM of *a*LTS cross-section prepared by gallium ion FIB mill. b) S-K EELS signal. c) Ti-K EELS signal. d) Li-K EELS signal. It appears that Li reacts with the milling process acting to deintercalate the material, forming a lithium matrix around the TiS_2 material.

The electrochemical characteristics of *a*LTS are displayed in Figure 8.4. A reversible CV from 3 to 1 V is shown in Figure 8.4. Similarly to CVs performed in the past on materials such as MnO_2 and RuO_2,[276,306] good reversibility is achieved by demonstrating an overlap in sweeps. Particularly, a reversible diffusive peak is exhibited at 2.2 V which is the standard intercalation peak of Li^+ into TiS_2. From approximately 2 to 1 V, however, the characteristics are quite familiarly close to an ideal capacitor rectangle. To illustrate this different characteristic further, the sweep for *a*LTS is overlapped with *n*LTS at a 0.1 mV s^{-1} rate in Figure 8.4. *n*LTS exhibits characteristics previously determined for nano-crystalline TiS_2, with the second shoulder peak from 2.2 to 1.8 V attributed to an intercalation pseudocapacitance effect.[292] Previously, this effect had only been demonstrated in

increasingly nano domains of TiS_2 and not seen in the bulk in a liquid cell. Interestingly, this same pseudocapacitive shoulder is demonstrated in *b*TS and *n*LTS particles (Figure 8.5). This indicates that perhaps a different mechanism is apparent for pseudocapacitance in the solid-state. *a*LTS has much different characteristics: broader diffusive peaks with greater hysteresis, no shoulder after the diffusive peak, and a broad rectangular section from 2 to 1 V. While *n*LTS has a small response in the 2 to 1 V region, consistent with previous reports,[292] *a*LTS has a profound region. This is worth continuing to investigate. A full spectrum of 3 to 1 V CVs are displayed in Figure 8.5.

Figure 8.4c are a variety of sweep rates performed for *a*LTS from 1 mV s^{-1} to 100 mV s^{-1}. The general rectangular shape is preserved with slight distortion at high rates. The distortion could be from the usage of a lithium metal counter electrode and large uncompensated resistance of the solid-state electrolyte.[307] A 3-electrode cell becomes extremely tricky when using a solid electrolyte layer while attempting to reduce resistance (thickness) as much as possible. CVs in the range of 2 to 1 V for *b*TS and *n*LTS are in Figure 8.6. Figure 8.4d are specific capacitance values in the range of 2 to 1 V for the three samples calculated with the following equation:

$$C = \frac{1}{m\nu\,|V_c - V_a|}\int_{V_a}^{V_c} i(V)dV \tag{8.4}$$

where m is the active material loading, ν is the scan rate, V_c and V_a are the cathodic and anodic potential, respectively, and $i(V)$ is the current response.[307] A capacitance value near 400 F g^{-1} for *a*LTS is one of the highest reports for a material over a 1 V voltage window. Previous reports for TMDs include the diffusive voltage window which obscures the actual capacitance value.[292] Figure 8.4e overlaps a normalized CV for the three samples at a rate of 10 mV s^{-1}. *b*TS and *n*LTS demonstrate a sharp anodic increase followed by a peak near 1.8 V. This could indicate that the shoulder seen in Figure 8.4b is actually part of the diffusive region and possibly mischaracterized earlier. For the possibility that temperature is skewing results, the effect of temperature on specific capacitance is investigated in Figure 8.7. Only a small effect is demonstrated, much more impacting in the diffusive region. Therefore, performing sweeps in the pseudocapacitive range is less impacted.

Figure 8.4f plots the peak anodic current versus the log of the sweep rate in the CVs. For a capacitive behavior, the slope of the line should be unity.[308]

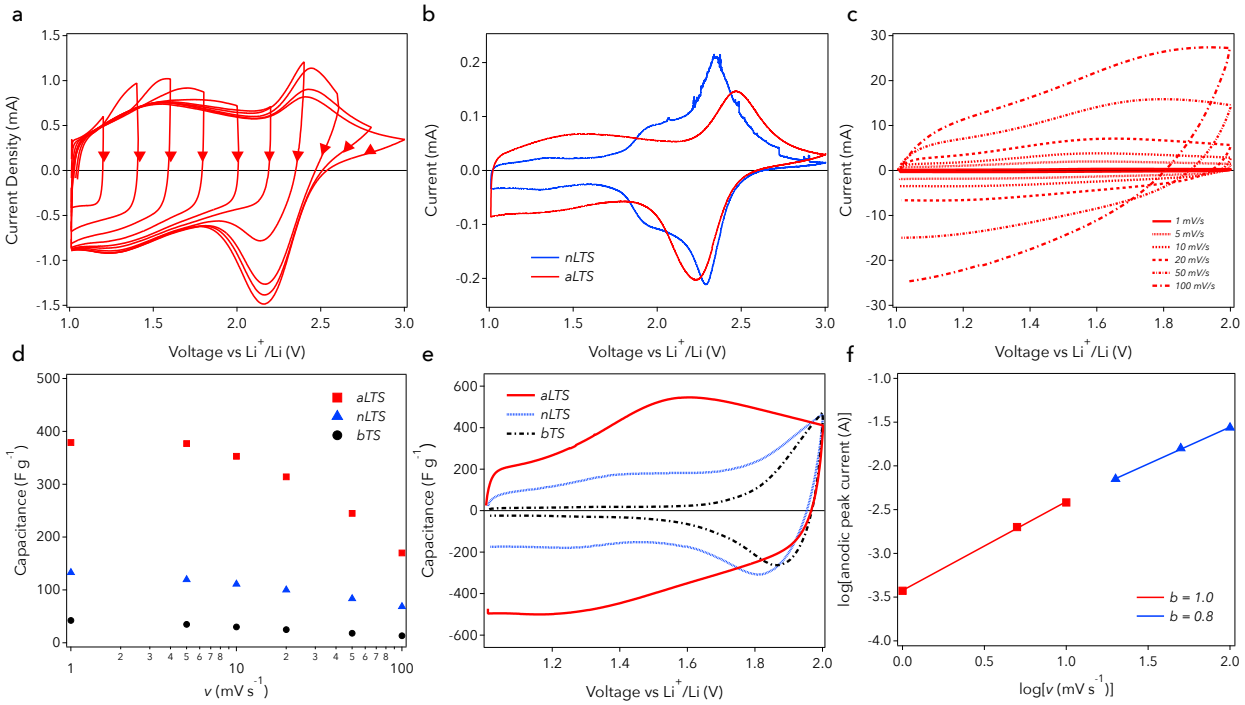

Figure 8.4: a) Reversible sweep of amorphous $LiTiS_2$ at 5 mV s^{-1}. b) Overlay of CVs of nano 1*T*-$LiTiS_2$ and amorphous $LiTiS_2$ at a sweep rate of 0.1 mV s^{-1}. c) Various sweep rates of amorphous $LiTiS_2$. d) Computed specific capacitance values for three samples in the voltage range of 2 to 1 V. e) Overlay of sweep of three samples at 20 mV s^{-1}. f) Log of peak current versus log of sweep rate for Figure c.

CVs in the voltage range of 3 to 1 V for *b*TS, *n*LTS and *a*LTS at 60°C are displayed in Figure 8.5a to 8.5c and at 120°C in 8.5d to 8.5f, respectively. The large shifts in redox peaks in *b*TS at 60°C in Figure 8.5a are much larger than those reported in liquid cells. These shifts in both cathodic and anodic peaks are a result of large uncompensated resistance of the solid electrolyte layer.[51] Typically, liquid electrolyte resistance are almost 10 times less resistive than a solid electrolyte layer, therefore, the temperature is raised to 120°C for proper response. It is clear that once the CV is performed at 120°C for *b*TS in Figure 8.5d, no large increase in capacitance is observed in the 1 to 2 V region. This could indicate the any capacitive response is not a result of the elevated temperature but a material response. *n*LTS in Figure 8.5b and 8.5e has a similar behavior to *b*TS

but with a larger peak shift. This could be the result of access to more material at the higher rates as both samples contain the same amount of material. A small rectangular portion is exhibited near 1 V during sweep rate reversal. This small pseudo-capacitive effect has been documented in nano $LiTiS_2$ previously. *a*LTS exhibits the largest shift in cathodic voltage with scan rate in Figure 8.5f. This is typical for a large activation energy as the anodic peak does not undergo the same shift.[51] This same shift is present at elevated temperatures (Figure 8.5f) with a smaller degree. During sweep rate reversal, a sharp increase in current response occurs followed by a reversible peak at the same voltage for all rates. This has been a well documented pseudo-capacitive effect.[307]

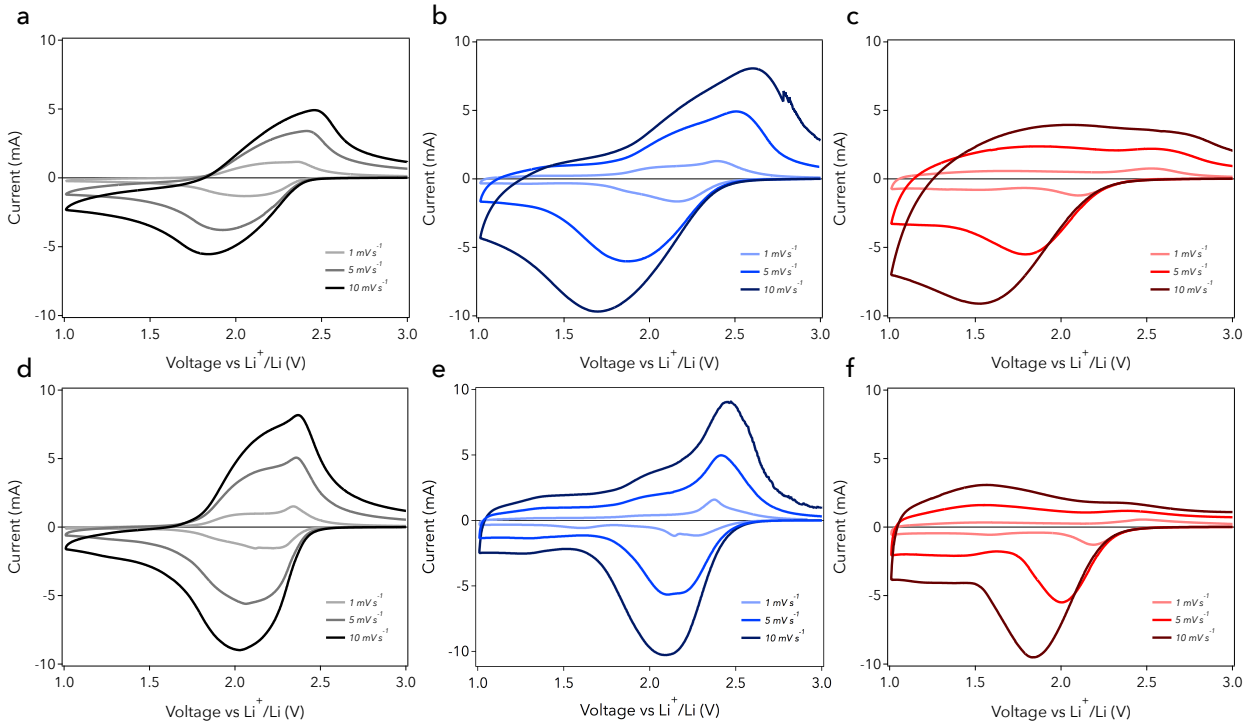

Figure 8.5: Cyclic Voltammetry over a 3 to 1 V range at 60°C for a) *b*TS, b) *n*LTS, c) *a*LTS. The same tests performed at 120°C for a) *b*TS, b) *n*LTS, c) *a*LTS. While *b*TS and *n*LTS have similar shapes, the more nano *n*LTS is able to achieve greater delivered current in the solid-state. At the same time, larger peak shifts are identified in *n*LTS. *a*LTS has a complete different form at both temperatures.

Figure 8.6a and 8.6b are CVs in the range of 1 to 2 V at 120°C for *b*TS and *n*LTS, respectively, the same test as performed in Figure 8.1c displaying a sharp contrast. *b*TS does not display any pseudocapacitance in this range. The cathodic and anodic response appears to be a result of

delithiation and lithiation of the diffusive type indicated by a cathodic peak following the anodic response that displays a voltage shift.[51] *n*LTS displays more pseudocapacitance with the longer plateau of current developing into two stages essentially. There still appears to to be some diffusive response near 2 V which is adding to the overall calculated capacitance value in Figure 8.3d. It is unclear if this pseudocapacitance is surface redox as demonstrated by *a*LTS or intercalation pseudocapacitance as previously reported.[292]

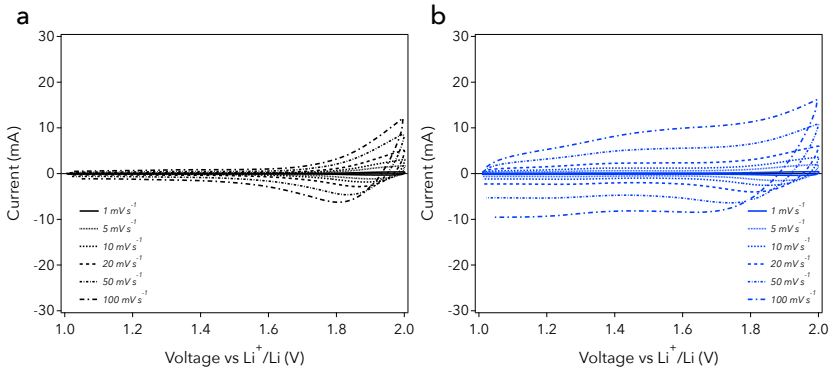

Figure 8.6: CVs over a 1 to 2 V range at 120°C for a) *b*TS, b) *n*LTS. The behavior developed near 2 V are clearly diffusive in nature due to peaks developed on the cathodic sweep following the anodic sweep. This diffusive region adds the specific capacitance values formed in Figure 8.4 and are incorrect in referring to a capacitance value.

Figure 8.7a are CVs for *a*LTS in the 1 to 2 V range at a variety of temperatures. This is to determine if by raising the temperature to 120°C for testing has any significant effect on *a*LTS characteristics. For all temperatures, specific capacitance is not significantly effected by temperature and *a*LTS still exhibits strong pseudocapacitance (over 300 F g^{-1} in Figure 8.7b) at 60°C. While the current derived increases slightly with temperature, there is also a change in the steepness of current reversal during sweep rate reversal at 2 V. This has been reportedly due to uncompensated resistances in the design cell which demonstrates that raising conductivity in the solid electrolyte, provides a better response for determining pseudocapacitance in the solid-state.

Cycling results for using *a*LTS is in the full range of 3 to 1 V are shown in Figure 8.8. 1000 cycles are demonstrated at a rate of C/2 with no capacity fade. *a*LTS has a stable capacity of 300 mAh g^{-1} which is far above theoretical for $LiTiS_2$ (227 mAh g^{-1}) and TiS_2 (240 mAh

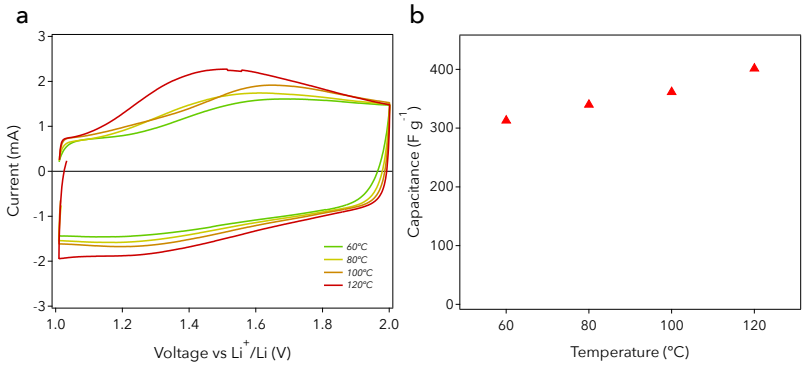

Figure 8.7: a) CV of *a*LTS over a 1 V range at various temperatures, b) Computed capacitance values for increasing temperatures. While slight amounts of capacitance are added with increasing temperature, the relative shape of the CV is almost unchanged. A large effect is seen during the switch from anodic to cathodic current. Increasing temperature reduces the uncompensated resistance and increases the vertical nature of this switch.

g^{-1}). Comparatively to *n*LTS and *b*TS both of which fade extremely quickly at these high rates in the absence of liquid electrolyte. A few possibilities can be attributed to this. First would be a more isotropic diffusion within *a*LTS. This allows for diffusion to be less effected at grain boundaries due to increased disorder. The second would be possibly less volume change due to the disorder. This is furthered by the fact that *n*LTS outperforms *b*TS. Figure 8.9 demonstrates an average coulombic efficiency of 99.7% in this range and also contains relevant voltage profiles. A rate study is performed in Figure 8.8. Rate is symmetrically increased from C/5 to 8C. *a*LTS sustains higher capacities than the other two. At 8C, the capacity of 210 mAh g^{-1} is still near theoretical for crystalline LTS. The discharge voltage profiles for *a*LTS are shown in Figure 8.4c. Although an increasing reduction in voltage can be seen for the diffusive peak the dQ/dV, the constant sloping tail at lower voltages is always present. This is the pseudocapacitive region. A constant slope in the dQ/dV is a clear capacitive response. Figure 8.10 isolates the cycling ability within the pseudocapacitive region from 2 to 1 V. Cycling is seen for over 750 cycles at a rate of 2C, however, capacity fade is exhibited which demonstrates a symbiotic relationship of cycling over the full diffusive and capacitive regions.

Figure 8.9 pertains to additional information for cycling in Figure 8.8. The coulombic efficiency for *a*LTS over the course of cycling at C/2 is displayed in Figure 8.9a. Taking a fit, the

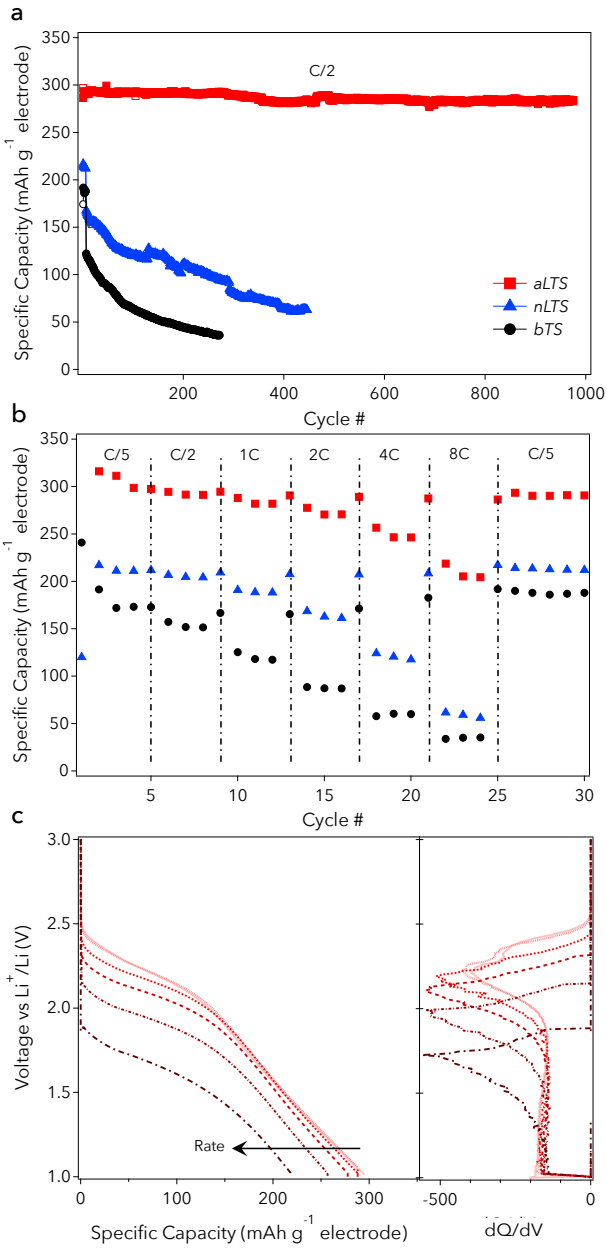

Figure 8.8: a) Cycling at a rate of C/2 for all three samples. b) Rate study of all three samples. c) Voltage profiles and dQ/dV of *a*LTS during rate study. Not only can *a*LTS achieve capacities as high as 300 mAh g^{-1}, but this capacity is stable for 1000 cycles. Indications of a constant dQ/dV for low voltages are a clear capacitive behavior.

average CE is 99.7%. Some variation can be due to small temperature fluctuations in the oven used to operate the cells at 60°C. Figure 8.9b, 8.9c, and 8.9d are voltage profile evolutions for *a*LTS, *n*LTS, and *b*TS, respectively, in Figure 8.8a. *a*LTS keeps its distinct shape over the course of the

1000 cycles including the pseudocapacitive range. Both *n*LTS and *b*TS exhibit a plateau shortening and rising ohmic overpotential. Possible explanations for the better cycling stability include lower volumetric changes in *a*LTS due to disordering and smaller domain sizes, and lower active material isolation in *a*LTS due to more isotropic diffusion of lithium.

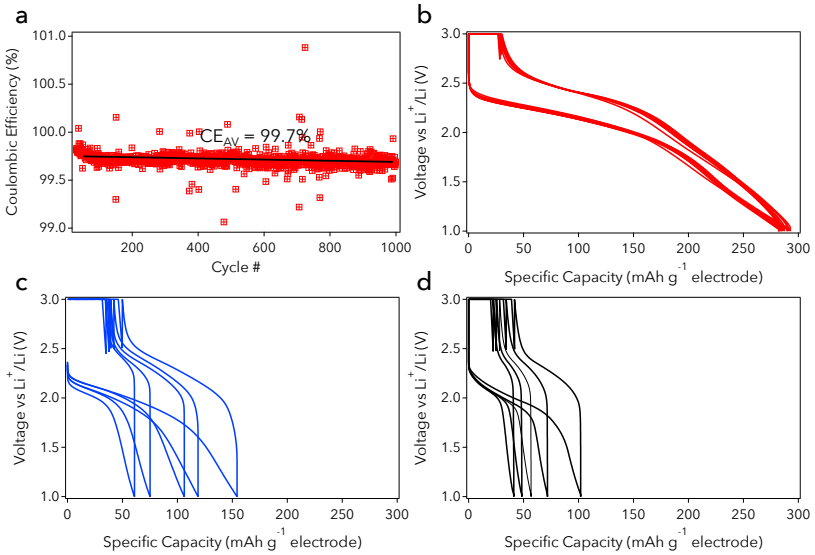

Figure 8.9: a) CE over the course of cycling at C/2 for *a*LTS. b) Voltage profile evolution (every 100 cycles) for at C/2 for b) *a*LTS, c) *n*LTS, d) *b*TS. The pseudocapacitive region for *a*LTS is present throughout the 1000 cycles.

The effects of cycling purely in the pseudocapacitive range for *a*LTS is investigated (Figure 8.10). A rate study is performed up to 20C (1.44 A g^{-1}), the highest ever reported for a solid-state cell. The voltage sweeps in the 2 to 1 V range are displayed in Figure 8.10a. Extended cycling is then carried out at 2C (0.28 A g^{-1}) for 750 cycles (Figure 8.10b). This is the same rate as used in Figure 8.8 for extended cycling. Interestingly, as opposed to when *a*LTS is cycled over the full 3 to 1 V range, the 2 to 1 V range exhibits drastically more capacity fade. This could be because the 2 to 1 V range includes some diffusive reaction with lithium and therefore, looses some lithium per cycle.

To elucidate the mechanism of pseudocapacitance, ex-situ XPS is performed on samples of *a*LTS at various stages of lithiation (Figure 8.11). XPS is performed so the sample is never exposed to air. Changes in sulfur oxidation state provide the clearest picture of redox behavior. At 3 V, the

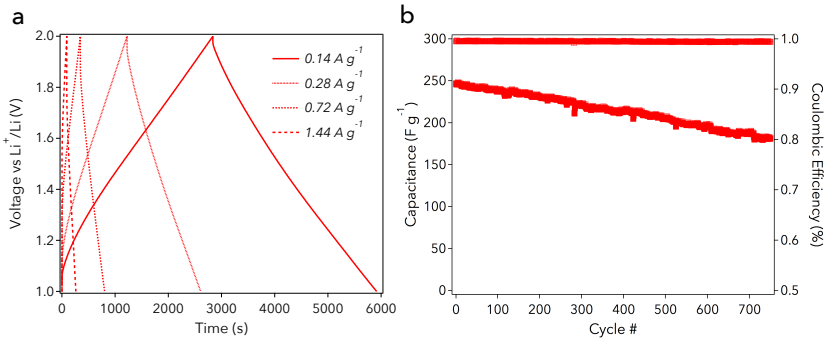

Figure 8.10: a) Voltage vs time for *a*LTS at increasing rates up to 20C. b) Extended cycling at 2C in the 2 to 1 V region. While the current is slightly greater for extended cycling than Figure 8.8, there is a much larger capacity fade when only using the lower region. This could indicate there is a symbiotic relationship when cycling over the full 3 to 1 voltage range. Perhaps overlap in the diffusive and capacitive regions could be the cause of the greater fade.

majority component is Ti-S in the doublet at 160.7 and 162 eV, relating to the S $2p_{3/2}$ and $2p_{1/2}$, respectively.[309] A small amount of lithium was detected in the elemental analysis which is expected as full lithium removal is extremely unlikely upon full charge. A broad tail is observed. This could be due to partial oxidation which has been reported for thin films of TiSO.[310] As EDS in Figure 8.1 confirmed the presence of no oxygen, this is most likely the result of partial oxidation. At 2 V, close to full intercalation has occurred therefore the peaks have been fitted to included Ti-S in both a lithium deficient and lithium intercalated environment. The shift for lithium intercalation is relatively small.[123,309,311] Finally, at 1 V, a new doublet appears at low binding energies, 160 and 161.2 eV. This is consistent with a Li-S interaction and more particularly, a surface Li-S interaction.[312–314] This sheds light that the mechanism for pseudocapacitance would happen at the surface of a TiS_2 slab. Figure 8.12 confirms the formation of Ti^{2+} at 1 V. A peak at 455 eV is indicative of a Ti^{2+} in an octahedral environment as in TiS.[315] The Li XPS peak also broadens and shifts lower during the lithiation process as seen in Figure 8.12. For the 1 V sample, a Li peak at 54.6 eV represents a Li-S interaction.[316] XPS on Li in $LiTiS_2$ has never been reported but Li is reported to not have strong interactions with sulfur when in the van der Waals gap, and acts more like a liquid metal in this state.[300] That would place the XPS peak closer to 55.2 eV.[317]

XPS results, along with CV analysis, supports the conclusion that the pseudocapacitance

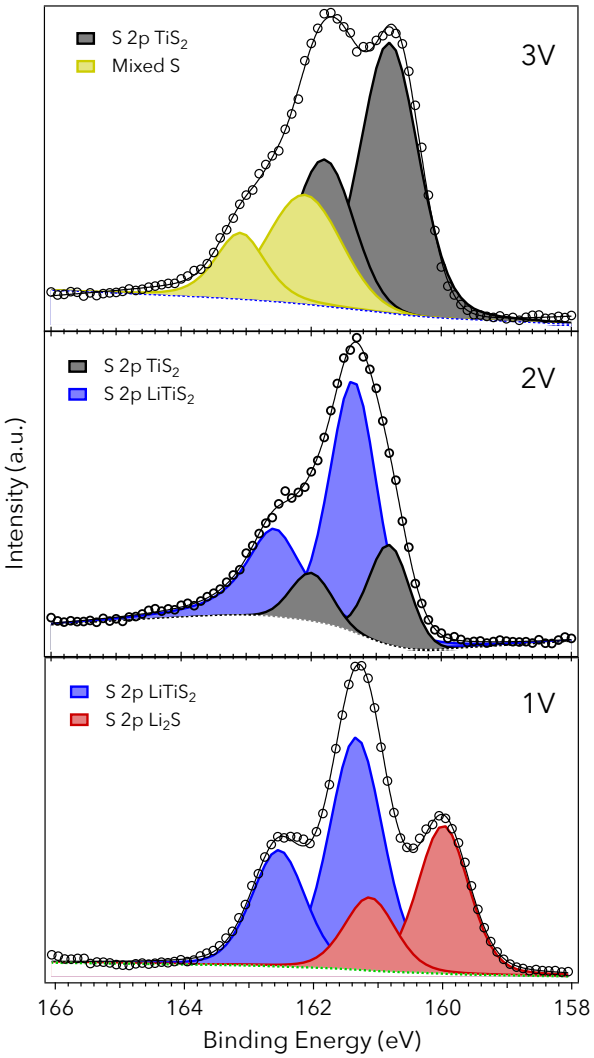

Figure 8.11: Ex-situ XPS spectra for S bonding in *a*LTS at different stages of lithiation. The main divergence from literature occurs at 1 V when peaks associated with a Li - S ionic interaction appear.

developed is from Li reducing the outer most slabs Ti from the 3+ to 2+ states. This mechanism proceeds after full intercalation into the van der Waals gap. High levels of reversibility and diffusion can be achieved as Li only coordinates to three S atoms on the surface of the S-Ti-S slab rather than a six fold coordination in between the layers. Density functional theory analysis has demonstrated hypothetical diffusion taking place along a S-Ti-S layer and lower energy barrier for Li hops.[318] Additionally a sheet voltage of 1.5 V is predicted which matches well with the average pseudocapacitive voltage in the case of *a*LTS.

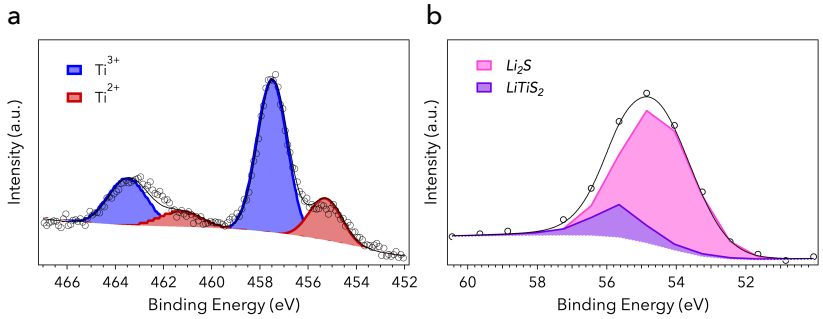

Figure 8.12: Ex-situ XPS spectra at 1 V in *a*LTS for, a) Ti, b) Li. The Ti results clearly indicate a Ti^{2+} state forming in an octahedrally coordinated environment. Li develops an ionic interaction with S.

Theoretically, TiS_2 has a specific capacity of 240 mAh g^{-1}; calculations for this value assume one mole of lithium per S-Ti-S unit. However, this scenario is only correct if it is assumed the domain size is infinite. Since lithium can only sit in between the TiS_2 slabs, once the domain size of the material is significantly reduced, the total number of slabs will become important for calculating a theoretical intercalation capacity. For instance, if the domain size only contains two TiS_2 slabs, one mole of intercalated lithium results in a theoretical intercalation capacity of 112 mAh g^{-1}. Figure 8.13 displays theoretical calculations for decreasing domain size of TiS_2. Only one the grain size is less than approximately 12 nm or 20 S-Ti-S slabs, does the intercalation capacity significantly differ from the overall capacity. As it is assumed that additional capacity is derived from using surface sulfur coordination at the outer most S-Ti-S slabs in *a*LTS, theoretical calculations have also been included for this amount defined as a "capacitive" contribution. It is clear in Figure 8.13 that this capacitive contribution only becomes significant at extremely small domain sizes such as the domains identified in Figure 8.1. The total capacity derived can deviate from traditional studies of $LiTiS_2$ and explain the significant increases developed in Figure 8.2 and 8.8.

If the pseudocapacitive contribution to *a*LTS is indeed developed from surface Ti redox and S coordination, then with decreasing grain size (ie. more surface area) should increase the overall capacitive contributions. Figure 8.14 is the deep discharge characteristics of increasing nano domains of $LiTiS_2$. Beginning with *b*TS, TiS_2 is ball-milled with Li_3N for increasing amounts

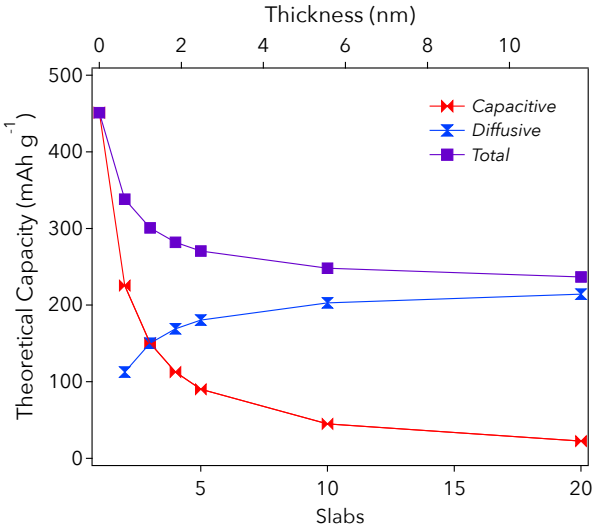

Figure 8.13: Calculated specific capacities for extremely small grain sizes in $LiTiS_2$. Diffusive capacities are related to the intercalation of Li into the van der Waals gap. Capacitive contribution are related to coordination on the outer most S-Ti-S slabs. As domain size decreases, more Li can coordinate to the surface states rather than in between the layers. The total capacity using both forms increases the theoretical past the traditional limit of 240 mAh g^{-1}.

of time - 2, 5, 10, and 20 hours. 2 and 20 already correspond to *n*LTS and *a*LTS, respectively. However, intermediates are developed that have smaller domain sizes than *n*LTS but begin to disorder similar to *a*LTS. All samples are lithiated to 0.01 V at a rate of C/20. Voltage profiles and associated dQ/dV are displayed in Figure 8.14. First analyzing *b*TS, the discharge characteristics match closely with literature. This is important to note that the same transformation can occur in solid-state as in liquid. The upper region from 2.4 to 1.8 V can uptake a full mole of lithium to form $LiTiS_2$. Then at 0.5 V, the reaction following equation 2 proceeds until another mole of lithium is taken to make the singular phase of Li_2TiS_2. The important difference in solid-state is the lack of SEI formation at 0.9 V noted in literature. Finally the full conversion to Ti^0 and Li_2S takes place as in equation 8.3. It appears the full conversion does not take place as only 3.5 moles of lithium are consumed which is most likely due to the large starting crystallite size of *b*TS. When forming a more nano domain as in *n*LTS (LTS-2h), the upper intercalation region shortens as the unit cell can no longer be counted as infinite (see Figure 8.13). Therefore the theoretical capacity diminishes. *n*LTS still displays the overintercalated version of Li_2TiS_2 in which lithium

shifts from octahedral to tetrahedral sites in the van der Waals gap. The final conversion is not as present in *n*LTS which could be blurred by the nano domain size. The trends in LTS-5 to LTS-20 are quite noticeable and provide profound insight into the mechanism of pseudocapacitance. From LTS-5 to LTS-20, the upper intercalation capacity decreases related to a decrease in crystallite size. The amount of pseudocapacitance increases with increasing disorder (lower slope from 2 to 1 V), this is also obvious with higher dQ/dV values. From LTS-5 to LTS-20, the amount of overintercalated plateau shortens until it almost disappears with LTS-20. If surface redox proceeds as the primary pseudocapacitance mechanism, the total overintercalated phase will diminish as lithium will be preferentially stored on the surface of the slab at higher voltages. As there doesn't appear to be any formation of Li_2TiS_2 in LTS-20, most likely the domain size is near 5 slabs thick which matches HR-TEM data in Figure 8.1. Finally the conversion process still proceeds in LTS-5 through LTS-20. Interestingly, all samples are almost able to fully react with 4 moles of lithium. This is an important concept as developing *a*LTS does not change the final discharge products are ability to store necessarily more lithium. It simply changes the reaction pathway of where lithium preferentially sits over the course of the reaction coordinate. The pseudocapacitive surface redox of S-Ti-S slab becomes more favorable than overintercalation to Li_2TiS_2.

If indeed the pseudocapacitance mechanism is surface redox, more surface area would promote more capacity in the lower voltage region. Figure 8.15a displays a cycle at 0.21 mA cm^{-2} for mass loading from 0.75 mg cm^{-2} to 15 mg cm^{-2}. Clearly with increasing mass loading, the intercalation region shortens and the pseudocapacitive region elongates. This is an interesting effect so that the same amount of lithium is roughly stored at the 1 V cutoff. This supports the theory of surface redox. This also confirms that the pseudocapacitance is not occurring at the electrode/electrolyte interface as the surface area of contact remains constant but scaling occurs in the z direction and the same overall capacity is achieved.

When working the sulfide family of glass electrolytes, there is always the possibility of electrolyte activation to provide additional capacity.[228] Therefore it is important to check to make sure that the observed pseudocapacitance effect is not influenced by the choice of electrolyte selection.

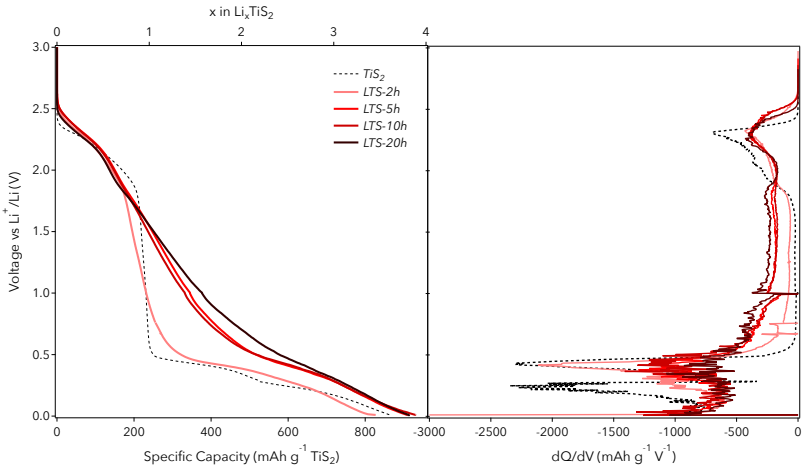

Figure 8.14: Discharge of TiS_2 ball-milled with Li_3N for 0, 2, 5, 10, and 20 hours at a rate of C/20 to 0.01 V following an initial charge of 3 V. Associated dQ/dV is matched to define the reaction plateaus. Whereas *b*TS follows the three reactions in Equations 8.1 to 8.3, with increasing milling time (smaller domain size) larger capacitance is derived in lieu of Equation 8.2 when Ti is reduced to the 2+ state.

Therefore, the electrolyte composition used for the separator was varied from $77.5Li_2S - 22.5P_2S_5$ to $60Li_2S - 40P_2S_5$ and *a*LTS was discharge (Figure 8.15b). With decreasing amounts of Li_2S conductivity decreases significantly, which accounts for the increasing ohmic overpotential. However, activation is believed to only take place when the Li_2S content exceeds 75 molar as this supersaturates the glass past the final Li_3PS_4 structural unit. In all three cases, pseudocapacitance exists suggesting a product of *a*LTS and not the solid electrolyte.

To further this understanding of possible electrolyte activation, solid electrolyte was used as a separator [2D Interface] (typical construction for all cells in this study) or mixed into the cathode itself with TiS_2 [3D Interface]. The cell was then initially charged to observe the capacity derived (Figure 8.15c). Only activation of the electrolyte occurs in the 3D interface. Since TiS_2 contains no lithium, all delithation must occur in the Li_2S in the solid electrolyte. Therefore, we can conclude that electrolyte activation plays no role in all the CVs or cycling occurring in this study.

Figure 8.16 demonstrates the ability of the use of *a*LTS, specifically in the solid-state construction, be "recycled. Figure 8.16a demonstrates long-term cycling at 1C. Compared to C/2 in Figure 8.8, *a*LTS degrades at this increased rate. Figure 8.16b demonstrates the voltage profile

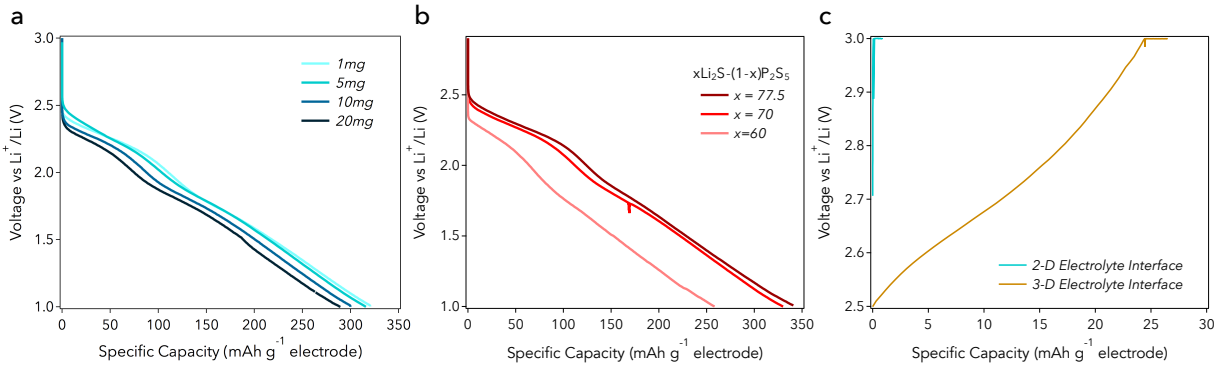

Figure 8.15: a) Increasing thickness of *a*LTS discharged at a rate of 0.21 mA cm^{-2}. b) Discharge of *a*LTS on a variety of sulfide solid electrolyte glasses. c) Initial charge of TiS_2 mounted or mixed with sulfide solid electrolyte.

evolution during the first 350 cycles at 1C. The pseudocapacitive region is lost so that only the intercalation portion is providing capacity. This is a different degradation mechanism than *n*LTS in Figure 8.8. In that case, capacity never became stable and there was in increase in ohmic overpotential. In Figure 8.16b, there is no ohmic overpotential but simply a loss of pseudocapacitance. Once the system is slowed down to a rate of C/10 and additional pressure is applied, the system recovers full capacity before the degradation. The system is then run for another 200 cycles at 1C before being slowed down to C/10 again to recover capacity. Figure 8.16c shows the voltage profiles at initial C/10, the first and second recovery. The first and second recovery contain a shorter pseudocapacitive region but a lengthening of the intercalation portion. This could indicate there is structural changes in *a*LTS over cycling. The idea of capacity recovery can not be applied to a liquid cell as SEIs typically form which prevent the reformation of the original structure. However, since an SEI does not form on *a*LTS and the pressure can be finely tuned, the system can be used multiple times in the solid-state.

There is curiosity to use *a*LTS at thicker electrodes. Typically thick electrode cycling is tough to achieve in the solid-state at higher rates due to lack of guaranteed diffusion pathways. Figure 8.17 displays cycling of *a*LTS at a 7.5 mg cm^{-2} mass loading ($\sim$ 25 µm) and a rate of C/5. The system achieves a stable capacity at 250 mAh g^{-1} which is less than when half the mass loading is used but is still greater than theoretical so the pseudocapacitive effect is preserved for extended

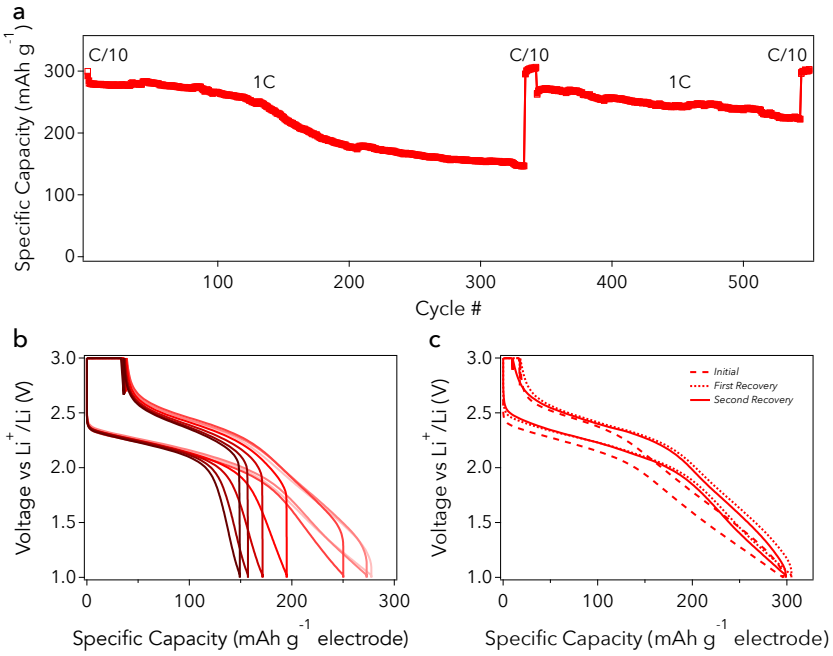

Figure 8.16: a) Cycling of *a*LTS at a 1C rate. The system is slowed down to C/10 and applied additional pressure for 10 cycles. Rate is the increased again to 1C. A second recovery is performed at C/10. b) Voltage profile evolution during the initial capacity degradation at 1C. c) Voltage profiles at C/10 of initial, first recover, and second recovery.

cycling at higher mass loadings.

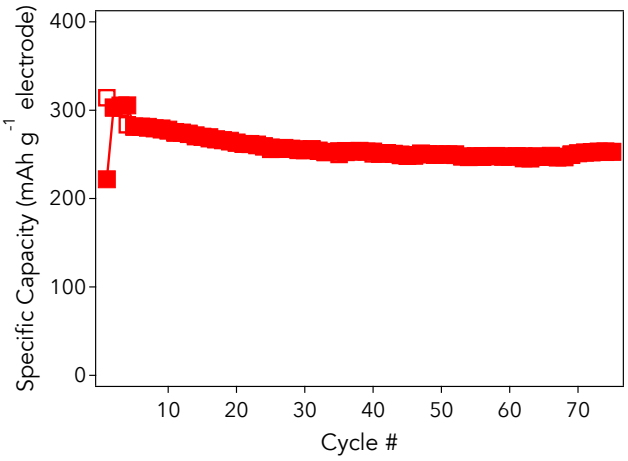

Figure 8.17: Cycling of a 7.5 mg cm^{-2} electrode of *a*LTS at a rate of C/5.

8.3 Conclusion

A new mechanism of pseudocapacitance is revealed in highly disordered $LiTiS_2$. Due to the

extreme nano domains developed, surface redox of titanium in the outer most S-Ti-S slabs allows for highly reversible and facile interactions at elevated voltages. Specific capacitance values of 400 F g^{-1} in the pseudocapacitve region are demonstrated or a stable capacity of 300 mAh g^{-1} is achieved over the full 3 to 1 V range. The resulting device is the first solid-state pseudocapacitor.

Bibliography

[1] M Stanley Whittingham. Lithium batteries and cathode materials. Chemical reviews, 104(10):4271–4302, 2004.

[2] Paul V Braun, Jiung Cho, James H Pikul, William P King, and Huigang Zhang. High power rechargeable batteries. Current Opinion in Solid State and Materials Science, 16(4):186–198, 2012.

[3] V. Etacheri, R. Marom, R. Elazari, G. Salitra, and D. Aurbach. Challenges in the development of advanced li-ion batteries: a review. Energy & Environmental Science, 4(9):3243–3262, 2011.

[4] Jiajun Chen. Recent progress in advanced materials for lithium ion batteries. Materials, 6(1):156–183, 2013.

[5] Robert Huggins. Advanced batteries: materials science aspects. Springer Science & Business Media, 2008.

[6] Emanuel Peled. The electrochemical behavior of alkali and alkaline earth metals in nonaqueous battery systemsthe solid electrolyte interphase model. Journal of The Electrochemical Society, 126(12):2047–2051, 1979.

[7] Doron Aurbach, Boris Markovsky, Gregory Salitra, Elena Markevich, Yossi Talyossef, Maxim Koltypin, Linda Nazar, Brian Ellis, and Daniella Kovacheva. Review on electrode–electrolyte solution interactions, related to cathode materials for li-ion batteries. Journal of Power Sources, 165(2):491–499, 2007.

[8] Languang Lu, Xuebing Han, Jianqiu Li, Jianfeng Hua, and Minggao Ouyang. A review on the key issues for lithium-ion battery management in electric vehicles. Journal of power sources, 226:272–288, 2013.

[9] Alireza Khaligh and Zhihao Li. Battery, ultracapacitor, fuel cell, and hybrid energy storage systems for electric, hybrid electric, fuel cell, and plug-in hybrid electric vehicles: State of the art. Vehicular Technology, IEEE Transactions on, 59(6):2806–2814, 2010.

[10] Sheng Shui Zhang. A review on electrolyte additives for lithium-ion batteries. Journal of Power Sources, 162(2):1379–1394, 2006.

[11] Kazuo Murata, Shuichi Izuchi, and Youetsu Yoshihisa. An overview of the research and development of solid polymer electrolyte batteries. Electrochimica acta, 45(8):1501–1508, 2000.

[12] B Smitha, S Sridhar, and AA Khan. Solid polymer electrolyte membranes for fuel cell applicationsa review. Journal of membrane science, 259(1):10–26, 2005.

[13] Chuizhou Meng, Changhong Liu, Luzhuo Chen, Chunhua Hu, and Shoushan Fan. Highly flexible and all-solid-state paperlike polymer supercapacitors. Nano letters, 10(10):4025–4031, 2010.

[14] SPS Badwal and K Foger. Solid oxide electrolyte fuel cell review. Ceramics International, 22(3):257–265, 1996.

[15] Tomonobu Tsujikawa, Kaho Yabuta, Takashi Matsushita, Toshio Matsushima, Koji Hayashi, and Masayasu Arakawa. Characteristics of lithium-ion battery with non-flammable electrolyte. Journal of Power Sources, 189(1):429–434, 2009.

[16] Subhash C Singhal and Kevin Kendall. High-temperature solid oxide fuel cells: fundamentals, design and applications. Elsevier, 2003.

[17] Peter G. Bruce. Solid state electrochemistry, volume 5. Cambridge University Press, 1997.

[18] J. W. Fergus. Ceramic and polymeric solid electrolytes for lithium-ion batteries. Journal of Power Sources, 195(15):4554–4569, 2010.

[19] J Maier. Nanoionics: ion transport and electrochemical storage in confined systems. Nature materials, 4(11):805–815, 2005.

[20] Marc Doyle, Thomas F Fuller, and John Newman. The importance of the lithium ion transference number in lithium/polymer cells. Electrochimica Acta, 39(13):2073–2081, 1994.

[21] A. Hayashi, K. Noi, A. Sakuda, and M. Tatsumisago. Superionic glass-ceramic electrolytes for room-temperature rechargeable sodium batteries. Nature Communications, 3:5, 2012.

[22] Yan Wang, William Davidson Richards, Shyue Ping Ong, Lincoln J Miara, Jae Chul Kim, Yifei Mo, and Gerbrand Ceder. Design principles for solid-state lithium superionic conductors. Nature materials, 2015.

[23] S. Ujiie, A. Hayashi, and M. Tatsumisago. Structure, ionic conductivity and electrochemical stability of li2s-p2s5-lii glass and glass-ceramic electrolytes. Solid State Ionics, 211:42–45, 2012.

[24] K. Takada. Progress and prospective of solid-state lithium batteries. Acta Materialia, 61(3):759–770, 2013.

[25] K. Kanehori, K. Matsumoto, K. Miyauchi, and T. Kudo. Thin-film solid electrolyte and its application to secondary lithium cell. Solid State Ionics, 9-10(DEC):1445–1448, 1983.

[26] J. B. Bates, N. J. Dudney, D. C. Lubben, G. R. Gruzalski, B. S. Kwak, X. H. Yu, and R. A. Zuhr. Thin-film rechargeable lithium batteries. Journal of Power Sources, 54(1):58–62, 1995.

[27] Boone B Owens. Solid state electrolytes: overview of materials and applications during the last third of the twentieth century. Journal of power sources, 90(1):2–8, 2000.

[28] Klaus Funke. Solid state ionics: from michael faraday to green energy-the european dimension. Science and Technology of Advanced Materials, 14(4), 2013.

[29] Tsutomu Minami, Masahiro Tatsumisago, Masataka Wakihara, Chiaki Iwakura, Shinzo Kohjiya, and Isao Tanaka. Solid state ionics for batteries. Springer Science & Business Media, 2006.

[30] Michael Faraday. Experimental researches in electricity, volume 1851. Taylor, 1851.

[31] Shin-ya Miyatami. α-ag2s as a mixed conductor. Journal of the Physical Society of Japan, 24(2):328–336, 1968.

[32] Walther Nernst. Theoretische chemie vom standpunkte der Avogadroschen regel und der thermodynamik. F. Enke, 1907.

[33] C Tubandt and E Lorenz. The molecular condition and electrical conductivity of crystallized salts. Z Phys Chem, 87:513–542, 1914.

[34] B. B. Owens and G. R. Argue. High-conductivity solid electrolytes - mag4i5. Science, 157(3786):308–&, 1967.

[35] J. N. Bradley and P. D. Greene. Solids with high ionic conductivity in group 1 halide systems. Transactions of the Faraday Society, 63(530P):424–, 1967.

[36] Y. F. Y. Yao and J. T. Kummer. Ion exchange properties of and rates of ionic diffusion in beta-alumina. Journal of Inorganic & Nuclear Chemistry, 29(9):2453–&, 1967.

[37] Walther Nernst. Electric glow-lamp., August 11 1914. US Patent 1,106,960.

[38] Werner Jundt and Rolf Reischl. Method and apparatus for controlling the air-fuel ratio of the operating mixture of an internal combustion engine, July 16 1985. US Patent 4,528,957.

[39] Lesley E Smart and Elaine A Moore. Solid state chemistry: an introduction. CRC press, 2012.

[40] Joseph T Kummer and Neill Weber. A sodium-sulfur secondary battery. Technical report, SAE Technical Paper, 1967.

[41] D. C. Ginnings and T. E. Phipps. Temperature-conductance curves of solid salts. iii. halides of lithium. Journal of the American Chemical Society, 52:1340–1345, 1930.

[42] W Greatbatch and R Mead. Lithium iodine battery, June 18 1974. US Patent 3,817,791.

[43] B. W. Faughnan and R. S. Crandall. Electrochromic displays based on wo3. Topics in Applied Physics, 40:181–211, 1980.

[44] J. M. Tarascon and M. Armand. Issues and challenges facing rechargeable lithium batteries. Nature, 414(6861):359–367, 2001.

[45] Andre Schwoebel, Rene Hausbrand, and Wolfram Jaegermann. Interface reactions between lipon and lithium studied by in-situ x-ray photoemission. Solid State Ionics, 273:51–54, 2015.

[46] Yizhou Zhu, Xingfeng He, and Yifei Mo. Origin of outstanding stability in the lithium solid electrolyte materials: Insights from thermodynamic analyses based on first-principles calculations. ACS applied materials & interfaces, 7(42):23685–23693, 2015.

[47] R. C. Agrawal and G. P. Pandey. Solid polymer electrolytes: materials designing and all-solid-state battery applications: an overview. Journal of Physics D-Applied Physics, 41(22), 2008.

[48] A. Aboulaich, R. Bouchet, G. Delaizir, V. Seznec, L. Tortet, M. Morcrette, P. Rozier, J. M. Tarascon, V. Viallet, and M. Dolle. A new approach to develop safe all-inorganic monolithic li-ion batteries. Advanced Energy Materials, 1(2):179–183, 2011.

[49] G. C. Farrington and J. L. Briant. Fast ionic transport in solids. Science, 204(4400):1371–1379, 1979.

[50] Yuki Kato, Satoshi Hori, Toshiya Saito, Kota Suzuki, Masaaki Hirayama, Akio Mitsui, Masao Yonemura, Hideki Iba, and Ryoji Kanno. High-power all-solid-state batteries using sulfide superionic conductors. Nature Energy, 1:16030, 2016.

[51] Allen J Bard, Larry R Faulkner, Johna Leddy, and Cynthia G Zoski. Electrochemical methods: fundamentals and applications, volume 2. Wiley New York, 1980.

[52] M. D. Ingram, C. T. Moynihan, and A. V. Lesikar. Ionic-conductivity and the weak electrolyte theory of glass. Journal of Non-Crystalline Solids, 38-9(MAY-):371–376, 1980.

[53] Maciej Galiski, Andrzej Lewandowski, and Izabela Stepniak. Ionic liquids as electrolytes. Electrochimica Acta, 51(26):5567–5580, 2006.

[54] M. Ribes, B. Barrau, and J. L. Souquet. Sulfide glasses - glass forming region, structure and ionic-conduction of glasses in na2s-sis2, na2s-ges2, na2s-p2s5 and li2s-ges2 systems. Journal of Non-Crystalline Solids, 38-9(MAY-):271–276, 1980.

[55] Ren Mercier, Jean-Pierre Malugani, Bernard Fahys, and Guy Robert. Superionic conduction in li2s-p2s5-lii-glasses. Solid State Ionics, 5:663–666, 1981.

[56] H Wada, M Menetrier, A Levasseur, and P Hagenmuller. Preparation and ionic conductivity of new b2s3-li2s-lii glasses. Materials research bulletin, 18(2):189–193, 1983.

[57] A. Hayashi, S. Hama, H. Morimoto, M. Tatsumisago, and T. Minami. High lithium ion conductivity of glass-ceramics derived from mechanically milled glassy powders. Chemistry Letters, (9):872–873, 2001.

[58] M. J. G. Jak, E. M. Kelder, M. Stuivinga, and J. Schoonman. Dynamically compacted rechargeable ceramic lithium batteries. Solid State Ionics, 86-8:897–902, 1996.

[59] K. Takada, N. Aotani, K. Iwamoto, and S. Kondo. Solid state lithium battery with oxysulfide glass. Solid State Ionics, 86-8:877–882, 1996.

[60] Akitoshi Hayashi, Hideki Yamashita, Masahiro Tatsumisago, and Tsutomu Minami. Characterization of li 2 s–sis 2–li x mo y (m= si, p, ge) amorphous solid electrolytes prepared by melt-quenching and mechanical milling. Solid State Ionics, 148(3):381–389, 2002.

[61] Nobuya Machida, Yuki Yoneda, and Toshihiko Shigematsu. Mechano-chemical synthesis of lithium ion conducting materials in the system li2o-li2s-p2s5. , 51(2):91–97, 2004.

[62] H. Morimoto, H. Yamashita, M. Tatsumisago, and T. Minami. Mechanochemical synthesis of new amorphous materials of 60li(2)s center dot 40sis(2) with high lithium ion conductivity. Journal of the American Ceramic Society, 82(5):1352–1354, 1999.

[63] J. H. Kennedy, S. Sahami, S. W. Shea, and Z. M. Zhang. Preparation and conductivity measurements of sis2-li2s glasses doped with libr and licl. Solid State Ionics, 18-9:368–371, 1986.

[64] Noboru Aotani, Kazuya Iwamoto, Kazunori Takada, and Shigeo Kondo. Synthesis and electrochemical properties of lithium ion conductive glass, li 3 po 4 li 2 s sis 2. Solid State Ionics, 68(1):35–39, 1994.

[65] M. Tachez, J. P. Malugani, R. Mercier, and G. Robert. Ionic-conductivity of and phase-transition in lithium thiophosphate li3ps4. Solid State Ionics, 14(3):181–185, 1984.

[66] Z. C. Liu, W. J. Fu, E. A. Payzant, X. Yu, Z. L. Wu, N. J. Dudney, J. Kiggans, K. L. Hong, A. J. Rondinone, and C. D. Liang. Anomalous high ionic conductivity of nanoporous beta-li3ps4. Journal of the American Chemical Society, 135(3):975–978, 2013.

[67] Ryoji Kanno, Takayuki Hata, Yoji Kawamoto, and Michihiko Irie. Synthesis of a new lithium ionic conductor, thio-lisicon–lithium germanium sulfide system. Solid State Ionics, 130(1):97–104, 2000.

[68] T. Kaib, S. Haddadpour, M. Kapitein, P. Bron, C. Schroder, H. Eckert, B. Roling, and S. Dehnen. New lithium chalcogenidotetrelates, licht: Synthesis and characterization of the li+-conducting tetralithium ortho-sulfidostannate li4sns4. Chemistry of Materials, 24(11):2211–2219, 2012.

[69] R. Kanno and M. Maruyama. Lithium ionic conductor thio-lisicon - the li2s-ges2-p2s5 system. Journal of the Electrochemical Society, 148(7):A742–A746, 2001.

[70] F. Mizuno, A. Hayashi, K. Tadanaga, and M. Tatsumisago. New, highly ion-conductive crystals precipitated from li2s-p2s5 glasses. Advanced Materials, 17(7):918–+, 2005.

[71] S. Boulineau, M. Courty, J. M. Tarascon, and V. Viallet. Mechanochemical synthesis of li-argyrodite li6ps5x (x = cl, br, i) as sulfur-based solid electrolytes for all solid state batteries application. Solid State Ionics, 221:1–5, 2012.

[72] N. Kamaya, K. Homma, Y. Yamakawa, M. Hirayama, R. Kanno, M. Yonemura, T. Kamiyama, Y. Kato, S. Hama, K. Kawamoto, and A. Mitsui. A lithium superionic conductor. Nature Materials, 10(9):682–686, 2011.

[73] M. Murayama, N. Sonoyama, A. Yamada, and R. Kanno. Material design of new lithium ionic conductor, thio-lisicon, in the li2s-p2s5 system. Solid State Ionics, 170(3-4):173–180, 2004.

[74] Masahiro Tatsumisago, Yoshikane Shinkuma, and Tsutomu Minami. Stabilization of superionic α-agl at room temperature in a glass matrix. 1991.

[75] H. J. Deiseroth, S. T. Kong, H. Eckert, J. Vannahme, C. Reiner, T. Zaiss, and M. Schlosser. Li6ps5x: A class of crystalline li-rich solids with an unusually high li+ mobility. Angewandte Chemie-International Edition, 47(4):755–758, 2008.

[76] E. Rangasamy, Z. C. Liu, M. Gobet, K. Pilar, G. Sahu, W. Zhou, H. Wu, S. Greenbaum, and C. D. Liang. An iodide-based li7p2s8i superionic conductor. Journal of the American Chemical Society, 137(4):1384–1387, 2015.

[77] H. Kahnt. Ionic transport in glasses. Journal of Non-Crystalline Solids, 203:225–231, 1996.

[78] C. A. Angell. Mobile ions in amorphous solids. Annual Review of Physical Chemistry, 43:693–717, 1992.

[79] J. H. Kennedy and Z. M. Zhang. Preparation and electrochemical properties of the sis2-p2s5-li2s glass coformer system. Journal of the Electrochemical Society, 136(9):2441–2443, 1989.

[80] H. Eckert, Z. M. Zhang, and J. H. Kennedy. Structural transformation of nonoxide chalcogenide glasses - the short-range order of li2s-p2s5 glasses studied by quantitative p-31 and li-6,7 high-resolution solid-state nmr. Chemistry of Materials, 2(3):273–279, 1990.

[81] K. Hayamizu, Y. Aihara, and N. Machida. Anomalous lithium ion migration in the solid electrolyte (li2s)(7)(p2s5)(3); fast ion transfer at short time intervals studied by pgse nmr spectroscopy. Solid State Ionics, 259:59–64, 2014.

[82] Hideaki Ohtsuka, Shigeto Okada, and Jun-ichi Yamaki. Solid state battery with li2o-v2o5-sio2 solid electrolyte thin film. Solid State Ionics, 40:964–966, 1990.

[83] J. R. Akridge and H. Vourlis. Solid-state batteries using vitreous solid electrolytes. Solid State Ionics, 18-9:1082–1087, 1986.

[84] M Baba, N Kumagai, H Kobayashi, O Nakano, and K Nishidate. Fabrication and electrochemical characteristics of all-solid-state lithium-ion batteries using v 2 o 5 thin films for both electrodes. Electrochemical and solid-state letters, 2(7):320–322, 1999.

[85] Mamoru Baba, Naoaki Kumagai, H Fujita, K Ohta, K Nishidate, Shinichi Komaba, Benjamin Kaplan, Henri Groult, and Didier Devilliers. Multi-layered li-ion rechargeable batteries for a high-voltage and high-current solid-state power source. Journal of power sources, 119:914–917, 2003.

[86] D Fauteux and R Koksbang. Rechargeable lithium battery anodes: alternatives to metallic lithium. Journal of applied electrochemistry, 23(1):1–10, 1993.

[87] Minoru Inaba, Takeshi Uno, and Akimasa Tasaka. Irreversible capacity of electrodeposited sn thin film anode. Journal of power sources, 146(1):473–477, 2005.

[88] JP Maranchi, AF Hepp, and PN Kumta. High capacity, reversible silicon thin-film anodes for lithium-ion batteries. Electrochemical and solid-state letters, 6(9):A198–A201, 2003.

[89] F Alamgir, E Strauss, M DenBoer, S Greenbaum, J Whitacre, C Kao, and S Neih. Licoo2 thin-film batteries. Journal of The Electrochemical Society, 152(BNL–80712-2008-JA), 2005.

[90] NJ Dudney, JB Bates, RA Zuhr, S Young, JD Robertson, HP Jun, and SA Hackney. Nanocrystalline li x mn2- y o 4 cathodes for solid-state thin-film rechargeable lithium batteries. Journal of the Electrochemical Society, 146(7):2455–2464, 1999.

[91] F Sauvage, E Baudrin, M Morcrette, and J-M Tarascon. Pulsed laser deposition and electrochemical properties of lifepo4 thin films. Electrochemical and solid-state letters, 7(1):A15–A18, 2004.

[92] Naoaki Kuwata, Shota Kudo, Yasutaka Matsuda, and Junichi Kawamura. Fabrication of thin-film lithium batteries with 5-v-class licomno4 cathodes. Solid State Ionics, 262:165–169, 2014.

[93] JB Bates, NJ Dudney, GR Gruzalski, RA Zuhr, A Choudhury, CF Luck, and JD Robertson. Fabrication and characterization of amorphous lithium electrolyte thin films and rechargeable thin-film batteries. Journal of Power Sources, 43(1-3):103–110, 1993.

[94] Arun Patil, Vaishali Patil, Dong Wook Shin, Ji-Won Choi, Dong-Soo Paik, and Seok-Jin Yoon. Issue and challenges facing rechargeable thin film lithium batteries. Materials research bulletin, 43(8):1913–1942, 2008.

[95] NJ Dudney and BJ Neudecker. Solid state thin-film lithium battery systems. Current Opinion in Solid State and Materials Science, 4(5):479–482, 1999.

[96] K. Xu. Nonaqueous liquid electrolytes for lithium-based rechargeable batteries. Chemical Reviews, 104(10):4303–4417, 2004.

[97] Atsushi Sakuda, Akitoshi Hayashi, and Masahiro Tatsumisago. Intefacial observation between licoo2 electrode and li2s-p2s5 solid electrolytes of all-solid-state lithium secondary batteries using transmission electron microscopy. Chemistry of Materials, 22(3):949–956, 2010.

[98] Narumi Ohta, Kazunori Takada, Lianqi Zhang, Renzhi Ma, Minoru Osada, and Takayoshi Sasaki. Enhancement of the high-rate capability of solid-state lithium batteries by nanoscale interfacial modification. Advanced Materials, 18(17):2226–+, 2006.

[99] Kazuya Okada, Nobuya Machida, Muneyuki Naito, Toshihiko Shigematsu, Seitaro Ito, Satoshi Fujiki, Masatugu Nakano, and Yuichi Aihara. Preparation and electrochemical properties of lialo 2-coated li (ni 1/3 mn 1/3 co 1/3) o 2 for all-solid-state batteries. Solid State Ionics, 255:120–127, 2014.

[100] Justin M. Whiteley, Jae H. Woo, Enyuan Hu, Kyung-Wan Nam, and Se-Hee Lee. Empowering the lithium metal battery through a silicon-based superionic conductor. Journal of the Electrochemical Society, 161(12):A1812–A1817, 2014.

[101] Kazunori Takada, Narumi Ohta, Lianqi Zhang, Xiaoxiong Xu, Bui Thi Hang, Tsuyoshi Ohnishi, Minoru Osada, and Takayoshi Sasaki. Interfacial phenomena in solid-state lithium battery with sulfide solid electrolyte. Solid State Ionics, 225:594–597, 2012.

[102] Fuminori Mizuno, Akitoshi Hayashi, Kiyoharu Tadanaga, Tsutomu Minami, and Masahiro Tatsumisago. All-solid-state lithium secondary batteries using li 2 s–sis 2–li 4 sio 4 glasses and li 2 s–p 2 s 5 glass ceramics as solid electrolytes. Solid state ionics, 175(1):699–702, 2004.

[103] Bum Ryong Shin and Yoon Seok Jung. All-solid-state rechargeable lithium batteries using liti2(ps4)(3) cathode with li2s-p2s5 solid electrolyte. Journal of the Electrochemical Society, 161(1):A154–A159, 2014.

[104] J. E. Trevey, Y. S. Jung, and S. H. Lee. High lithium ion conducting li2s-ges2-p2s5 glass-ceramic solid electrolyte with sulfur additive for all solid-state lithium secondary batteries. Electrochimica Acta, 56(11):4243–4247, 2011.

[105] Joachim Maier. Ionic conduction in space charge regions. Progress in solid state chemistry, 23(3):171–263, 1995.

[106] K. Takada, N. Ohta, L. Q. Zhang, K. Fukuda, I. Sakaguchi, R. Ma, M. Osada, and T. Sasaki. Interfacial modification for high-power solid-state lithium batteries. Solid State Ionics, 179(27-32):1333–1337, 2008.

[107] Chihiro Yada, Akihiro Ohmori, Kazuto Ide, Hisatsugu Yamasaki, Takehisa Kato, Toshiya Saito, Fumihiro Sagane, and Yasutoshi Iriyama. Dielectric modification of 5v-class cathodes for high-voltage all-solid-state lithium batteries. Advanced Energy Materials, 4(9), 2014.

[108] Fudong Han, Yizhou Zhu, Xingfeng He, Yifei Mo, and Chunsheng Wang. Electrochemical stability of li10gep2s12 and li7la3zr2o12 solid electrolytes. Advanced Energy Materials, 2016.

[109] Y. S. Jung, A. S. Cavanagh, A. C. Dillon, M. D. Groner, S. M. George, and S. H. Lee. Enhanced stability of licoo2 cathodes in lithium-ion batteries using surface modification by atomic layer deposition. Journal of the Electrochemical Society, 157(1):A75–A81, 2010.

[110] Yong Jeong Kim, Jaephil Cho, Tae-Joon Kim, and Byungwoo Park. Suppression of cobalt dissolution from the licoo2 cathodes with various metal-oxide coatings. Journal of The Electrochemical Society, 150(12):A1723–A1725, 2003.

[111] Yoshikatsu Seino, Tsuyoshi Ota, and Kazunori Takada. High rate capabilities of all-solid-state lithium secondary batteries using li 4 ti 5 o 12-coated lini 0.8 co 0.15 al 0.05 o 2 and a sulfide-based solid electrolyte. Journal of Power Sources, 196(15):6488–6492, 2011.

[112] Atsushi Sakuda, Hirokazu Kitaura, Akitoshi Hayashi, Kiyoharu Tadanaga, and Masahiro Tatsumisago. All-solid-state lithium secondary batteries with oxide-coated licoo 2 electrode and li 2 s–p 2 s 5 electrolyte. Journal of Power Sources, 189(1):527–530, 2009.

[113] J. H. Woo, J. E. Trevey, A. S. Cavanagh, Y. S. Choi, S. C. Kim, S. M. George, K. H. Oh, and S. H. Lee. Nanoscale interface modification of licoo2 by al2o3 atomic layer deposition for solid-state li batteries. Journal of the Electrochemical Society, 159(7):A1120–A1124, 2012.

[114] Kazunori Takada. Interfacial nanoarchitectonics for solid-state lithium batteries. Langmuir, 29(24):7538–7541, 2013.

[115] Atsushi Sakuda, Naoyuki Nakamoto, Hirokazu Kitaura, Akitoshi Hayashi, Kiyoharu Tadanaga, and Masahiro Tatsumisago. All-solid-state lithium secondary batteries with metal-sulfide-coated licoo 2 prepared by thermal decomposition of dithiocarbamato complexes. Journal of Materials Chemistry, 22(30):15247–15254, 2012.

[116] X. L. Ji, K. T. Lee, and L. F. Nazar. A highly ordered nanostructured carbon-sulphur cathode for lithium-sulphur batteries. Nature Materials, 8(6):500–506, 2009.

[117] J. Hassoun and B. Scrosati. Moving to a solid-state configuration: A valid approach to making lithium-sulfur batteries viable for practical applications. Advanced Materials, 22(45):5198–+, 2010.

[118] M. Nagao, A. Hayashi, and M. Tatsumisago. Bulk-type lithium metal secondary battery with indium thin layer at interface between li electrode and li2s-p2s5 solid electrolyte. Electrochemistry, 80(10):734–736, 2012.

[119] M. Nagao, A. Hayashi, and M. Tatsumisago. Sulfur-carbon composite electrode for all-solid-state li/s battery with li2s-p2s5 solid electrolyte. Electrochimica Acta, 56(17):6055–6059, 2011.

[120] H. Nagata and Y. Chikusa. A lithium sulfur battery with high power density. Journal of Power Sources, 264:206–210, 2014.

[121] T. Kobayashi, Y. Imade, D. Shishihara, K. Homma, M. Nagao, R. Watanabe, T. Yokoi, A. Yamada, R. Kanno, and T. Tatsumi. All solid-state battery with sulfur electrode and thio-lisicon electrolyte. Journal of Power Sources, 182(2):621–625, 2008.

[122] M. Nagao, Y. Imade, H. Narisawa, T. Kobayashi, R. Watanabe, T. Yokoi, T. Tatsumi, and R. Kanno. All-solid-state li-sulfur batteries with mesoporous electrode and thio-lisicon solid electrolyte. Journal of Power Sources, 222:237–242, 2013.

[123] Bum Ryong Shin, Young Jin Nam, Jin Wook Kim, Young-Gi Lee, and Yoon Seok Jung. Interfacial architecture for extra li+ storage in all-solid-state lithium batteries. Scientific Reports, 4, 2014.

[124] T. A. Yersak, J. E. Trevey, and S. H. Lee. In situ lithiation of tis2 enabled by spontaneous decomposition of li3n. Journal of Power Sources, 196(22):9830–9834, 2011.

[125] Motohiro Nagao, Hirokazu Kitaura, Akitoshi Hayashi, and Masahiro Tatsumisago. High rate performance, wide temperature operation and long cyclability of all-solid-state rechargeable lithium batteries using mo-s chevrel-phase compound. Journal of The Electrochemical Society, 160(6):A819–A823, 2013.

[126] T. A. Yersak, H. A. Macpherson, S. C. Kim, V. D. Le, C. S. Kang, S. B. Son, Y. H. Kim, J. E. Trevey, K. H. Oh, C. Stoldt, and S. H. Lee. Solid state enabled reversible four electron storage. Advanced Energy Materials, 3(1):120–127, 2013.

[127] Y. S. Jung, D. Y. Oh, Y. J. Nam, and K. H. Park. Issues and challenges for bulk-type all-solid-state rechargeable lithium batteries using sulfide solid electrolytes. Israel Journal of Chemistry, 55(5):472–485, 2015.

[128] Kazunori Takada, Taro Inada, Akihisa Kajiyama, Hideki Sasaki, Shigeo Kondo, Mamoru Watanabe, Masahiro Murayama, and Ryoji Kanno. Solid-state lithium battery with graphite anode. Solid State Ionics, 158(3):269–274, 2003.

[129] Tomonari Takeuchi, Hiroyuki Kageyama, Koji Nakanishi, Toshiaki Ohta, Atsushi Sakuda, Hikari Sakaebe, Hironori Kobayashi, Kuniaki Tatsumi, and Zempachi Ogumi. Rapid preparation of li2s-p2s5 solid electrolyte and its application for graphite/li2s all-solid-state lithium secondary battery. ECS Electrochemistry Letters, 3(5):A31–A35, 2014.

[130] Kiyoshi Kanamura, Nao Akutagawa, and Kaoru Dokko. Three dimensionally ordered composite solid materials for all solid-state rechargeable lithium batteries. Journal of power sources, 146(1):86–89, 2005.

[131] Yuji Hashimoto, Nobuya Machida, and Toshihiko Shigematsu. Preparation of li 4.4 ge x si 1-x alloys by mechanical milling process and their properties as anode materials in all-solid-state lithium batteries. Solid State Ionics, 175(1):177–180, 2004.

[132] J. Trevey, J. S. Jang, Y. S. Jung, C. R. Stoldt, and S. H. Lee. Glass-ceramic li2s-p2s5 electrolytes prepared by a single step ball billing process and their application for all-solid-state lithium-ion batteries. Electrochemistry Communications, 11(9):1830–1833, 2009.

[133] A. Hayashi, T. Konishi, K. Tadanaga, T. Minami, and M. Tatsumisago. Preparation and characterization of sno-p2o5 glasses as anode materials for lithium secondary batteries. Journal of Non-Crystalline Solids, 345:478–483, 2004.

[134] Hirokazu Kitaura, Kenji Takahashi, Fuminori Mizuno, Akitoshi Hayashi, Kiyoharu Tadanaga, and Masahiro Tatsumisago. Preparation of α-fe2o3 electrode materials via solution process and their electrochemical properties in all-solid-state lithium batteries. Journal of The Electrochemical Society, 154(7):A725–A729, 2007.

[135] Ai Ueda, Motohiro Nagao, Akiko Inoue, Akitoshi Hayashi, Yoshikatsu Seino, Tsuyoshi Ota, and Masahiro Tatsumisago. Electrochemical performance of all-solid-state lithium batteries with sn 4 p 3 negative electrode. Journal of Power Sources, 244:597–600, 2013.

[136] Yoon S Jung, Kyu T Lee, Jun H Kim, Ji Y Kwon, and Seung M Oh. Thermo-electrochemical activation of an in–cu intermetallic electrode for the anode in lithium secondary batteries. Advanced Functional Materials, 18(19):3010–3017, 2008.

[137] R. Kanno, M. Murayama, T. Inada, T. Kobayashi, K. Sakamoto, N. Sonoyama, A. Yamada, and S. Kondo. A self-assembled breathing interface for all-solid-state ceramic lithium batteries. Electrochemical and Solid State Letters, 7(12):A455–A458, 2004.

[138] P. G. Bruce, S. A. Freunberger, L. J. Hardwick, and J. M. Tarascon. Li-o-2 and li-s batteries with high energy storage. Nature Materials, 11(1):19–29, 2012.

[139] D. Aurbach, E. Zinigrad, Y. Cohen, and H. Teller. A short review of failure mechanisms of lithium metal and lithiated graphite anodes in liquid electrolyte solutions. Solid State Ionics, 148(3-4):405–416, 2002.

[140] M. Nagao, A. Hayashi, M. Tatsumisago, T. Kanetsuku, T. Tsuda, and S. Kuwabata. In situ sem study of a lithium deposition and dissolution mechanism in a bulk-type solid-state cell with a li2s-p2s5 solid electrolyte. Physical Chemistry Chemical Physics, 15(42):18600–18606, 2013.

[141] B. R. Shin, Y. J. Nam, D. Y. Oh, D. H. Kim, J. W. Kim, and Y. S. Jung. Comparative study of tis2/li-in all-solid-state lithium batteries using glass-ceramic li3ps4 and li10gep2s12 solid electrolytes. Electrochimica Acta, 146:395–402, 2014.

[142] Gayatri Sahu, Zhan Lin, Juchuan Li, Zengcai Liu, Nancy Dudney, and Chengdu Liang. Air-stable, high-conduction solid electrolytes of arsenic-substituted li 4 sns 4. Energy & Environmental Science, 7(3):1053–1058, 2014.

[143] P Balasubramanian, M Marinaro, S Theil, M Wohlfahrt-Mehrens, and L Jörissen. Au-coated carbon electrodes for aprotic li–o 2 batteries with extended cycle life: The key issue of the li-ion source. Journal of Power Sources, 278:156–162, 2015.

[144] T. R. Jow and C. C. Liang. Interface between solid anode and solid electrolyte-effect of pressure on li/lii(al2o3) interface. Solid State Ionics, 9-10(DEC):695–698, 1983.

[145] M. Meyer, H. Rickert, and U. Schwaitzer. Investigations on the kinetics of the anodic-dissolution of lithium at the interface li/li3n. Solid State Ionics, 9-10(DEC):689–693, 1983.

[146] J. Janek and S. Majoni. Investigation of charge-transport across the ag-vertical-bar-agi-interface .1. occurrence of periodic phenomena during anodic-dissolution of silver. Berichte Der Bunsen-Gesellschaft-Physical Chemistry Chemical Physics, 99(1):14–20, 1995.

[147] S. Majoni and J. Janek. Periodic electrochemical oscillations at a solid-solid electrode. Solid State Ionics, 85(1-4):247–250, 1996.

[148] T. R. Jow and C. C. Liang. Interface between solid electrode and solid electrolyte - a study of the li/lil(al2o3) solid-electrolyte system. Journal of the Electrochemical Society, 130(4):737–740, 1983.

[149] Atsushi Sakuda, Akitoshi Hayashi, Takamasa Ohtomo, Shigenori Hama, and Masahiro Tatsumisago. Licoo2 electrode particles coated with li2s–p2s5 solid electrolyte for all-solid-state batteries. Electrochemical and Solid-State Letters, 13(6):A73–A75, 2010.

[150] S. Teragawa, K. Aso, K. Tadanaga, A. Hayashi, and M. Tatsumisago. Preparation of li2s-p2s5 solid electrolyte from n-methylformamide solution and application for all-solid-state lithium battery. Journal of Power Sources, 248:939–942, 2014.

[151] Y. M. Wang, Z. Q. Liu, X. L. Zhu, Y. F. Tang, and F. Q. Huang. Highly lithium-ion conductive thio-lisicon thin film processed by low-temperature solution method. Journal of Power Sources, 224:225–229, 2013.

[152] Y. Seino, T. Ota, K. Takada, A. Hayashi, and M. Tatsumisago. A sulphide lithium super ion conductor is superior to liquid ion conductors for use in rechargeable batteries. Energy & Environmental Science, 7(2):627–631, 2014.

[153] A. Sakuda, A. Hayashi, and M. Tatsumisago. Sulfide solid electrolyte with favorable mechanical property for all-solid-state lithium battery. Scientific Reports, 3, 2013.

[154] H. Kitaura, A. Hayashi, T. Ohtomo, S. Hama, and M. Tatsumisago. Fabrication of electrode-electrolyte interfaces in all-solid-state rechargeable lithium batteries by using a supercooled liquid state of the glassy electrolytes. Journal of Materials Chemistry, 21(1):118–124, 2011.

[155] Y. Idota, T. Kubota, A. Matsufuji, Y. Maekawa, and T. Miyasaka. Tin-based amorphous oxide: A high-capacity lithium-ion-storage material. Science, 276(5317):1395–1397, 1997.

[156] G. C. Kuczynski. Study of the sintering of glass. Journal of Applied Physics, 20(12):1160–1163, 1949.

[157] C. M. Park, J. H. Kim, H. Kim, and H. J. Sohn. Li-alloy based anode materials for li secondary batteries. Chemical Society Reviews, 39(8):3115–3141, 2010.

[158] G. R. Goward, N. J. Taylor, D. C. S. Souza, and L. F. Nazar. The true crystal structure of li17m4 (m=ge, sn, pb)-revised from li22m5. Journal of Alloys and Compounds, 329(1-2):82–91, 2001.

[159] A. Anani, S. Crouchbaker, and R. A. Huggins. Kinetic and thermodynamic parameters of several binary lithium alloy negative electrode materials at ambient-temperature. Journal of the Electrochemical Society, 134(12):3098–3102, 1987.

[160] O. Mao, R. A. Dunlap, and J. R. Dahn. Mechanically alloyed sn-fe(-c) powders as anode materials for li-ion batteries - i. the sn2fe-c system. Journal of the Electrochemical Society, 146(2):405–413, 1999.

[161] S. Yoon, J. M. Lee, H. Kim, D. M. Im, S. G. Doo, and H. J. Sohn. An sn-fe/carbon nanocomposite as an alternative anode material for rechargeable lithium batteries. Electrochimica Acta, 54(10):2699–2705, 2009.

[162] O. Crosnier, T. Brousse, X. Devaux, P. Fragnaud, and D. M. Schleich. New anode systems for lithium ion cells. Journal of Power Sources, 94(2):169–174, 2001.

[163] J. Hassoun, S. Panero, and B. Scrosati. Electrodeposited ni-sn intermetallic electrodes for advanced lithium ion batteries. Journal of Power Sources, 160(2):1336–1341, 2006.

[164] L. Huang, H. B. Wei, F. S. Ke, X. Y. Fan, J. T. Li, and S. G. Sun. Electrodeposition and lithium storage performance of three-dimensional porous reticular sn-ni alloy electrodes. Electrochimica Acta, 54(10):2693–2698, 2009.

[165] I. A. Courtney and J. R. Dahn. Electrochemical and in situ x-ray diffraction studies of the reaction of lithium with tin oxide composites. Journal of the Electrochemical Society, 144(6):2045–2052, 1997.

[166] J. T. Vaughey, J. O'Hara, and M. M. Thackeray. Intermetallic insertion electrodes with a zinc blende-type structure for li batteries: A study of lixinsb (0 ¡= x ¡= 3). Electrochemical and Solid State Letters, 3(1):13–16, 2000.

[167] D. M. Piper, T. A. Yersak, and S. H. Lee. Effect of compressive stress on electrochemical performance of silicon anodes. Journal of the Electrochemical Society, 160(1):A77–A81, 2013.

[168] T. A. Yersak, T. Evans, J. M. Whiteley, S. B. Son, B. Francisco, K. H. Oh, and S. H. Lee. Derivation of an iron pyrite all-solid-state composite electrode with ferrophosphorus, sulfur, and lithium sulfide as precursors. Journal of the Electrochemical Society, 161(5):A663–A667, 2014.

[169] M. Tatsumisago, F. Mizuno, and A. Hayashi. All-solid-state lithium secondary batteries using sulfide-based glass-ceramic electrolytes. Journal of Power Sources, 159(1):193–199, 2006.

[170] A. Hayashi, T. Konishi, K. Tadanaga, T. Minami, and M. Tatsumisago. All-solid-state lithium secondary batteries with sns-p2s5 negative electrodes and li2s-p2s5 solid electrolytes. Journal of Power Sources, 146(1-2):496–500, 2005.

[171] T. A. Yersak, S. B. Son, J. S. Cho, S. S. Suh, Y. U. Kim, J. T. Moon, K. H. Oh, and S. H. Lee. An all-solid-state li-ion battery with a pre-lithiated si-ti-ni alloy anode. Journal of the Electrochemical Society, 160(9):A1497–A1501, 2013.

[172] T. Inada, K. Takada, A. Kajiyama, H. Sasaki, S. Kondo, M. Watanabe, M. Murayama, and R. Kanno. Silicone as a binder in composite electrolytes. Journal of Power Sources, 119:948–950, 2003.

[173] Justin M. Whiteley, Ji Woo Kim, Chan Soon Kang, Jong Soo Cho, Kyu Hwan Oh, and Se-Hee Lee. Tin networked electrode providing enhanced volumetric capacity and pressureless operation for all-solid-state li-ion batteries. Journal of the Electrochemical Society, 162(4):A711–A715, 2015.

[174] M. Winter and J. O. Besenhard. Electrochemical lithiation of tin and tin-based intermetallics and composites. Electrochimica Acta, 45(1-2):31–50, 1999.

[175] C. Lupu, J. G. Mao, J. W. Rabalais, A. M. Guloy, and J. W. Richardson. X-ray and neutron diffraction studies on "li4.4sn". Inorganic Chemistry, 42(12):3765–3771, 2003.

[176] N. Tamura, R. Ohshita, M. Fujimoto, S. Fujitani, M. Kamino, and I. Yonezu. Study on the anode behavior of sn and sn-cu alloy thin-film electrodes. Journal of Power Sources, 107(1):48–55, 2002.

[177] H. Tavassol, J. W. Buthker, G. A. Ferguson, L. A. Curtiss, and A. A. Gewirth. Solvent oligomerization during sei formation on model systems for li-ion battery anodes. Journal of the Electrochemical Society, 159(6):A730–A738, 2012.

[178] I. A. Courtney, J. S. Tse, O. Mao, J. Hafner, and J. R. Dahn. Ab initio calculation of the lithium-tin voltage profile. Physical Review B, 58(23):15583–15588, 1998.

[179] D. M. Piper, T. A. Yersak, S. B. Son, S. C. Kim, C. S. Kang, K. H. Oh, C. M. Ban, A. C. Dillon, and S. H. Lee. Conformal coatings of cyclized-pan for mechanically resilient si nano-composite anodes. Advanced Energy Materials, 3(6):697–702, 2013.

[180] H. Mukaibo, T. Momma, Y. Shacham-Diamand, T. Osaka, and M. Kodaira. In situ stress transition observations of electrodeposited sn-based anode materials for lithium-ion secondary batteries. Electrochemical and Solid State Letters, 10(3):A70–A73, 2007.

[181] J. R. Dahn, I. A. Courtney, and O. Mao. Short-range sn ordering and crystal structure of li4.4sn prepared by ambient temperature electrochemical methods. Solid State Ionics, 111(3-4):289–294, 1998.

[182] S. B. Son, S. C. Kim, C. S. Kang, T. A. Yersak, Y. C. Kim, C. G. Lee, S. H. Moon, J. S. Cho, J. T. Moon, K. H. Oh, and S. H. Lee. A highly reversible nano-si anode enabled by mechanical confinement in an electrochemically activated lixti4ni4si7 matrix. Advanced Energy Materials, 2(10):1226–1231, 2012.

[183] J. E. Trevey, K. W. Rason, C. R. Stoldt, and S. H. Lee. Improved performance of all-solid-state lithium-ion batteries using nanosilicon active material with multiwalled-carbon-nanotubes as a conductive additive. Electrochemical and Solid State Letters, 13(11):A154–A157, 2010.

[184] T. D. Hatchard and J. R. Dahn. In situ xrd and electrochemical study of the reaction of lithium with amorphous silicon. Journal of the Electrochemical Society, 151(6):A838–A842, 2004.

[185] Justin M Whiteley, Ji Woo Kim, Daniela Molina Piper, and Se-Hee Lee. High-capacity and highly reversible silicon-tin hybrid anode for solid-state lithium-ion batteries. Journal of The Electrochemical Society, 163(2):A251–A254, 2016.

[186] Wei-Jun Zhang. Lithium insertion/extraction mechanism in alloy anodes for lithium-ion batteries. Journal of Power Sources, 196(3):877–885, 2011.

[187] M. N. Obrovac and L. Christensen. Structural changes in silicon anodes during lithium insertion/extraction. Electrochemical and Solid State Letters, 7(5):A93–A96, 2004.

[188] Yadong Wang and Jeff Dahn. Phase changes in electrochemically lithiated silicon at elevated temperature. Journal of the Electrochemical Society, 153(12):A2314–A2318, 2006.

[189] P. Limthongkul, Y. I. Jang, N. J. Dudney, and Y. M. Chiang. Electrochemically-driven solid-state amorphization in lithium-metal anodes. Journal of Power Sources, 119:604–609, 2003.

[190] V. L. Chevrier, H. M. Dahn, and J. R. Dahn. Activation energies of crystallization events in electrochemically lithiated silicon. Journal of the Electrochemical Society, 158(11):A1207–A1213, 2011.

[191] S. F. Pugh. Relations between the elastic moduli and the plastic properties of polycrystalline pure metals. Philosophical Magazine, 45(367):823–843, 1954.

[192] M. Armand and J. M. Tarascon. Building better batteries. Nature, 451(7179):652–657, 2008.

[193] J. R. Dahn, E. W. Fuller, M. Obrovac, and U. Vonsacken. Thermal-stability of lixcoo2, lixnio2 and lambda-mno2 and consequences for the safety of li-ion cells. Solid State Ionics, 69(3-4):265–270, 1994.

[194] S. Tobishima and J. Yamaki. A consideration of lithium cell safety. Journal of Power Sources, 81:882–886, 1999.

[195] Z. Lin, Z. C. Liu, N. J. Dudney, and C. D. Liang. Lithium superionic sulfide cathode for all-solid lithium-sulfur batteries. Acs Nano, 7(3):2829–2833, 2013.

[196] P. Bron, S. Johansson, K. Zick, J. S. auf der Gunne, S. Dehnen, and B. Roling. Li10snp2s12: An affordable lithium superionic conductor. Journal of the American Chemical Society, 135(42):15694–15697, 2013.

[197] A. Hayashi, S. Hama, F. Mizuno, K. Tadanaga, T. Minami, and M. Tatsumisago. Characterization of li2s-p2s5 glass-ceramics as a solid electrolyte for lithium secondary batteries. Solid State Ionics, 175(1-4):683–686, 2004.

[198] S. P. Ong, Y. F. Mo, W. D. Richards, L. Miara, H. S. Lee, and G. Ceder. Phase stability, electrochemical stability and ionic conductivity of the li10 +/- 1mp2x12 (m = ge, si, sn, al or p, and x = o, s or se) family of superionic conductors. Energy & Environmental Science, 6(1):148–156, 2013.

[199] B. T. Ahn and R. A. Huggins. Synthesis and lithium conductivities of li2sis3 and li4sis4. Materials Research Bulletin, 24(7):889–897, 1989.

[200] J. H. Kennedy. Ionically conductive glasses based on sis2. Materials Chemistry and Physics, 23(1-2):29–50, 1989.

[201] S. Kondo, K. Takada, and Y. Yamamura. New lithium ion conductors based on li2s-sis2 system. Solid State Ionics, 53:1183–1186, 1992.

[202] K. Hirai, M. Tatsumisago, and T. Minami. Thermal and electrical-properties of rapidly quenched glasses in the systems li2s-sis2-li(x)mo(y)(li(x)mo(y)=li4sio4,li2so4). Solid State Ionics, 78(3-4):269–273, 1995.

[203] M. Tatsumisago, K. Hirai, T. Minami, and M. Takahashi. Preparation and characterisation of superionic li2s-sis2-li4geo4 glasses. Physics and Chemistry of Glasses, 38(2):63–65, 1997.

[204] M. Murayama, R. Kanno, M. Irie, S. Ito, T. Hata, N. Sonoyama, and Y. Kawamoto. Synthesis of new lithium ionic conductor thio-lisicon - lithium silicon sulfides system. Journal of Solid State Chemistry, 168(1):140–148, 2002.

[205] Alexander Kuhn, Oliver Gerbig, Changbao Zhu, Frank Falkenberg, Joachim Maier, and Bettina V. Lotsch. A new ultrafast superionic li-conductor: ion dynamics in li11si2ps12 and comparison with other tetragonal lgps-type electrolytes. Physical Chemistry Chemical Physics, 16(28):14669–14674, 2014.

[206] A. Kuhn, V. Duppel, and B. V. Lotsch. Tetragonal li10gep2s12 and li7geps8 - exploring the li ion dynamics in lgps li electrolytes. Energy & Environmental Science, 6(12):3548–3552, 2013.

[207] J. Hassoun, R. Verrelli, P. Reale, S. Panero, G. Mariotto, S. Greenbaum, and B. Scrosati. A structural, spectroscopic and electrochemical study of a lithium ion conducting li10gep2s12 solid electrolyte. Journal of Power Sources, 229:117–122, 2013.

[208] Y. F. Mo, S. P. Ong, and G. Ceder. First principles study of the li10gep2s12 lithium super ionic conductor material. Chemistry of Materials, 24(1):15–17, 2012.

[209] L. A. Riley, S. Van Ana, A. S. Cavanagh, Y. F. Yan, S. M. George, P. Liu, A. C. Dillon, and S. H. Lee. Electrochemical effects of ald surface modification on combustion synthesized lini1/3mn1/3co1/3o2 as a layered-cathode material. Journal of Power Sources, 196(6):3317–3324, 2011.

[210] P. Hartmann, T. Leichtweiss, M. R. Busche, M. Schneider, M. Reich, J. Sann, P. Adelhelm, and J. Janek. Degradation of nasicon-type materials in contact with lithium metal: Formation of mixed conducting interphases (mci) on solid electrolytes. Journal of Physical Chemistry C, 117(41):21064–21074, 2013.

[211] J. B. Goodenough and Y. Kim. Challenges for rechargeable li batteries. Chemistry of Materials, 22(3):587–603, 2010.

[212] M. Kotobuki, H. Munakata, K. Kanamura, Y. Sato, and T. Yoshida. Compatibility of li7la3zr2o12 solid electrolyte to all-solid-state battery using li metal anode. Journal of the Electrochemical Society, 157(10):A1076–A1079, 2010.

[213] P. Knauth. Inorganic solid li ion conductors: An overview. Solid State Ionics, 180(14-16):911–916, 2009.

[214] J. E. Ni, E. D. Case, J. S. Sakamoto, E. Rangasamy, and J. B. Wolfenstine. Room temperature elastic moduli and vickers hardness of hot-pressed llzo cubic garnet. Journal of Materials Science, 47(23):7978–7985, 2012.

[215] F. Mizuno, S. Hama, A. Hayashi, K. Tadanaga, T. Minami, and M. Tatsumisago. All solid-state lithium secondary batteries using high lithium ion conducting li2s-p2s5 glass-ceramics. Chemistry Letters, (12):1244–1245, 2002.

[216] T. Inada, K. Takada, A. Kajiyama, M. Kouguchi, H. Sasaki, S. Kondo, M. Watanabe, M. Murayama, and R. Kanno. Fabrications and properties of composite solid-state electrolytes. Solid State Ionics, 158(3-4):275–280, 2003.

[217] A. Sakuda, A. Hayashi, T. Ohtomo, S. Hama, and M. Tatsumisago. All-solid-state lithium secondary batteries using licoo2 particles with pulsed laser deposition coatings of li2s-p2s5 solid electrolytes. Journal of Power Sources, 196(16):6735–6741, 2011.

[218] M. Ogawa, R. Kanda, K. Yoshida, T. Uemura, and K. Harada. High-capacity thin film lithium batteries with sulfide solid electrolytes. Journal of Power Sources, 205:487–490, 2012.

[219] T. Uemura, K. Goto, M. Ogawa, and K. Harada. All-solid secondary batteries with sulfide-based thin film electrolytes. Journal of Power Sources, 240:510–514, 2013.

[220] S. S. Berbano, M. Mirsaneh, M. T. Lanagan, and C. A. Randall. Lithium thiophosphate glasses and glass-ceramics as solid electrolytes: Processing, microstructure, and properties. International Journal of Applied Glass Science, 4(4):414–425, 2013.

[221] Justin M. Whiteley, Philip Taynton, Wei Zhang, and Se-Hee Lee. Ultra-thin solid-state li-ion electrolyte membrane facilitated by a self-healing polymer matrix. Advanced Materials, 27(43):6922–+, 2015.

[222] Guangxi Dong, Hongyu Li, and Vicki Chen. Challenges and opportunities for mixed-matrix membranes for gas separation. Journal of Materials Chemistry A, 1(15):4610–4630, 2013.

[223] S. J. Rowan, S. J. Cantrill, G. R. L. Cousins, J. K. M. Sanders, and J. F. Stoddart. Dynamic covalent chemistry. Angewandte Chemie-International Edition, 41(6):898–952, 2002.

[224] Yinghua Jin, Chao Yu, Ryan J. Denman, and Wei Zhang. Recent advances in dynamic covalent chemistry. Chemical Society Reviews, 42(16):6634–6654, 2013.

[225] M. Capelot, D. Montarnal, F. Tournilhac, and L. Leibler. Metal-catalyzed transesterification for healing and assembling of thermosets. Journal of the American Chemical Society, 134(18):7664–7667, 2012.

[226] Philip Taynton, Kai Yu, Richard K. Shoemaker, Yinghua Jin, H. Jerry Qi, and Wei Zhang. Heat- or water-driven malleability in a highly recyclable covalent network polymer. Advanced Materials, 26(23):3938–3942, 2014.

[227] K. Minami, A. Hayashi, and M. Tatsumisago. Preparation and characterization of lithium ion conducting li2s-p2s5-ges2 glasses and glass-ceramics. Journal of Non-Crystalline Solids, 356(44-49):2666–2669, 2010.

[228] T. A. Yersak, C. Stoldt, and S. H. Lee. Electrochemical evolution of an iron sulfide and sulfur based cathode for all-solid-state li-ion batteries. Journal of the Electrochemical Society, 160(8):A1009–A1015, 2013.

[229] J. L. Barton and J. O. Bockris. Electrolytic growth of dendrites from ionic solutions. Proceedings of the Royal Society of London Series a-Mathematical and Physical Sciences, 268(1335):485–&, 1962.

[230] J. W. Diggle, A. R. Despic, and J. O. Bockris. Mechanism of dendritic electrocrystallization of zinc. Journal of the Electrochemical Society, 116(11):1503–&, 1969.

[231] J. Yamaki, S. Tobishima, K. Hayashi, K. Saito, Y. Nemoto, and M. Arakawa. A consideration of the morphology of electrochemically deposited lithium in an organic electrolyte. Journal of Power Sources, 74(2):219–227, 1998.

[232] C. Monroe and J. Newman. The impact of elastic deformation on deposition kinetics at lithium/polymer interfaces. Journal of the Electrochemical Society, 152(2):A396–A404, 2005.

[233] M. Nagao, A. Hayashi, and M. Tatsumisago. Fabrication of favorable interface between sulfide solid electrolyte and li metal electrode for bulk-type solid-state li/s battery. Electrochemistry Communications, 22:177–180, 2012.

[234] Y. Y. Ren, Y. Shen, Y. H. Lin, and C. W. Nan. Direct observation of lithium dendrites inside garnet-type lithium-ion solid electrolyte. Electrochemistry Communications, 57:27–30, 2015.

[235] M. Motoyama, M. Ejiri, and Y. Iriyama. In-situ electron microscope observations of electrochemical li deposition/dissolution with a lipon electrolyte. Electrochemistry, 82(5):364–368, 2014.

[236] H. E. Park, C. H. Hong, and W. Y. Yoon. The effect of internal resistance on dendritic growth on lithium metal electrodes in the lithium secondary batteries. Journal of Power Sources, 178(2):765–768, 2008.

[237] Taro Inada, Takeshi Kobayashi, Noriyuki Sonoyama, Atsuo Yamada, Shigeo Kondo, Miki Nagao, and Ryoji Kanno. All solid-state sheet battery using lithium inorganic solid electrolyte, thio-lisicon. Journal of Power Sources, 194(2):1085–1088, 2009.

[238] Z. Q. Wang, M. S. Wu, G. Liu, X. L. Lei, B. Xu, and C. Y. Ouyang. Elastic properties of new solid state electrolyte material li10gep2s12: A study from first-principles calculations. International Journal of Electrochemical Science, 9(2):562–568, 2014.

[239] Fudong Han, Tao Gao, Yujie Zhu, Karen J. Gaskell, and Chunsheng Wang. A battery made from a single material. Advanced Materials, 27(23):3473–3483, 2015.

[240] Bruce D Katz, Lutgard C De Jonghe, May-Ying Chu, and Steven J Visco. Positive electrodes comprising active-sulfur material of 1st and 2nd group sulfides, polysulfides, and a second material of higher discharge rate than active sulfur is oxidizable by in situ redox reaction with first, contains metal sulfide, March 13 2001. US Patent 6,200,704.

[241] Lijun Bai, Changming Li, Anaba A Anani, George Thomas, Han Wu, Ke Keryn Lian, Frank R Denton III, and Jason N Howard. Battery and capacitor, April 28 1998. US Patent 5,744,258.

[242] Z. W. Seh, J. H. Yu, W. Y. Li, P. C. Hsu, H. T. Wang, Y. M. Sun, H. B. Yao, Q. F. Zhang, and Y. Cui. Two-dimensional layered transition metal disulphides for effective encapsulation of high-capacity lithium sulphide cathodes. Nature Communications, 5, 2014.

[243] D. Marmorstein, T. H. Yu, K. A. Striebel, F. R. McLarnon, J. Hou, and E. J. Cairns. Electrochemical performance of lithium/sulfur cells with three different polymer electrolytes. Journal of Power Sources, 89(2):219–226, 2000.

[244] F. Badway, A. N. Mansour, N. Pereira, J. F. Al-Sharab, F. Cosandey, I. Plitz, and G. G. Amatucci. Structure and electrochemistry of copper fluoride nanocomposites utilizing mixed conducting matrices. Chemistry of Materials, 19(17):4129–4141, 2007.

[245] R. Fong, J. R. Dahn, and C. H. W. Jones. Electrochemistry of pyrite-based cathodes for ambient-temperature lithium batteries. Journal of the Electrochemical Society, 136(11):3206–3210, 1989.

[246] V. Pele, F. Flamary, L. Bourgeois, B. Pecquenard, and F. Le Cras. Perfect reversibility of the lithium insertion in fes2: The combined effects of all-solid-state and thin film cell configurations. Electrochemistry Communications, 51:81–84, 2015.

[247] M. S. Whittingham. Electrical energy-storage and intercalation chemistry. Science, 192(4244):1126–1127, 1976.

[248] A. J. Vaccaro, T. Palanisamy, R. L. Kerr, and J. T. Maloy. Electrochemical determination of the lithium ion diffusion-coefficient in tis2. Solid State Ionics, 2(4):337–340, 1981.

[249] C. W. Lin, X. J. Zhu, J. Feng, C. Z. Wu, S. L. Hu, J. Peng, Y. Q. Guo, L. L. Peng, J. Y. Zhao, J. L. Huang, J. L. Yang, and Y. Xie. Hydrogen-incorporated tis2 ultrathin nanosheets with ultrahigh conductivity for stamp-transferrable electrodes. Journal of the American Chemical Society, 135(13):5144–5151, 2013.

[250] Justin M Whiteley, Simon Hafner, Sang Sub Han, Seul Cham Kim, Kyu Hwan Oh, and Se-Hee Lee. Fes2-imbedded mixed conducting matrix as a solid battery cathode. Advanced Energy Materials, 2016.

[251] P. P. Chin, J. Ding, J. B. Yi, and B. H. Liu. Synthesis of fes2 and fes nanoparticles by high-energy mechanical milling and mechanochemical processing. Journal of Alloys and Compounds, 390(1-2):255–260, 2005.

[252] B. G. Silbernagel. Lithium intercalation complexes of layered transition-metal dichalcogenides - nmr survey of physical-properties. Solid State Communications, 17(3):361–365, 1975.

[253] M. S. Whittingham. Chemistry of intercalation compounds - metal guests in chalcogenide hosts. Progress in Solid State Chemistry, 12(1):41–99, 1978.

[254] T. A. Yersak, Y. F. Yan, C. Stoldt, and S. H. Lee. Ambient temperature and pressure mechanochemical preparation of nano-litis2. Ecs Electrochemistry Letters, 1(1):A21–A23, 2012.

[255] R. Winter and P. Heitjans. Li+ diffusion and its structural basis in the nanocrystalline and amorphous forms of two-dimensionally ion-conducting lixtis2. Journal of Physical Chemistry B, 105(26):6108–6115, 2001.

[256] A. Jain, G. Hautier, C. J. Moore, S. P. Ong, C. C. Fischer, T. Mueller, K. A. Persson, and G. Ceder. A high-throughput infrastructure for density functional theory calculations. Computational Materials Science, 50(8):2295–2310, 2011.

[257] W. Weppner and R. A. Huggins. Determination of kinetic-parameters of mixed-conducting electrodes and application to system li3sb. Journal of the Electrochemical Society, 124(10):1569–1578, 1977.

[258] C. J. Wen, B. A. Boukamp, R. A. Huggins, and W. Weppner. Thermodynamic and mass-transport properties of lial. Journal of the Electrochemical Society, 126(12):2258–2266, 1979.

[259] S. B. Son, T. A. Yersak, D. M. Piper, S. C. Kim, C. S. Kang, J. S. Cho, S. S. Suh, Y. U. Kim, K. H. Oh, and S. H. Lee. A stabilized pan-fes2 cathode with an ec/dec liquid electrolyte. Advanced Energy Materials, 4(3), 2014.

[260] Tyler Evans, Daniela Molina Piper, Seul Cham Kim, Sang Sub Han, Vinay Bhat, Kyu Hwan Oh, and Se-Hee Lee. Ionic liquid enabled fes2 for high-energy-density lithium-ion batteries. Advanced Materials, 26(43):7386–7392, 2014.

[261] E. Kendrick, J. Barker, J. Bao, and A. Swiatek. The rate characteristics of lithium iron sulfide. Journal of Power Sources, 196(16):6929–6933, 2011.

[262] R. Brec, A. Dugast, and A. Lemehaute. Chemical and electrochemical study of the lixfes2 cathodic system (0 less-than x less-than-or-equal-to 2). Materials Research Bulletin, 15(5):619–625, 1980.

[263] A. Van der Ven, J. Bhattacharya, and A. A. Belak. Understanding li diffusion in li-intercalation compounds. Accounts of Chemical Research, 46(5):1216–1225, 2013.

[264] H. I. Yoo, J. H. Lee, M. Martin, J. Janek, and H. Schmalzried. Experimental-evidence of the interference between ionic and electronic flows in an oxide with prevailing electronic conduction. Solid State Ionics, 67(3-4):317–322, 1994.

[265] Julius Tafel. Über die polarisation bei kathodischer wasserstoffentwicklung. Z. phys. Chem, 50:641, 1905.

[266] M. Chiku, W. Tsujiwaki, E. Higuchi, and H. Inoue. Microelectrode studies on kinetics of charge transfer at an interface of li metal and li2s-p2s5 solid electrolytes. Electrochemistry, 80(10):740–742, 2012.

[267] M. Chiku, W. Tsujiwaki, E. Higuchi, and H. Inoue. Determination of the rate-determining step in the electrochemical oxidation of li metal at the li negative electrode/li2s-p2s5 solid electrolyte interface. Journal of Power Sources, 244:675–678, 2013.

[268] Peng Bai and Martin Z. Bazant. Charge transfer kinetics at the solid-solid interface in porous electrodes. Nature Communications, 5, 2014.

[269] H. Munakata, B. Takemura, T. Saito, and K. Kanamura. Evaluation of real performance of lifepo4 by using single particle technique. Journal of Power Sources, 217:444–448, 2012.

[270] P. L. Allen and A. Hickling. Electrochemistry of sulphur .1. overpotential in the discharge of the sulphide ion. Transactions of the Faraday Society, 53(12):1626–1635, 1957.

[271] T. Abe, H. Fukuda, Y. Iriyama, and Z. Ogumi. Solvated li-ion transfer at interface between graphite and electrolyte. Journal of the Electrochemical Society, 151(8):A1120–A1123, 2004.

[272] T. Abe, F. Sagane, M. Ohtsuka, Y. Iriyama, and Z. Ogumi. Lithium-ion transfer at the interface between lithium-ion conductive ceramic electrolyte and liquid electrolyte - a key to enhancing the rate capability of lithium-ion batteries. Journal of the Electrochemical Society, 152(11):A2151–A2154, 2005.

[273] M. Gellert, K. I. Gries, J. Zakel, S. Kranz, S. Bradler, E. Hornberger, S. Muller, C. Yada, F. Rosciano, K. Volz, and B. Boling. Charge transfer across the interface between lini0.5mn1.5o4 high-voltage cathode films and solid electrolyte films. Journal of the Electrochemical Society, 162(4):A754–A759, 2015.

[274] R. A. Huggins. Supercapacitors and electrochemical pulse sources. Solid State Ionics, 134(1-2):179–195, 2000.

[275] B. E. Conway. Transition from supercapacitor to battery behavior in electrochemical energy-storage. Journal of the Electrochemical Society, 138(6):1539–1548, 1991.

[276] S. Hadzijordanov, H. Angersteinkozlowska, M. Vukovic, and B. E. Conway. Reversibility and growth-behavior of surface oxide-films at ruthenium electrodes. Journal of the Electrochemical Society, 125(9):1471–1480, 1978.

[277] T. Brezesinski, J. Wang, J. Polleux, B. Dunn, and S. H. Tolbert. Templated nanocrystal-based porous tio2 films for next-generation electrochemical capacitors. Journal of the American Chemical Society, 131(5):1802–1809, 2009.

[278] Veronica Augustyn, Jeremy Come, Michael A. Lowe, Jong Woung Kim, Pierre-Louis Taberna, Sarah H. Tolbert, Hector D. Abruna, Patrice Simon, and Bruce Dunn. High-rate electrochemical energy storage through li+ intercalation pseudocapacitance. Nature Materials, 12(6):518–522, 2013.

[279] J. W. Kim, V. Augustyn, and B. Dunn. The effect of crystallinity on the rapid pseudocapacitive response of nb2o5. Advanced Energy Materials, 2(1):141–148, 2012.

[280] K. Brezesinski, J. Wang, J. Haetge, C. Reitz, S. O. Steinmueller, S. H. Tolbert, B. M. Smarsly, B. Dunn, and T. Brezesinski. Pseudocapacitive contributions to charge storage in highly ordered mesoporous group v transition metal oxides with iso-oriented layered nanocrystalline domains. Journal of the American Chemical Society, 132(20):6982–6990, 2010.

[281] C. Lin, J. A. Ritter, and B. N. Popov. Characterization of sol-gel-derived cobalt oxide xerogels as electrochemical capacitors. Journal of the Electrochemical Society, 145(12):4097–4103, 1998.

[282] J. P. Zheng, P. J. Cygan, and T. R. Jow. Hydrous ruthenium oxide as an electrode material for electrochemical capacitors. Journal of the Electrochemical Society, 142(8):2699–2703, 1995.

[283] K. C. Liu and M. A. Anderson. Porous nickel oxide/nickel films for electrochemical capacitors. Journal of the Electrochemical Society, 143(1):124–130, 1996.

[284] M. Toupin, T. Brousse, and D. Belanger. Influence of microstucture on the charge storage properties of chemically synthesized manganese dioxide. Chemistry of Materials, 14(9):3946–3952, 2002.

[285] Longyan Yuan, Xi-Hong Lu, Xu Xiao, Teng Zhai, Junjie Dai, Fengchao Zhang, Bin Hu, Xue Wang, Li Gong, Jian Chen, Chenguo Hu, Yexiang Tong, Jun Zhou, and Zhong Lin Wang. Flexible solid-state supercapacitors based on carbon nanoparticles/mno2 nanorods hybrid structure. Acs Nano, 6(1):656–661, 2012.

[286] Brian E Francisco, Christina M Jones, Se-Hee Lee, and Conrad R Stoldt. Nanostructured all-solid-state supercapacitor based on li2s-p2s5 glass-ceramic electrolyte. Applied Physics Letters, 100(10):103902, 2012.

[287] Qing Hua Wang, Kourosh Kalantar-Zadeh, Andras Kis, Jonathan N. Coleman, and Michael S. Strano. Electronics and optoelectronics of two-dimensional transition metal dichalcogenides. Nature Nanotechnology, 7(11):699–712, 2012.

[288] R. H. Friend and A. D. Yoffe. Electronic-properties of intercalation complexes of the transition-metal dichalcogenides. Advances in Physics, 36(1):1–94, 1987.

[289] D. W. Murphy, F. J. Disalvo, G. W. Hull, and J. V. Waszczak. Convenient preparation and physical-properties of lithium intercalation compounds of group-4b and group-5b layered transition-metal dichalcogenides. Inorganic Chemistry, 15(1):17–21, 1976.

[290] Kin Fai Mak, Changgu Lee, James Hone, Jie Shan, and Tony F. Heinz. Atomically thin mos2: A new direct-gap semiconductor. Physical Review Letters, 105(13), 2010.

[291] Muharrem Acerce, Damien Voiry, and Manish Chhowalla. Metallic 1t phase mos2 nanosheets as supercapacitor electrode materials. Nature nanotechnology, 10(4):313–318, 2015.

[292] Guillaume A Muller, John B Cook, Hyung-Seok Kim, Sarah H Tolbert, and Bruce Dunn. High performance pseudocapacitor based on 2d layered metal chalcogenide nanocrystals. Nano letters, 15(3):1911–1917, 2015.

[293] Qasim Mahmood, Sul Ki Park, Kideok D Kwon, Sung-Jin Chang, Jin-Yong Hong, Guozhen Shen, Young Mee Jung, Tae Jung Park, Sung Woon Khang, Woo Sik Kim, et al. Charge storage: Transition from diffusion-controlled intercalation into extrinsically pseudocapacitive charge storage of mos2 by nanoscale heterostructuring (adv. energy mater. 1/2016). Advanced Energy Materials, 6(1), 2016.

[294] C. Umrigar, D. E. Ellis, D. Wang, H. Krakauer, and M. Posternak. Band-structure, intercalation, and interlayer interactions of transition-metal dichalcogenides - tis2 and litis2. Physical Review B, 26(9):4935–4950, 1982.

[295] F. Wypych and R. Schollhorn. 1t-mos2, a new metallic modification of molybdenum-disulfide. Journal of the Chemical Society-Chemical Communications, (19):1386–1388, 1992.

[296] K. M. Colbow, J. R. Dahn, and R. R. Haering. The 3r phase of lixtis2. Journal of Power Sources, 26(3-4):301–307, 1989.

[297] R. Schollhorn and A. Payer. Cis-tis2, a new modification of titanium disulfide with cubic structure. Angewandte Chemie-International Edition in English, 24(1):67–68, 1985.

[298] Jishnu Bhattacharya and Anton Van der Ven. First-principles study of competing mechanisms of nondilute li diffusion in spinel lixtis2. Physical Review B, 83(14), 2011.

[299] A. H. Thompson. Lithium ordering in lixtis2. Physical Review Letters, 40(23):1511–1514, 1978.

[300] Y. S. Kim, H. J. Kim, Y. A. Jeon, and Y. M. Kang. Theoretical study on the correlation between the nature of atomic li intercalation and electrochemical reactivity in tis2 and tio2. Journal of Physical Chemistry A, 113(6):1129–1133, 2009.

[301] D. W. Murphy and J. N. Carides. Low-voltage behavior of lithium-metal dichalcogenide topochemical cells. Journal of the Electrochemical Society, 126(3):349–351, 1979.

[302] Y. Kim, K. S. Park, S. H. Song, J. T. Han, and J. B. Goodenough. Access to m3+/m2+ redox couples in layered lims2 sulfides (m=ti, v, cr) as anodes for li-ion battery. Journal of the Electrochemical Society, 156(8):A703–A708, 2009.

[303] J. Dahn and R. R. Haering. Lithium intercalation in tis2. Materials Research Bulletin, 14(10):1259–1262, 1979.

[304] AL Patterson. The scherrer formula for x-ray particle size determination. Physical review, 56(10):978, 1939.

[305] S. B. Son, J. E. Trevey, H. Roh, S. H. Kim, K. B. Kim, J. S. Cho, J. T. Moon, C. M. DeLuca, K. K. Maute, M. L. Dunn, H. N. Han, K. H. Oh, and S. H. Lee. Microstructure study of electrochemically driven lixsi. Advanced Energy Materials, 1(6):1199–1204, 2011.

[306] Thierry Brousse, Mathieu Toupin, Romain Dugas, Laurence Athouel, Olivier Crosnier, and Daniel Belanger. Crystalline mno2 as possible alternatives to amorphous compounds in electrochemical supercapacitors. Journal of the Electrochemical Society, 153(12):A2171–A2180, 2006.

[307] Brian E Conway. Electrochemical supercapacitors: scientific fundamentals and technological applications. Springer Science & Business Media, 2013.

[308] H. Lindstrom, S. Sodergren, A. Solbrand, H. Rensmo, J. Hjelm, A. Hagfeldt, and S. E. Lindquist. Li+ ion insertion in tio2 (anatase) .2. voltammetry on nanoporous films. Journal of Physical Chemistry B, 101(39):7717–7722, 1997.

[309] P. Moreau, G. Ouvrard, P. Gressier, P. Ganal, and J. Rouxel. Electronic structures and charge transfer in lithium and mercury intercalated titanium disulfides. Journal of Physics and Chemistry of Solids, 57(6-8):1117–1122, 1996.

[310] J. C. Dupin, D. Gonbeau, I. Martin-Litas, P. Vinatier, and A. Levasseur. Amorphous oxysulfide thin films moysz (m = w, mo, ti) xps characterization: structural and electronic pecularities. Applied Surface Science, 173(1-2):140–150, 2001.

[311] Tianyang Li, Yi-Hsin Liu, Basant Chitara, and Joshua E. Goldberger. Li intercalation into 1d tis2(en) chains. Journal of the American Chemical Society, 136(8):2986–2989, 2014.

[312] Yu-Sheng Su, Yongzhu Fu, Thomas Cochell, and Arumugam Manthiram. A strategic approach to recharging lithium-sulphur batteries for long cycle life. Nature Communications, 4, 2013.

[313] Chenxi Zu, Nasim Azimi, Zhengcheng Zhang, and Arumugam Manthiram. Insight into lithium-metal anodes in lithium-sulfur batteries with a fluorinated ether electrolyte. Journal of Materials Chemistry A, 3(28):14864–14870, 2015.

[314] John F Moulder, Jill Chastain, and Roger C King. Handbook of X-ray photoelectron spectroscopy: a reference book of standard spectra for identification and interpretation of XPS data. Physical Electronics Eden Prairie, MN, 1995.

[315] H. F. Franzen, M. X. Umana, J. R. McCreary, and R. J. Thorn. Xps spectra of some transition-metal and alkaline-earth monochalcogenides. Journal of Solid State Chemistry, 18(4):363–368, 1976.

[316] Xia Li and Xueliang Sun. Nitrogen-doped carbons in li–s batteries: materials design and electrochemical mechanism. Frontiers in Energy Research, 2:49, 2014.

[317] M. L. Shek, J. Hrbek, T. K. Sham, and G. Q. Xu. A soft-x-ray study of the interaction of oxygen with li. Surface Science, 234(3):324–334, 1990.

[318] Kevin Tibbetts, Caetano R Miranda, Ying S Meng, and Gerbrand Ceder. An ab initio study of lithium diffusion in titanium disulfide nanotubes. Chemistry of Materials, 19(22):5302–5308, 2007.

[319] H. M. Rietveld. A profile refinement method for nuclear and magnetic structures. Journal of Applied Crystallography, 2:65–&, 1969.

[320] A. Lebail, H. Duroy, and J. L. Fourquet. Abinitio structure determination of lisbwo6 by x-ray-powder diffraction. Materials Research Bulletin, 23(3):447–452, 1988.

[321] J. W. Kim, J. J. Travis, E. Y. Hu, K. W. Nam, S. C. Kim, C. S. Kang, J. H. Woo, X. Q. Yang, S. M. George, K. H. Oh, S. J. Cho, and S. H. Lee. Unexpected high power performance of atomic layer deposition coated li ni1/3mn1/3co1/3 o-2 cathodes. Journal of Power Sources, 254:190–197, 2014.

[322] R. A. Huggins. Simple method to determine electronic and ionic components of the conductivity in mixed conductors a review. Ionics, 8(3-4):300–313, 2002.

[323] J. Evans, C. A. Vincent, and P. G. Bruce. Electrochemical measurement of transference numbers in polymer electrolytes. Polymer, 28(13):2324–2328, 1987.

Appendix A

Experimental

A.2 Chapter 2

All procedures outlined were conducted in a dry argon environment. To assemble test cells, a 200 mg glass solid electrolyte pellet separator was first pressed at 1 metric ton inside a polyetheretherketone (PEEK) lined Ti test cell die.[228] The $77.5Li_2S - 22.5P_2S_5$ glass sulfide solid electrolyte (SSE)[57,132] used as the basis for all-solid-state construction was prepared by ball milling with an appropriate ratio of Li_2S (Aldrich, 99.9%, reagent grade) and P_2S_5 (Aldrich, 99%) using a planetary ball mill (MTI Corporation SFM-1). The composite electrode was a 7:3 weight ratio of Sn powder (100 nm, Alfa Aesar, 99.8%) and glass SSE mixed by hand with agate mortar and pestle. 4 mg of the composite electrode was then pressed to one side of the glass electrolyte pellet at 375 MPa. A lithium-indium alloy (stoichiometry of $Li_{0.5}In$) (FMC Lithium Corp., Lectro Max Powder 100 and Indium powder, Alfa Aesar, Puratronic 99.999%) was attached to the opposite side of the pellet as a counter electrode at 375 MPa. The $Li_{0.5}In$ alloy has a potential of 0.62 V versus Li^+/Li for a limited compositional range[59] so voltage profile figures are given with respect to Li metal for convenience. Electrochemical performances were tested using Arbin BT2000 battery test station with a constant current constant voltage (CCCV) operation to cycle the cells at 60°C. External pressure was applied and maintained by clamping the cell die in a reinforced assembly and determined using a button load cell (Measurement Specialties, FC2311).

To analyze the microstructure, cross-sectional samples were prepared from the as-pressed

electrode before cycling test using a dual-beam focused ion beam (FIB) (FEI, Nova Nanolab 200) equipped with energy dispersive X-ray spectroscopy (EDS).

A.3 Chapter 3

All procedures outlined were conducted in a dry argon environment. To assemble test cells, a 150 mg glass solid electrolyte pellet separator was first pressed at 1 metric ton inside a PEEK lined Ti test cell die.[167] The $77.5Li_2S - 22.5P_2S_5$ glass SSE[126] used as the basis for all-solid-state construction was prepared by ball milling with an appropriate ratio of Li_2S (Aldrich, 99.9%, reagent grade) and P_2S_5 (Aldrich, 99%) using a planetary ball mill (MTI Corporation SFM-1). The composite electrode was a 52.5:17.5:30 weight ratio of Sn powder (100 nm, Alfa Aesar, 99.8%), Si powder (50 nm, Alfa Aesar, 99.99%), and glass SSE mixed by hand with agate mortar and pestle. Thus a 3:1 weight ratio of Sn to Si is used which is approximately a 1:1 volume ratio. 3 mg of the composite electrode was then pressed to one side of the glass electrolyte pellet at 375 MPa. A lithium-indium alloy (stoichiometry of $Li_{0.5}In$) (FMC Lithium Corp., Lectro Max Powder 100 and Indium powder, Alfa Aesar, Puratronic 99.999%) was attached to the opposite side of the pellet as a counter electrode at 375 MPa. The $Li_{0.5}In$ alloy has a potential of 0.62 V versus Li^+/Li for a limited composition range[59] so voltage profile figures are given with respect to Li metal for convenience. Cells are held under 20 MPa during operation. Electrochemical performances were tested using Arbin BT2000 battery test station with a CCCV operation to cycle the cells at 60°C.

To analyze the microstructure, a cell prepared as above was discharge to 5 mV then extruded from the die. X-ray diffraction (XRD) was carried out by sealing the pellet in an acrylic holder under a Be window to prevent air exposure. XRD patterns were collected with Cu Kα radiation ($\lambda = 1.5418$ Å) in the 2θ range of 20° - 60°, using a Bruker AXS D2 Phaser benchtop XRD system operated at 30 kV and 30 mA. A Lynxeye XE 1D detector with a step size of 0.02° and collection time of 1 s per step were employed. Sample displacement was corrected by using a pure corundum internal standard.

A.4 Chapter 4

Material Synthesis: All procedures outlined were conducted in a dry argon environment. $Li_{10}SiP_2S_{12}$ (LSiPS) was prepared in three ways. All three samples used the exact same composition of precursors of Li_2S (Aldrich, 99.9%), P_2S_5 (Aldrich, 99%) and SiS_2 (Aldrich, 95%) in a 5-1-1 molar ratio. The initial mixing process provides the differentiation between samples. Sample 1, LSiPS_0, used a vortex mill (Scientific Industries, Vortex-Genie 2) for 3 minutes to mix the precursors. Sample 2, LSiPS_1, planetary ball-milled (MTI Corporation SFM-1) 2 g of the precursors in an airtight, 500 mL stainless steel jar for 1 hour at 500 rpm. Sample 3, LSiPS_20, used the same process as sample 2 but ball-milled for 20 hours. Recovered powder for all three samples were then pressed into pellets 2 mm thick at 375 MPa in a titanium dye (ϕ = 1.3 cm. Pellets were then heat treated at 550°C for 8 hours in evacuated borosilicate glass ampoules. The resultant material was ground with agate mortar and pestle. LGPS was processed in the same manner as sample 3 using the precursor of GeS_2 (City Chemical, 99.99%). LGPS synthesis is in alignment with a previous report by Kamaya et al.[72] Throughout this text, the samples are referred to as LSiPS_0, LSiPS_1, LSiPS_20, and LGPS.

Material Characterization: XRD data was collected at beamline X14A (λ = 0.7788 Å) at the National Synchrotron Light Source at Brookhaven National Laboratory (NSLS-BNL). The data were collected with glass capillaries (0.5 mm diameter) in transmission mode using a silicon strip detector scanning from 6° to 60° 2θ. Samples were sealed in glass capillaries in an argon-filled glove box to avoid air exposure. For easy comparison with other researchers results, all 2θ values in the XRD data are converted to the 2θ value of Cu Kα wavelength (λ = 1.5418 Å). Because there are uncertainties about the structure details and our main interest is in the lattice parameter, Le Bail refinement was favored over Rietveld refinement. Le Bail refinement was carried out in GSAS-EXPGUI software using Von Dreele modified Le Bail fitting approach.[319,320] Materials were further characterized by scanning electron microscopy (SEM) (JEOL JSM-5910LV), and EDS.

Electrochemical Characterization: Ionic conductivity measurements were made using AC Impedance Spectroscopy with a Solartron 1280C with a frequency range of 20 kHz - 0.01 Hz. Samples were pressed into pellets approximately 1.5 mm thick at 375 MPa. 50 mg of copper nano-

powder (Alfa Aesar, 20 - 40 nm diameter, 99.99%) was pressed on either side of the electrolyte using 75 MPa to ensure sufficient electrical contact. Lithium stability tests were carried out by pressing 200 mg of each sample at 375 MPa and attaching lithium metal foil on either side under 75 MPa. AC Impedance sweeps were then performed using the test outlined previously but allowing the cell to relax at open circuit for 24 hour increments between sweeps. Ionic conductivity and lithium stability tests were performed under an argon environment.

Electrochemical Testing: Solid-state batteries were fabricated in a cell dye detailed by our previous study.[167] First a layer of LSiPS_20 was pressed using 200 mg of material at 75 MPa. 10 mg of $Li(Ni_{1/3}Mn_{1/3}Co_{1/3})O_2$ (Johnson Controls, 4 cycles of atomic layer deposition (ALD) Al_2O_3), LSiPS_20, and carbon black (Timcal, Super C65) was mixed by mortar and pestle in a 70:30:2 weight ratio and pressed onto one side of the separator layer using 375 MPa. Application of the ALD coating is outlined in a previous study.[321] Finally a piece of lithium foil is attached to the other side of the separator layer using 75 MPa. An identical cell using LGPS was also constructed. Electrochemical cycling was performed using an Arbin BT2000 Battery Test Station. The batteries were galvanostatically cycled using an aerial current density of 0.082 mA cm^{-2}, corresponding to a rate of C/10, in a voltage range of 2.5 - 4.3 V (vs. Li^+/Li). Conditions for the GITT test are outlined in a previous study.[321]

A.5 Chapter 5

All processes occurred in an argon environment. The $77.5Li_2S - 22.5P_2S_5$ solid electrolyte (denoted as a77.5) and original polyimine syntheses are reported elsewhere.[126,226] a77.5 and polyimine powders were measured in a 4 to 1 weight ratio into an agate jar with 50 x 6 mm agate balls; the powders were mixed through planetary ball-milling for 30 minutes.

Free-standing pellets (referred to as SEPM) of the resultant powder were developed with the following procedure: the composite was pressed at 38 MPa in a stainless steel dye (ϕ = 1.3 cm) while the temperature was raised to 100°C at 5°C min^{-1}; the pressure was held for another 15 minutes before increasing pressure to 228 MPa; the composite was held at this temperature and

pressure for 1 hour, periodically reapplying pressure lost due to shrinkage.

Densities were determined using a micron-resolution caliper to measure thickness (Mitutoyo, 547-400) and accurate mass of the samples. 3 samples were prepared for each formulation to get a standard error. Theoretical density for a77.5 is tough to accurately measure due to the nature of glass-ceramics. 1.75 g cm^{-1} is chosen using a tie line between densities of the precursors: Li_2S and P_2S_5. This value matches closely with what others have reported for similar near full-dense variations.[220] Theoretical densities of polyimine materials were measured by pressing polyimine powders into translucent films using the method outlined previously.

To measure long-term interaction between polyimine and electrolyte, ie. decomposition of material, a DC pulse technique is used to measure internal resistance of SEPMs. DC pulse resistance measurements are taken on symmetric lithium cells (lithium/SEPM/lithium) using a 0.1 mA pulse applied every 5 minutes.

For ionic conductivity tests, Ag paint (SPI) was used as blocking electrodes and allowed to cure at 120°C under ambient pressure. AC Impedance measurements were taken using a Solartron 1260 with a 100 mV amplitude between 1 MHz to 1 Hz on a heating process, equilibrating the temperature for 1 hour between tests. Typical equivalent circuits for ion blocking electrodes fit to the data in conjuncture with Equation A.1 to back out resistance and thus conductivity values.[322] Activation energy is determined from the slope of the Arrhenius plot.

$$\sigma = \frac{l}{RA} \tag{A.1}$$

A reinforced cell die is used for all cycling tests.[228] A pyrite based cathode is prepared by hand-mixing FeS_2 (Washington Mills, SULFEX Red), a77.5, and C65 (Timcal) in a 5:5:1 weight ratio. A large enough batch is prepared to mount on both the standard and SEPM separators. 5 mg of cathode is pressed onto aluminum foil at 38 MPa. 10 mg of prepared a77.5:polyimine powder is then pressed onto the cathode at 76 MPa. The whole stack then undergoes the same heat treatment procedure as before. Finally, an In-Li alloy (In + Li_xIn, $0 < x < 1$) is pressed onto the prepared

cell at 76 MPa. Galvanostatic cycling of cells occur on an Arbin B2000 Battery Testing Station. A rate of C/10 refers to an aerial current density of 0.15 mA cm^{-2}). Volumetric energy densities are calculated by measuring the tap density of the prepared cathode powder pressed into discs at 228 MPa.

A dynamic mechanical analysis (DMA) machine (Model Q800, TA Instruments, New Castle, DE, USA) was used to carry out tension tests at room temperature (23°C locally). All the samples were trimmed into a uniform size of 12 mm x 3 mm x 1.1 mm, and then stretched under a constant loading rate (2 MPa min^{-1}) until broken.

The time and temperature dependent relaxation modulus of the polyimine thermoset was also tested on the DMA machine (Model Q800, TA Instruments, New Castle, DE, USA). During the test, a polymer sample with the same dimension mentioned above was initially preloaded by 1 10^{-3} N force to maintain straightness. After reaching the testing temperature, it was allowed 30 min to reach thermal equilibrium. The specimen was stretched by 1% on the DMA machine and the deformation was maintained throughout the test. The decrease of stress was recorded and the stress relaxation modulus was calculated.

The master relaxation curve suggests that the kinetics of the (bond exchange reaction (BER) induced stress relaxation follows the well-known temperature-time superposition (TTSP) principles. To quantitatively study the relaxation behavior, we used the following definition of relaxation modulus:

$$\tau = \frac{1}{k} e^{\frac{E_a}{RT}} \tag{A.2}$$

where k is a kinetic coecient ($k > 0$), R is the gas constant with $R = 8.31446$ J K^{-1} mol^{-1}, and E_a is the activation energy.

The shift factor, namely the ratio between the temperature dependent relaxation time and

the relaxation time at a reference temperature T_r, is therefore expressed as:

$$\alpha = exp\left[\frac{E_a}{R}\left(\frac{1}{T} - \frac{1}{T_r}\right)\right] \tag{A.3}$$

The predicted shift factors of the relaxation curves are also plotted in Figure 6.2g - i to compare with the experimental data. An Arrhenius-type dependence on temperature is revealed, which is consistent with what we previously reported for the tri-imine. By further examination of Equation A.3 we found that in the semi-log scale, the energy barrier could be determined by the slope of the shift factor curve. As shown in Figure 6.2g - i, by measuring the curve slope, the energy barrier E_a is calculated for each formulation.

Lithium ion transference number is calculated using the Bruce-Vincent-Evans (BVE) technique as in Equation A.4.[323] SEPMs are constructed into a symmetric lithium cells (lithium / SEPM / lithium); lithium is scraped prior to use to remove any native layer. BVE requires the measurement of initial and steady state current, I_0 and I_S, respectively, for a given DC polarization, ΔV. Initial and steady state resistance values, R_0 and R_S, are determined through AC Impedance using the same test as before. Steady state is determined once less than a 1% change in current occurred in a 10 minute period.

$$t_{Li+} = \frac{I_S(\Delta V - I_0 R_0)}{I_0(\Delta V - I_S R_S)} \tag{A.4}$$

A.6 Chapter 6

All processes occurred in an argon environment. The $77.5Li_2S - 22.5P_2S_5$ solid electrolyte (denoted as a77.5) and original polyimine syntheses are reported elsewhere.[126,226] Variations of the polyimine used can be found in Section 5 and Figure 5.1.

Composites were characterized by SEM (JEOL JSM-5910LV).

Composites are prepared by mixing appropriate amounts of a77.5 and polyimine in a mortar and pestle for 3 minutes. A hot-press follows the same preparation as in Section 5. Cold-pressed

pellets are pressed at 5 MT in a PEEK-lined Ti die for 5 minutes. For both galvanostatic polarization and cycling tests, the cell construction is Li foil / Composite / Li foil. Li foil is attached onto the prepared composite using a torque wrench and applying 10 in-lb. Battery operation takes place with the cell in an oven to the desired temperature and controlled using a Arbin BT2000 Battery Testing Station.

A.7 Chapter 7

All procedures outlined were conducted in a dry argon environment. The $77.5Li_2S - 22.5P_2S_5$ solid electrolyte (denoted as a77.5) is prepared by planetary ball-milling Li_2S (Alfa, 99.9%) and P_2S_5 (Sigma, 99%) in a 77.5 to 22.5 molar ratio for 20 hours in a 500 mL stainless steel jar. The standard cathode is prepared by hand-mixing FeS_2 (Washington Mills, SULFEX Red), a77.5, and C65 (Timcal Super C65) in a 5:5:1 weight ratio. A large enough batch is prepared to use for all experiments. The FeS_2-LTS cathode is prepared by planetary ball-milling FeS_2, TiS_2 (Sigma, 99.9%), and Li_3N (Alfa, 99.4%) in a 3.1:3:1 molar ratio for 20 hours in a 100 mL agate jar. The theoretical capacity is therefore, 51% weight FeS_2 (894 mAh g^{-1}) and 49% weight $LiTiS_2$ (227 mAh g^{-1}) yielding 567 mAh g^{-1}.

A reinforced cell die is used for all electrochemical tests.[167] 150 mg of a77.5 is pressed at 75 MPa as a separator. Either the standard or FeS_2-LTS cathode is pressed onto one side of the separator at 375 MPa (3.75 mg cm^{-2} for cycling and rate study; 2.25 mg cm^{-2} for GITT; 0.75 mg cm^{-2} for CV and Tafel). Concurrently, Li metal foil [CV, GITT, Tafel] or an In-Li alloy (In + Li_xIn, $0 < x < 1$) [rate study and cycling] is pressed onto the other side of the separator as a counter electrode. Cyclic voltammetry (CV) and Tafel Analysis is carried out on a Solartron 1280C Electrochemical Test System. Tafel Analysis, more specifically, took place on the third cycle discharge by holding the cell at either 2.17 V (intercalation) or 1.53 V (conversion) for 1 hour; then a linear sweep was performed at 1 mV s^{-1} between ±150 mV around open circuit voltage (OCV). Galvanostatic intermittent titration technique (GITT) and cycling was performed using an Arbin BT2000 Battery Test Station. GITT is performed by using a rate of C/20 for 1 hour followed by

a 6 hour relaxation. An aerial current density of 0.21 mA cm^{-2} corresponds to a rate of C/10. The rate study and long-term cycling use an operating voltage window of 3 - 1 V (vs. Li^+/Li). All electrochemical tests are performed at 60°C unless otherwise noted; cells are allowed 3 hours of temperature acclimating before tests are performed.

XRD patterns were collected with Cu Kα radiation (λ = 1.5418 Å) in the 2θ range of 25° - 50°, using a Bruker AXS D2 Phaser benchtop XRD system operated at 30 kV and 30 mA. A Lynxeye XE 1D detector with a step size of 0.02° and collection time of 1 s per step were employed. Sample displacement was corrected by using a pure corundum internal standard.

For the detailed observation of uncycled and 10th cycle composite electrodes, assembled cells are extruded from the pressure die. Samples cross-sections are prepared using a FIB (FEI NOVA200 dual beam system) machine equipped with air-lock system. The air-lock system enables our composite electrode to remain in a vacuum state while samples are loaded from the glove box to the FIB chamber. High resolution transmission electron microscopy (HR-TEM) (TEM, JEOL 3000F) is then performed on the fine-milled cross-sections. These techniques are detailed in previous studies.[305]

A.8 Chapter 8

All procedures outlined were conducted in a dry argon environment. The $77.5Li_2S - 22.5P_2S_5$ solid electrolyte (denoted as a77.5) is prepared by planetary ball-milling Li_2S (Alfa, 99.9%) and P_2S_5 (Sigma, 99%) in a 77.5 to 22.5 molar ratio for 20 hours in a 500 mL stainless steel jar. The three samples used in this study are synthesized as followed and make use of the same TiS_2 (Sigma, 99.9%) and Li_3N (Alfa, 99.4%) sources. Bulk TiS_2 (*b*TS) is the straight as-bought TiS_2. Nano $LiTiS_2$ *n*LTS) planetary ball-mills TiS_2 and Li_3N together in a 100 mL agate jar using 50 x 3 mm agate balls for 2 hours. Disorder $LiTiS_2$ (*a*LTS) uses the same process as *n*LTS but mills for 20 hours operating time.

XRD patterns were collected with Cu Kα radiation (λ = 1.5418 Å) in the 2θ range of 25° - 50°, using a Bruker AXS D2 Phaser benchtop XRD system operated at 30 kV and 30 mA. A

Lynxeye XE 1D detector with a step size of 0.02° and collection time of 1 s per step were employed. Sample displacement was corrected by using a pure corundum internal standard. For the detailed observation of *a*LTS microstructure, powder samples are cross-sectioned using a FIB (FEI NOVA200 dual beam system) machine equipped with air-lock system. The air-lock system enables the sample to remain in a vacuum state while being loaded from the glove box to the FIB chamber. HR-TEM (TEM, JEOL 3000F) is then performed on the fine-milled cross-sections. Selected area electron diffraction (SAED) and zero loss electron energy loss spectroscopy (EELS) takes place on the same machine.

A reinforced cell die is used for all electrochemical tests.[167] 150 mg of a77.5 is pressed at 75 MPa as a separator. The cathode samples are then pressed onto one side of the separator at 375 MPa (3.75 mg cm^{-2} for cycling and rate study; 2.25 mg cm^{-2} for GITT; 0.75 mg cm^{-2} for CV). Concurrently, Li metal foil [CV, GITT] or an In-Li alloy (In + Li_xIn, $0 < x < 1$) [rate study and cycling] is pressed onto the other side of the separator as a counter electrode. CV analysis is carried out on a Solartron 1280C Electrochemical Test System. GITT and cycling was performed using an Arbin BT2000 Battery Test Station. GITT is performed by using a rate of C/20 for 1 hour followed by a 6 hour relaxation. An aerial current density of 0.09 mA cm^{-2} corresponds to a rate of C/10. The rate study and long-term cycling use an operating voltage window of 3 - 1 V (vs. Li^+/Li). Testing temperature is set using ovens (Quincy Labs, Model 30) and cells are allowed 2 hours of temperature acclimating before tests are performed.

X-ray photoelectron spectroscopy (XPS) took place at the National Renewable Energy Laboratory in Golden, CO. Samples were prepared using the method outlined above. An initial charge took place and the samples were stopped at various voltages on the second cycle. The sample was extruded and transported under an Ar environment.